Investigations on Cs-free alternative materials for negative hydrogen ion formation

Dissertation

zur Erlangung des akademischen Grades

Dr. rer. nat.

eingereicht an der

Mathematisch-Naturwissenschaftlich-Technischen Fakultät

der Universität Augsburg

von

Uwe Kurutz

Augsburg, September 2016

Universität
Augsburg
University

Tag der mündlichen Prüfung: 19.01.2017

Erster Gutachter: apl. Prof. Dr.-Ing. U. Fantz

Zweiter Gutachter: Prof. Dr. A. Wixforth

Contents

1 Introduction

Addressing the energy demand of a growing world population, thermonuclear fusion represents a possible solution. In this context, the world's largest international fusion experiment is currently under construction in Cadarache, South France: **ITER**[1]. As the name indicates, ITER is designed for experimental purposes and is an intermediate step on the roadmap towards a fusion power plant. The machine beyond ITER will be the **DEMO**nstration power plant **DEMO**. It will be the last step towards a commercial reactor based on fusion energy.
A key system for heating and current drive of such fusion machines is neutral beam injection based on negative hydrogen ions (NNBI). Negative ions are formed in the volume of a low pressure, low temperature hydrogen plasma produced in the injectors ion source and by plasma surface interaction. After formation negative ions are extracted and accelerated by a multi grid system to form a high energetic particle beam. The ion beam is subsequently neutralised to a high energetic neutral particle beam and directed into the fusion device.
Requirements for future NNBI systems are very challenging. In case of ITER NNBI a very homogeneous, high energetic 1 MeV ion beam of 40 A extracted from an extraction area of $0.2\,\mathrm{m}^2$, i.e. with a negative ion current density of $200\,\mathrm{Am}^{-2}$ is demanded for pulse lengths of up to one hour. Moreover, the ratio of inevitably co-extracted electron current to the extracted negative ion current has to be below unity. In case of DEMO, requirements are not as specified yet but corresponding or even more challenging demands are realistic. At present, no such NNBI systems exist and extensive research and development is performed.
At ITER NNBI negative ion formation will be based on the conversion of positive ions and atomic hydrogen at a caesiated converter surface. Caesium is applied for reducing the converter's work function, which results in a significant enhancement of particle conversion into negative hydrogen ions. However, although capable of maintaining a high negative ion yield, the alkali metal exhibits a high chemical reactivity and is subject to plasma induced redistribution processes. Thus a complex caesium dynamic is given. Known from present test stands like the ones

[1] **I**nternational **T**hermonuclear **E**xperimental **R**eactor (Latin for 'the way').

at IPP[2] which are equipped with the prototype sources for ITER, caesium will have to be continuously evaporated into the source for maintaining a spatially homogeneous and temporal stable low converter surface work function, i.e. for continuously delivering the demanded high source performance. The arising caesium consumption and the migration of caesium into the accelerator stage are critical issues regarding the maintenance periods and system reliability and thus, for DEMO NNBI and beyond alternative materials are needed.
Investigations on different materials for negative hydrogen ion formation have been performed throughout the literature at different experiments focused on specific material types in tailored experimental setups. However, partially inconsistent or even contrary results have been reported and additionally the comparability of those investigations and the transfer to NNBI ion sources is rather limited. For the application in negative ion sources for NNBI, comparable investigations are required at actual operational ion source relevant conditions, i.e. in a low pressure low temperature hydrogen plasma providing a high combined flux of atomic hydrogen and positive ions.
The aim of this work is therefore the systematic investigation of different caesium-free materials at one distinct experimental setup which provides ion source relevant parameters and directly compare the effect on the negative ion density with the application of caesium.

These investigations are carried out at the laboratory experiment HOMER[3] where the plasma is monitored with a multitude of different diagnostics for measuring the overall plasma parameters and in particular the negative hydrogen ion density. Investigations are focused on materials known from literature, i.e. on materials with an intrinsically low work function, different types of doped and non-doped diamond as well as on the refractory metals tantalum and tungsten. A material's impact on the plasma and especially on the negative ion density is directly compared with other materials at equal external experimental conditions. Underlying negative ion related volume processes are modelled using a 0-dimensional model for balancing volume formation and destruction channels on bases of measured input parameters which allows for assessing a materials impact on the negative ion density. In order to set gained results into perspective, investigations are compared to measurements with a stainless steel reference sample representing the negative ion density coming from pure volume processes on the one hand and by in-situ application of caesium i.e. the aimed for enhancement on the other hand.

[2]Max-Planck-Institut für Plasmaphysik, Garching (Germany).
[3]**HOM**ogeneous **E**lectron cyclotron **R**esonance plasma.

2 Ion Sources for Negative Hydrogen Ions

A promising concept for future power generation is thermonuclear fusion in a magnetically confined plasma composed of deuterium and tritium [SCM+07]:

$$^{2}\mathrm{D} + {}^{3}\mathrm{T} \rightarrow {}^{4}\mathrm{He} + \mathrm{n} + 17.6\,\mathrm{MeV} \quad . \tag{2.1}$$

Two basic concepts exist that follow this approach: the *Tokamak* and the *Stellarator* (see figure 2.1). The Tokamak concept, is based on the transformer principle and the magnetic field needed for plasma confinement is created by external coils superimposed by a magnetic field resulting from a toroidally driven plasma current. The current is induced as the plasma acts as a secondary winding for a transformer whose solenoid is in the centre of the torus. Hence, a pulsed operation is inherent for the Tokamak. In a Stellarator the plasma confining magnetic field is solely created by a complex geometry of solenoids avoiding the need of a plasma current. It allows for a steady-state operation that is generally advantageous, as a competitive future fusion power plant will have to operate in steady-state or long-pulse mode of several hours. However, due to the complex geometry of solenoids needed for the Stellarator, the development of the Tokamak concept is currently further progressed[1].

For sufficient energy production in fusion reactors, high collision rates are needed that are achieved by heating the confined plasma to temperatures up to 100 million Kelvin. To sustain the plasma at those high temperatures in a controlled way different auxiliary heating systems like electron cyclotron resonance heating (ECRH), ion cyclotron resonance heating (ICRH) or neutral beam injection (NBI) are applied.

NBI provides beside its heating capabilities, an efficient way of toroidal current drive and thus it allows for an extension of a Tokamaks pulse length. It will be

[1] Further information on the Tokamak and the Stellarator principle can be found in [Sch93].

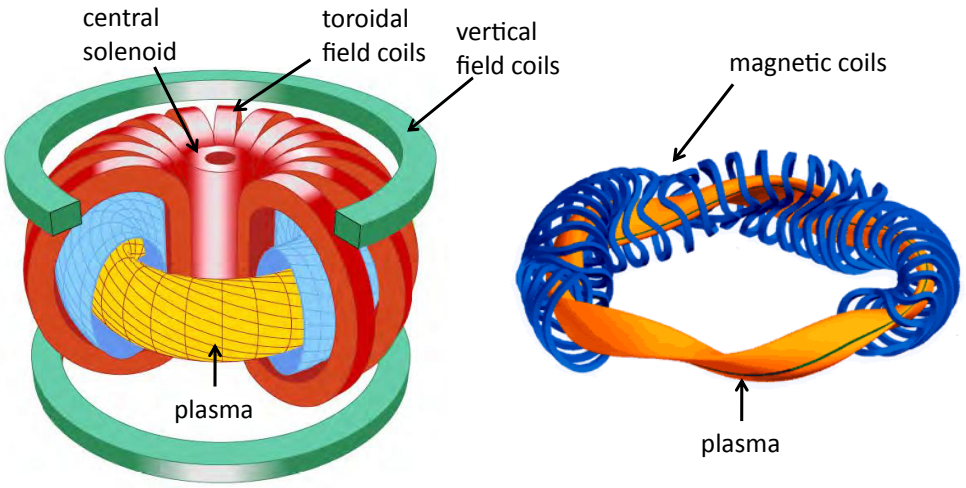

Figure 2.1: *Schematic drawing of the two reactor concepts for thermonuclear fusion based on magnetic confinement: Tokamak (left) and the Stellarator (right). The major radius of such toroidal machines is in the order of* $\gtrsim 5\,m$.

therefore a key system for heating and current drive at the world largest next generation Tokamak **ITER** (**I**nternational **T**hermonuclear **E**xperimental **R**eactor) which is currently under assembly in Cadarache, south France. ITER will start first plasma operation in December 2025 and the scope of ITER is to demonstrate the scientific and technological feasibility of fusion energy for up to one hour [ITE16, IAE02]. For the corresponding pulse lengths two NBI systems will provide a total injected power of 33 MW with a beam energy of 1 MeV [IAE02]. According to the European *roadmap to the realisation of fusion energy* as a sustainable and secure energy source, the machine beyond ITER will be a **DEMO**nstration reactor **DEMO**, which will be the last machine towards a commercial fusion power plant [RBB+12]. The construction of DEMO will be prepared between 2021 and 2030 and is expected to commence in 2031 aiming to start first plasma operation in the early 2040's. The production of net electricity from fusion is planned to start in 2050 [RBB+12]. In the European DEMO's present conceptual design status two scenarios are considered: a pulsed and a cw option [FBB+15a, FBB+15b]. Depending on the scenario different research and development needs for heating and current drive arise that are currently under assessment (see for instance [SBJ+12, FF13a, McA14]). When a DEMO NBI system will be applied, the system will be based on the technological know-how and design of the ITER NBI system. It is discussed that a DEMO NBI system has to deliver

a total injected power of up to 50 MW in case of a pulsed scenario and up to 135 MW for a steady-state scenario with beam energies between 1 and 1.5 MeV [FBB+15b, GAB+15]. For the application at DEMO, it is of major relevance, that a DEMO NBI system provides a high reliability, availability, maintainability and a facilitated inspectability, also known as RAMI issues together with a high plug-in efficiency [FBB+15a, FBB+15b].

Neutral Beam Injection

The NBI heating and current drive is based on the injection of a high energetic particle beam into the fusion plasma, depositing its energy by collisions. The beam for ITER will consist of neutral hydrogen or deuterium particles, able to pass through the external magnetic field that confines the fusion plasma. (Within this work for simplification, the term hydrogen will be used as a synonym for deuterium and hydrogen. A distinction will be made when necessary to emphasis a present difference).

A schematic drawing of an NBI system is shown in figure 2.2. It consists of an ion source, an extraction and acceleration multi-grid system, a neutraliser and a beamline connecting the system to the fusion device. In the ion source a low pressure low temperature hydrogen plasma is created. Charged particles are subsequently extracted by the electrostatic grid system and accelerated to high energies. After acceleration, the precursor charged particle beam is neutralised in a gas target[2] via charge exchange collisions. Residual ions are deflected by a magnetic field to an ion dump. For minimizing transmission losses due to collisions with residual gas after the neutraliser, a large scale vacuum pump is reducing the pressure and the high energetic neutral beam is transmitted to the fusion plasma torus.

Most present NBI systems like for the currently largest fusion experiment JET (**J**oint **E**uropean **T**orus) are based on positive ions. The JET NBI system delivers in short pulses (seconds range) a maximal total beam power of up to 34 MW with particle energies of up to 125 keV [AJS+15]. For ITER and DEMO, NBI systems will have to deliver for pulse lengths of up to one hour a higher total injected power with particle energies of at least 1 MeV [IAE02, SBJ+12, FF13a, McA14, FBB+15b]. As shown in figure 2.3 the neutralisation efficiency in a gas neutraliser is significantly reduced for such high energetic positive ions [BPS75], while to the contrary, for negative deuterium ions the neutralisation efficiency

[2]For DEMO other neutraliser concepts like a photo or plasma neutraliser may be applied [McA14].

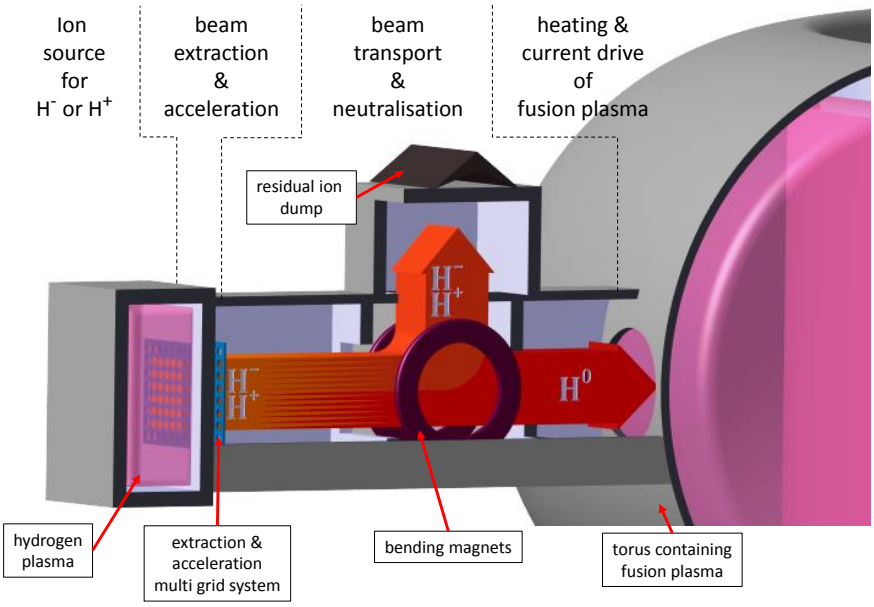

Figure 2.2: *Schematic drawing of a neutral beam injection (NBI) system. The typical length of a NBI system is in the order of several 10 m.*

does not decline below 60 %. Consequently, for maintaining a high overall efficiency of the NBI system, at ITER and DEMO the NBI will be based on negative ions [IAE02, FBB+15a, FBB+15b].

Negative Ion Based Systems

Positively charged particles for positive ion based systems are efficiently formed via ionising collisions within the ion source plasma bulk (see chapter 3.1). The most relevant pathway for negative ion formation in case of negative ion based NBI (NNBI) systems is given via a particle conversion at the plasma facing grid (PG, first grid of the multi grid system) (see chapter 4.1.2). Furthermore, negative ions are also formed in the bulk plasma volume (see chapter 4.1.1). However, due to the low binding energy of the negative hydrogen ions additional electron, negative ions are easily destroyed in the plasma volume (see chapter 4.1.3). As a consequence, the mean free path of negative ions in ion sources is generally low and most of the extracted negative ions are created in the vicinity of the plasma grid [GWF+09].

For reducing the negative ion loss rate in the accelerator stage, the ITER negative ion source has to be operated at low pressure of maximal 0.3 Pa [IAE02]. At such low pressure, only negative ion sources based on the negative ion surface production are capable to fulfil the required parameters for ITER [SFF+06]:

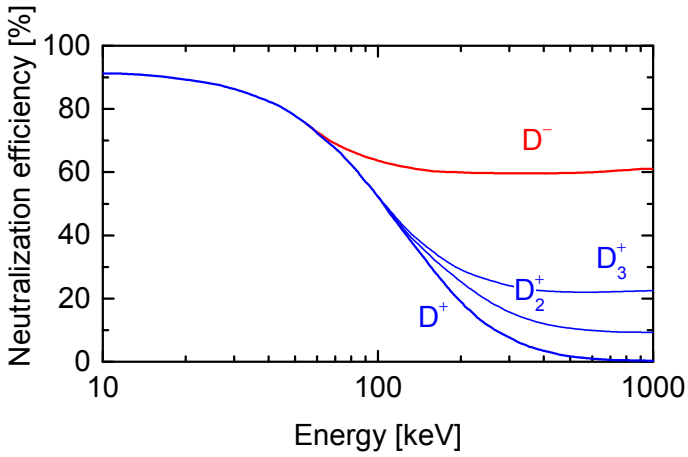

Figure 2.3: *Neutralisation efficiency versus particle energy of positive and negative deuterium ions travelling through a gas target of optimal thickness [BPS75].*

Specified in [IAE02], the ITER NBI will have a source area of $1.5\times0.6\,\mathrm{m}^2$. The system will have to deliver a negative ion current of 40 A D^- at a current density of $200\,\mathrm{Am}^{-2}$. Therefore, the beam is extracted from an extraction area of $0.2\,\mathrm{m}^2$ that possesses 1280 extraction apertures with a diameter of 14 mm each. During the one hour pulse length a high beam homogeneity with deviations of maximally $\pm10\,\%$ are demanded.

For negative ion extraction the ion source, including the plasma and acceleration grid (both grids at different negative potentials) is negatively biased against a third, grounded grid. This allows for controlling the beam extraction performance, but is linked with the inevitably co-extraction of electrons due to the same charge state of electrons and negative ions. In order to protect components after the extraction and acceleration stage from high energetic electron bombardment, co-extracted electrons are deflected within this multi-grid system prior to full acceleration via bending magnets. The resulting heat load on components is a limiting factor and thus, for ITER NNBI, the ratio of the co-extracted electron current density j_e to the extracted negative ion density j_{D^-} has to be below unity [IAE02].

In the EU fusion roadmap it is favoured that initial system design studies for DEMO are as much as possible based on the extrapolation from ITER experience [RBB+12, FBB+15b]. Thus, research and development focused on the ITER NNBI systems will influence a future DEMO NBI design and described ITER NBI parameters can be seen to represent at least minimal requirements for a DEMO

NNBI system.
Up to date, NNBI systems that achieve all ITER requirements simultaneously do not exist. Main tasks concern for example the ion source, i.e. the efficiency of negative ion formation and homogeneous and temporal stable operation as well as the stable and reliable 1 MeV particle acceleration. In the context of the ion source topics, research and development is performed at the Max-Planck-Institute for Plasmaphysics (IPP) in Garching (Germany). At present the test facilities BATMAN (**BA**varian **T**est **MA**chine for **N**egative ions) [SFF+06] and ELISE (**E**xtraction from a **L**arge **I**on **S**ource **E**xperiment) [HFF+09, FHF+13] are in operation. Both test stands are equipped with the RF prototype sources for ITER. BATMAN has a source area of $0.32 \times 0.59\,\mathrm{m}^2$ with an extraction area of about $7.0\times10^{-3}\,\mathrm{m}^2$. With this test stand, it has already been demonstrated that in short pulses (seconds range) at low pressure the ITER required current densities at the demanded electron to negative ion current density ratio can be achieved [SFF+06]. ELISEs design allows for cw operation and the pulsed extraction of negative ion beams of 10 s every 150 s. It has a larger source area of $1.0\times0.9\,\mathrm{m}^2$ and an extraction area of $0.1\,\mathrm{m}^2$, i.e. half of the size of the ITER NNBI ion source. One objective of ELISE is to demonstrate ion source size scaling towards ITER NNBI.

Current test facilities, like BATMAN and ELISE achieve high extracted negative ion currents and simultaneously low amounts of co-extracted electrons at low pressure by negative ion production at converter surfaces with a low work function. Therefore, caesium is evaporated into the ion sources. The alkali metal is subject of complex redistribution processes in the ion source body and results in a reduction the PG's work function. Neutral hydrogen atoms and positive ions, impinging on the PG are converted, with a probability depending on the work function, to negative ions and are subsequently extracted.
For providing long pulses of negative ion beams with high homogeneity and high negative ion current densities, a uniform and stable negative ion formation at the PG is a requisite. Therefore, a uniform low work function has to be maintained. After [FFW12], this is the most challenging task for operation of negative ion sources based on the application of caesium: caesium is characterised by a high chemical reactivity and consequently compounds with unavoidable impurities within the ion sources (e.g. residual oxygen and water) are easily formed. This results in a spatially inhomogeneous deterioration of the low work function

and consequently in the negative ion formation probability. For maintaining a stably low and uniform work function of the PG, i.e. a high source performance, up to date careful source conditioning by frequent evaporation of fresh caesium is needed. This affects the availability and reliability of NNBI systems [FFW12]. Maintenance periods for NNBI systems are sensitive to the caesium consumption [FF13a] and a possible migration of caesium into the accelerator stage, causing a reduction of the high voltage holding capabilities of different components can affect the reliability of such systems. As these issues are in contradiction to RAMI needs for future NNBI systems caesium-free alternatives are investigated for efficient negative ion formation.

Such investigations are performed within this work at the small scale laboratory experiment HOMER (**HOM**ogeneous **E**lectron cyclotron **R**esonance plasma) that provides comparable plasma conditions like those in front of the PG in combination with a high flexibility and diagnostic accessibility.

In table 2.1 a comparison of characteristic parameters of HOMER and the IPP prototype source at BATMAN in front of the PG is presented. Both experiments are operated in hydrogen and deuterium at a gas pressure of down to 0.3 Pa. Negative ion formation and destruction processes are sensitive to plasma conditions like electron temperature and electron density (both directly determine electron stripping by electron negative ion collisions for example). Furthermore, surface production of negative ions in BATMAN is mainly a consequence from neutral atomic hydrogen conversion, correlated with the atomic hydrogen flux [WSM+12]. As can be seen, despite of a significant higher available discharge power, the small scale laboratory experiment HOMER provides within its smaller discharge volume comparable electron temperatures and densities like in front of BATMANs PG and a comparable flux of atomic hydrogen. This is indispensable for the transferability of gained results at HOMER to negative ion source application.

Table 2.1: *Parameters and characteristics of the laboratory setup HOMER and the IPP prototype source at BATMAN. Plasma parameters in case of the prototype source represent typical conditions in front of the plasma grid.*

	HOMER	**BATMAN**
Pressure [Pa]	≥ 0.3 (H_2, D_2)	≥ 0.3 (H_2, D_2)
Discharge power [kW]	≤ 1	≤ 150
Power density [kW/m^{-3}]	$\lesssim 260$	$\lesssim 2930$
Electron temperature [eV]	0.5 – 2	1 – 2
Electron density [m^{-3}]	10^{16} – 10^{17}	10^{16} – 10^{17}
Atomic hydrogen density [m^{-3}]	10^{18} – 10^{19}	10^{18} – 10^{19}
Atomic hydrogen flux [m^{-2}s^{-1}]	10^{21} – 10^{22}	10^{21} – 10^{22}

3 Low Temperature Low Pressure Hydrogen Plasmas

3.1 General Plasma Characteristics

Within a plasma, i.e. an at least partially ionised gas, neutral particles like molecules and atoms as well as positively and negatively charged species are present[1]. In case of a low pressure, low temperature hydrogen plasma these particles are neutral H_2 molecules and H atoms, three different species of positive ions (H^+, H_2^+, H_3^+), negative hydrogen ions H^- and electrons.
A plasma is *quasi-neutral* on a macroscopic scale. This means, the sum of the positive charge density equals the sum of the negative charge density. With $n_{H^+}, n_{H_2^+}$, $n_{H_3^+}$ and n_{H^-} representing the corresponding positive and negative ion densities of H^+, H_2^+, H_3^+ and H^-, and n_e denoting the electron density, this yields for a hydrogen plasma:

$$n_{H^+} + n_{H_2^+} + n_{H_3^+} = n_e + n_{H^-} \quad . \tag{3.1}$$

Deviations from quasi-neutrality are only possible within the so-called *Debye length*:

$$\lambda_D = \sqrt{\frac{\epsilon_0 k_B T_e}{e^2 n_e}} \tag{3.2}$$

where ϵ_0 is the permittivity constant, k_B the Boltzmann constant, e the elementary charge and T_e the electron temperature. For dimensions exceeding this scale (typically some μm), present Coulomb potentials are efficiently shielded by electrons and quasi-neutrality is fulfilled.

The description of the various processes in a plasma is possible by the application of distribution functions $f(\mathbf{v}, \mathbf{r}, t)$. These functions give the probability of

[1] The following presented plasma characteristics are based on [LL05] and [CB11] where a detailed description of plasma discharges and processes can be found.

a particle per unit volume and per unit time being in a certain velocity or energy unit. Their evolution can be calculated via the so-called *Boltzmann equation*:

$$\frac{df}{dt} = \frac{\partial f}{\partial t} + \boldsymbol{v} \cdot \nabla_{\boldsymbol{r}} f + \frac{\boldsymbol{F}}{m} \nabla_{\boldsymbol{v}} f = \left(\frac{\partial f}{\partial t} \right)_{\text{coll}} \quad , \tag{3.3}$$

where $\boldsymbol{F} = |q| \left(\boldsymbol{E} + \boldsymbol{v} \times \boldsymbol{B} \right)$ is the force of a local electric and local magnetic field $\boldsymbol{E}$ and $\boldsymbol{B}$ onto a particle of mass m and charge q. By the collisional term $(\partial f / \partial t)_{\text{coll}}$ a redistribution of $f(\mathbf{v}, \mathbf{r}, t)$ due to elastic and inelastic collisions can be attributed. Of major relevance in low temperature, low pressure plasmas is the *electron velocity distribution function* (**EVDF**) $f_{\text{e}}(\boldsymbol{v}, \boldsymbol{r}, t)$ or the equivalent *electron energy distribution function* (**EEDF**) $f_{\text{e}}(E, \boldsymbol{r}, t)$.
The density of a specific particle ensemble like the electron density n_{e} (this also holds for other particle species) is given by the integration in $\boldsymbol{v}$-space of the corresponding distribution function $f_{\text{e}}(\boldsymbol{v}, \boldsymbol{r}, t)$ and the mean velocity is given by $\langle v_{\text{e}}(\boldsymbol{r}, t) \rangle = \frac{1}{n_{\text{e}}} \int d^3 v \boldsymbol{v} f_{\text{e}}(\boldsymbol{v}, \boldsymbol{r}, t)$.
In case of the ensemble being in thermal equilibrium, the distribution function is given by the Maxwell-Boltzmann or short Maxwell distribution $f_{\text{M}}(\boldsymbol{v}, \boldsymbol{r}, t)$ and a temperature T can be assigned to the particle ensemble. For an isotropic, spatially and temporal constant distribution function describing a particle ensemble like the electron ensemble, the Maxwellian distribution function can be written as:

$$f_{\text{M}}(v_{\text{e}}) = n_{\text{e}} \left(\frac{m_{\text{e}}}{2\pi k_{\text{B}} T_{\text{e}}} \right)^{3/2} 4\pi v_{\text{e}}^2 \exp\left(-\frac{m_{\text{e}} v_{\text{e}}^2}{2 k_{\text{B}} T_{\text{e}}} \right) \quad , \tag{3.4}$$

with m_{e} being the electron mass. The mean thermal velocity $\langle v_{\text{e}} \rangle$ is given by $\langle v_{\text{e}} \rangle = \sqrt{8 k_{\text{B}} T_{\text{e}} / \pi m_{\text{e}}}$ and a transformation of this distribution function into the energy dependent form yields:

$$f_{\text{M}}(E_{\text{e}}) = \frac{2 n_{\text{e}}}{\sqrt{\pi}} \left(\frac{1}{k_{\text{B}} T_{\text{e}}} \right)^{3/2} \sqrt{E_{\text{e}}} \exp\left(-\frac{E_{\text{e}}}{k_{\text{B}} T_{\text{e}}} \right) \quad . \tag{3.5}$$

Like the mean velocity, the mean energy can be defined via:

$$\langle E_{\text{e}} \rangle = \frac{1}{n_{\text{e}}} \int dE_{\text{e}} E_{\text{e}} f(E_{\text{e}}) \tag{3.6}$$

that transforms in case of a Maxwellian distribution into:

$$\langle E_{\text{e}} \rangle = \frac{3}{2} k_{\text{B}} T_{\text{e}} \quad . \tag{3.7}$$

Laboratory plasmas, including those in ion sources are generated by electric or electromagnetic fields. Thereby, efficient energy transfer is provided dominantly to electrons and heavy particles like ions and neutrals are mainly heated by elastic electron collisions. Due to the ineffectiveness of elastic collisions between particles with a distinct mass difference and low collision rates present in low pressure, low temperature discharges, electrons and heavy particles do not thermalize among each other. As a consequence, the electron temperature is significantly higher than heavy particle temperatures like for neutrals (e.g. the gas temperature T_{gas}) and for ions T_{i}. Thus, a low temperature, low pressure plasma is a non-equilibrium plasma with $T_{\mathrm{e}} \gg T_{\mathrm{gas}} \approx T_{\mathrm{i}}$.
It is convenient in plasma physics to express temperatures in terms of the energy equivalent unit eV where $1\,\mathrm{eV} \approx 11605\,\mathrm{K}$. Typical electron temperatures in low pressure low temperature plasmas are in the order of eV whereas heavy particle temperatures are usually $\gtrsim 0.04$ to $0.09\,\mathrm{eV}$ (≈ 500 to $1000\,\mathrm{K}$).

Beside a Maxwellian EEDF another prominent form, the so-called *Bi-Maxwellian* EEDF $f_{\mathrm{BM}}(E_{\mathrm{e}})$ can evolve when energy selective heating or loss mechanisms are present that surpass the electron ensembles thermalization.
A Bi-Maxwellian EEDF is a composition of two different Maxwellian distributions comprising two ensembles of electrons namely $n_{\mathrm{e},1}$ and $n_{\mathrm{e},2}$ that are thermalized within each ensemble separately but not as a whole. After [GMS95] a Bi-Maxwellian EEDF can be characterised by the 'temperatures[2]' $T_{\mathrm{e},1}$ and $T_{\mathrm{e},2}$ where $T_{\mathrm{e},1} < T_{\mathrm{e},2}$ and the weighting factor $\beta = n_{\mathrm{e},2}/(n_{\mathrm{e},1} + n_{\mathrm{e},2})$:

$$\begin{aligned} f_{\mathrm{BM}}(E_{\mathrm{e}}) =& \frac{2n_{\mathrm{e}}}{\sqrt{\pi}}\sqrt{E_{\mathrm{e}}}(1-\beta)(k_{\mathrm{B}}T_{\mathrm{e},1})^{-3/2}\exp\left(-\frac{E_{\mathrm{e}}}{k_{\mathrm{B}}T_{\mathrm{e},1}}\right) \\ &+ \frac{2n_{\mathrm{e}}}{\sqrt{\pi}}\sqrt{E_{\mathrm{e}}}\beta(k_{\mathrm{B}}T_{\mathrm{e},2})^{-3/2}\exp\left(-\frac{E_{\mathrm{e}}}{k_{\mathrm{B}}T_{\mathrm{e},2}}\right) \quad . \end{aligned} \tag{3.8}$$

A correlation with the mean electron energy is again given via equation (3.6). Furthermore, an effective electron temperature $T_{\mathrm{e}}^{\mathrm{eff}}$ can be defined via:

$$T_{\mathrm{e}}^{\mathrm{eff}} = (1-\beta)T_{\mathrm{e},1} + \beta T_{\mathrm{e},2} \quad . \tag{3.9}$$

A convenient way of comparing different forms of EEDFs is to calculate the so-called *electron energy probability function* **EEPF** $g(E_{\mathrm{e}}) = f(E_{\mathrm{e}})/\sqrt{E_{\mathrm{e}}}$. De-

[2]Note, a temperature in thermodynamic sense only can be assigned in case of a Maxwellian energy distribution function.

pending on the normalisation to unity or the density, the EEDF is given in units of [$\mathrm{eV}^{-1}\mathrm{m}^{-3}$] or [$\mathrm{eV}^{-1}$] and the EEPFs unit is [$\mathrm{eV}^{-3/2}\mathrm{m}^{-3}$] or [$\mathrm{eV}^{-3/2}$]. For a Maxwellian distribution the logarithm $\ln g(E_\mathrm{e})$ plotted versus E_e represents a linear decrease, with a slope given by $(-k_\mathrm{B}T_\mathrm{e})^{-1}$. In comparison, a Bi-Maxwellian EEPF plotted versus E_e is concave shaped. It has to be noted, also other forms of the electron energy distribution, like the convex shaped, so-called *Druyvesteyn distribution* or *ν-distributions* can evolve when a depletion in the EEDFs high energy tail is given due to characteristic energy levels of relevant collisional partners [DP40, BF94].

3.2 Plasma Generation via ECR

The generation of a plasma discharge is generally achieved by the application of electrostatic fields or electromagnetic waves to a gas. A compilation of the different plasma generation and heating mechanisms can be found in [LL05]. A very efficient way for plasma generation at low pressure is resonant coupling of circular polarised microwaves into a plasma. Therefore, a magnetic field is applied to adjust the gyration frequency of a particle species for matching the microwave frequency and thus allow for the resonant deposition of the injected microwave power. Commonly used in research and industrial applications are electron cyclotron resonance (ECR) heated plasma discharges at a frequency of $f_\mathrm{MW} = \omega_\mathrm{MW}/2\pi = 2.45\,\mathrm{GHz}$. Here a magnetic field of strength 87.5 mT, which can be created by permanent magnets or solenoids is needed for resonant electron coupling ($\omega_\mathrm{MW} = \omega_\mathrm{c,e} \equiv eB/m_\mathrm{e}$), i.e. by matching the introduced frequency and the electron cyclotron frequency $\omega_\mathrm{c,e}$. The absorption of the incoming right-hand circularly polarized wave is thereby increasing the mean energy of the electron ensemble by collisional and collisionless heating mechanisms in the resonance zone [LL05].

Electromagnetic wave propagation within a plasma is generally described by the dispersion relation $\omega(k)$ and the transmission or reflection of an incident wave with frequency ω is dependent on the refractive index N. The refractive index is a function of the *plasma frequency* $\omega_\mathrm{P} = \sqrt{n_\mathrm{e}e^2/(m_\mathrm{e}\epsilon_0)}$. Without any magnetic fields applied, $N = \sqrt{1-\omega_\mathrm{P}^2/\omega^2}$ and wave propagation is possible for $\omega > \omega_\mathrm{P}$. For $N < 0$ a so-called cut-off is present and the incident wave is reflected. A magnetic field modifies the dispersion relation for electromagnetic wave propagation within a plasma. After [Gel96] the refractive index for a right hand circularly polarised

wave is given by: $N^* = \sqrt{1 - [(\omega_{\mathrm{P}}^2/\omega^2)(1 - \omega_{\mathrm{c,e}}/\omega)^{-1}]}$.
In order to prevent wave propagation through a region where a cut-off is present, the microwave is typically injected in ECR discharges via a region with local magnetic field increment (so-called high-field side), where the magnetic field exceeds the one needed for resonant coupling.

3.3 Plasma Processes

3.3.1 Atomic and Molecular States of Hydrogen

The different interactions pathways of the constituents in a hydrogen discharge result in the (re-)distribution of the internal energies of the different reactants. A review of corresponding processes can be found in [JRS03].

For atomic hydrogen distinct electronic states exist. With the Rydberg constant $R_{\mathrm{H}} = 13.6\,\mathrm{eV}$ the internal energy $E_n = R_{\mathrm{H}}(1 - 1/n^2)$ is quantified by the principal quantum number n. A transition between different electronic states is possible by various processes like electron impact excitation from all states below n, heavy particle collisions between atomic hydrogen and other hydrogen species or by optical transitions i.e. emission or absorption of photons.

For the homonuclear hydrogen molecule a by far more complex energy structure arises due to the additional degrees of freedom caused by the relative motion of the two nuclei[3]. The vibration and rotation of the nuclei leads to the existence of further internal energy states and the internal energy of H_2 is given by the sum of electronic, vibrational and rotational energy: $E = E_{el} + E(\nu) + E_\nu(J)$. For each electronic state different vibrational states, characterised by the vibrational quantum number ν and for each vibrational state distinct rotational states characterised by the rotational quantum number J exist. The energy difference between the ground and electronic excited states is typically several eV, whereas the energy difference between different vibrational states is in the order of 0.1 eV and between rotational states in the order of 0.01 eV.
After the Born-Oppenheimer approximation it can be assumed that the nuclei are at rest during electronic transitions, due to the mass difference between the nuclei and electrons. Thus, a separate treatment of the nuclei and electron mo-

[3] A detailed description of the energy levels of molecules can be found e.g. in [Her50].

tion is possible.
The electronic energy states of H_2 split according to the spin rules into a singlet and a triplet state system where no optical transitions between these two systems are allowed by quantum mechanic's selection rules. The vibrational motion of the nuclei is characterised by potential curves, i.e. by functions of the nuclei distance. The complex structure of these functions furthermore depends on the electronic state of the molecule. In the electronic ground state the potential curve can be approximated for example by a Morse-Potential.
The ground state of the H_2 molecule is a binding state, i.e. the potential curve possesses a distinct minimum. This singlet state is termed in the spectroscopic nomenclature[4] with $X^1\Sigma_g^+$. The energetically lowest triplet state is $b^3\Sigma_u^+$ and its potential curve monotonously decreases with increasing nuclei distance, i.e. this state is anti-binding. When a hydrogen molecule in ground state is electronically excited into this repulsive state, the molecule dissociates and two hydrogen atoms in ground state are created.

3.3.2 Plasma Reactions

The variety of processes within a hydrogen plasma like excitation, dissociation or ionisation results in distinct densities of different species and their states. In the following a brief overview of relevant reactions in the plasma volume is presented. This list by far does not claim completeness but is intended to give an idea about the variety of mechanisms that occur in a low pressure hydrogen plasma.

A dominant population channel of electronically excited atomic and molecular hydrogen states (in the following labelled with $H(i,k)$ and $H_2(i,k)$) is given in low pressure, low temperature hydrogen discharges by electron impact excitation out of the corresponding ground states:

$$\mathrm{H}, \mathrm{H}_2 + e_\mathrm{f} \rightarrow \mathrm{H}(i), \mathrm{H}_2(i) + e_\mathrm{s} \quad . \tag{3.10}$$

The indices f and s denote fast and slow electrons. For optically allowed transitions, excited states are primarily depopulated via spontaneous emission into a lower lying electronic state k by emission of a characteristic photon of energy

[4] A description of the spectroscopic nomenclature can be found in [Her50].

$E_{ik} = \mathrm{h} f_{ik}$ where h is the Planck constant and f_{ik} is the photons frequency:

$$\mathrm{H}(i), \mathrm{H}_2(i) \rightarrow \mathrm{H}(k), \mathrm{H}_2(k) + E_{ik} \quad \text{with} \quad i > k. \tag{3.11}$$

Atomic hydrogen is mainly resulting from dissociative excitation via the repulsive $b^3\Sigma_u^+$ triplet state:

$$\mathrm{H}_2 + e_\mathrm{f} \rightarrow \mathrm{H}_2(b^3\Sigma_u^+) + e_\mathrm{s} \rightarrow \mathrm{H} + \mathrm{H} + e_\mathrm{s} \quad . \tag{3.12}$$

The H^+ and H_2^+ positive ions are dominantly formed via electron impact ionisation

$$\mathrm{H}, \mathrm{H}_2 + e_\mathrm{f} \rightarrow \mathrm{H}^+, \mathrm{H}_2^+ + e_\mathrm{s} + e \quad , \tag{3.13}$$

and for the positive molecular ion H_2^+ dissociative recombination with a low energetic electron leads to the formation of a ground state atom and an electronically excited atom:

$$\mathrm{H}_2^+ + e_\mathrm{s} \rightarrow \mathrm{H} + \mathrm{H}(k) \quad . \tag{3.14}$$

The triatomic molecule H_3^+ results from the heavy particle collision of H_2 and H_2^+:

$$\mathrm{H}_2 + \mathrm{H}_2^+ \rightarrow \mathrm{H}_3^+ + \mathrm{H} \quad . \tag{3.15}$$

The formation of negative hydrogen ions proceeds via the dissociative attachment process where a low energetic electron attaches to a vibrationally excited hydrogen molecule in ground state $\mathrm{H}_2(\mathrm{X}, \nu)$ resulting in the formation of a ground state hydrogen atom and a negative hydrogen ion via a transient negative hydrogen molecule ion:

$$\mathrm{H}_2(X, \nu) + e_\mathrm{s} \rightarrow \mathrm{H}_2^- \rightarrow \mathrm{H} + \mathrm{H}^- \quad . \tag{3.16}$$

Additionally to these, corresponding reverse processes and further collisions between atoms, molecules and ions as well as recombinative processes are present in a hydrogen plasma. A detailed compilation can be found in [JRS03].

In a global (0-dimensional) approach, the density of the corresponding process products n_x can be calculated by balancing the different reaction rates $R_{+,-}$ describing the sources and sinks for a population:

$$\frac{dn_x}{dt} = \sum_{\text{sources}} R_+ - \sum_{\text{sinks}} R_-. \tag{3.17}$$

In case of collision processes of heavy particles and/or electrons, a reaction rate R can be calculated by the product of the parent species densities and the so-called *rate coefficient* X. In this case, the rate coefficient is sensitive on the parent species' relative energy E_{rel} and is calculated from the related cross section σ and the corresponding distribution functions for the involved particles. In case of electron collisions, the relative energy can be approximated to equal the electron energy $E_{\mathrm{rel}} \approx E_{\mathrm{e}}$ and thus the rate coefficient is solely dependent on the EEDF:

$$X(\mathrm{EEDF}) = \int_0^\infty dE_{\mathrm{e}} \sigma(E_{\mathrm{e}}) \sqrt{\frac{2E_{\mathrm{e}}}{m_{\mathrm{e}}}} \frac{f(E_{\mathrm{e}})}{n_{\mathrm{e}}} \quad . \tag{3.18}$$

Depending on the process a threshold energy E_{th} like for example the ionisation energy can be present so that $\sigma(E < E_{th}) = 0$ and parent particles of less energy consequently do not affect the resulting products density.
In case of optical transitions, the corresponding reaction rate is dependent on the so-called *Einstein-coefficients*. A depopulation of an initial electronic excited state i is for example linked via the Einstein-coefficient for spontaneous emission A_{ik} with the so-called emissivity $\epsilon_{ik} = \frac{dn_i}{dt}$ via:

$$\epsilon_{ik} = n_i A_{ik} \quad . \tag{3.19}$$

A set of equations of the form of (3.17) allows setting up a 0-dimensional population model (e.g. dissociation, ionisation or collisional radiative models). Via such models the steady-state population density for different particle states or particle densities can be calculated. However, the accuracy is thereby highly sensitive on the available cross section data. Depending on the number of relevant processes various input parameters like $T_{\mathrm{e}}, n_{\mathrm{e}}, ...$ are needed for determining the reaction rates R. In turn, when the population density is known from measurement, these models can be used to identify dominant populating or depopulating processes.

3.3.3 Diffusion and Balances

An important process that affects the population density of particles with sufficiently long lifetimes is given by particle diffusion. This process superimposes the random particle movement and can be driven in case of charged particles by electric fields or generally by present density gradients, caused for example by a particle species production or loss mechanism at a surface like the plasma

surrounding wall. Such surface mechanisms can be for example the adsorption or reformation of atomic hydrogen to hydrogen molecules or the recombination of positive ions to neutrals. For charged particles the quasi-neutrality causes also a diffusion, when a density gradient in an oppositely charged particle density is given via an ambipolar field (so-called ambipolar diffusion).

Following the review of particle diffusion for neutrals and ions by [Möl93] the diffusion rate R of a particle species with density n_x can be represented via a confinement time τ_{conf}:

$$R = n_x/\tau_{\text{conf}} \quad . \tag{3.20}$$

The confinement depends on typical vessel dimensions d given by the ratio of plasma volume V and surrounding surface area A ($d = V/A$) and the mean free path λ_{free}. The latter is defined as the average distance that particles of speed $\langle v \rangle$ travel through a background of particles with a density n_0 between two collisions within a time τ_{coll}. Thus, the mean free path is dependent on the pressure and is furthermore specific for each particle species, i.e. linked to the cross section or the rate coefficient via:

$$\lambda_{\text{free}} = \frac{1}{n_0 \sigma(E)} = \frac{\langle v \rangle}{n_0 \cdot X(E)} = \langle v \rangle \cdot \tau_{\text{coll}} \quad . \tag{3.21}$$

According to the mean free path, the collision frequency ν_{coll} can be defined as the inverse of the average time between two collisions τ_{coll}:

$$\nu_{\text{coll}} = \tau_{\text{coll}}^{-1} \quad . \tag{3.22}$$

Generally, the confinement time is given by $\tau_{\text{conf}} = \frac{\int dV n_x}{\oint d\boldsymbol{A}\boldsymbol{\Gamma}}$ with $\boldsymbol{\Gamma} = n\boldsymbol{v}$ being the particle flux. For a diffusive flux driven by an electric field $\boldsymbol{E}$ and a density gradient ∇n_x, $\boldsymbol{\Gamma}$ can be furthermore written as:

$$\boldsymbol{\Gamma} = \mu n_x \boldsymbol{E} - D \nabla n_x \quad . \tag{3.23}$$

Here, D is the so-called diffusion coefficient, defined for particles of mass m and temperature T by

$$D = \frac{k_{\text{B}} T}{m \nu_{\text{coll}}} \tag{3.24}$$

and $\mu = q m^{-1} \nu_{\text{coll}}^{-1}$ is the mobility of the diffusing particles with charge q. In case of $\lambda_{\text{free}} \ll d$ the **diffusion is laminar**, i.e. dominated by particle collisions

within the plasma volume and the confinement time $\tau_{\mathrm{conf}}^{\mathrm{lam}}$ is [Möl93]:

$$\tau_{\mathrm{conf}}^{\mathrm{lam}} = \frac{\Lambda^2}{D} \quad , \tag{3.25}$$

where Λ is a characteristic diffusion length (see below). In case of neutral particle diffusion, equation (3.23) simplifies to $\mathbf{\Gamma} = -D\nabla n_x$ and the diffusion coefficient in equation (3.25) is given by the normal diffusion coefficient D_n. After [HCB64] the normal diffusion coefficient for neutral particles diffusing through a background of particles with mass m_0 and of same temperature is:

$$D_n = \frac{3\sqrt{\pi}}{8}\lambda_{\mathrm{free}}\sqrt{k_{\mathrm{B}}T_{\mathrm{gas}}\frac{m+m_0}{2mm_0}} \quad . \tag{3.26}$$

For charged particle diffusion, the ambipolar electric field couples positive ion and negatively charged particle diffusion and the positive ion flux $\mathbf{\Gamma}_+$ equals the sum of electron $\mathbf{\Gamma}_{\mathrm{e}}$ and negative ion flux $\mathbf{\Gamma}_-$: $\mathbf{\Gamma}_+ = \mathbf{\Gamma}_{\mathrm{e}} + \mathbf{\Gamma}_-$. In a low temperature, low pressure plasma with electrons being the only negatively charges particle species and with $T_{\mathrm{e}} \gg T_{\mathrm{i}} \approx T_{\mathrm{gas}}$, this transforms to $\mathbf{\Gamma}_+ = \mathbf{\Gamma}_{\mathrm{e}}$. As electrons are characterised by a higher velocity then positive ions (mass and temperature difference), an electrical field evolves that accelerates the positive ions and decelerates the electrons until the flux is ambipolar. The corresponding ambipolar diffusion coefficient D_a is given by [TL29]:

$$D_a = \frac{3\sqrt{\pi}}{8}\frac{T_{\mathrm{e}}}{T_{\mathrm{gas}}}\lambda_{\mathrm{free}}\sqrt{k_{\mathrm{B}}T_{\mathrm{gas}}\frac{m_{\mathrm{i}}+m_0}{2m_{\mathrm{i}}m_0}} \quad , \tag{3.27}$$

with m_{i} being the mass of the diffusing positive ion.
In the presence of negative ions within the plasma, the ambipolar diffusion coefficient is modified due to the additionally diffusing negatively charged particles with high mass, i.e. the negative ions. After [LVL+94] the modified ambipolar diffusion coefficient D_{a+} can be expressed by:

$$D_{a+} = \frac{k_{\mathrm{B}}T_{\mathrm{gas}}}{m_{\mathrm{i}}\nu_{\mathrm{coll}}^{+}}\frac{1+\gamma+2\gamma\alpha}{1+\gamma\alpha} \quad , \tag{3.28}$$

with $\gamma = T_{\mathrm{e}}/T_-$ and $\alpha = n_-/n_{\mathrm{e}}$, where T_- and n_- are the temperature and density of the negative ions respectively and ν_{coll}^{+} the collisional frequency of positive ions.

The characteristic diffusion length Λ in equation (3.25) depends on the plasma

geometry. For a finite cylindrical vessel with radius R and height H, Λ can be approximated by [Möl93]:

$$\frac{1}{\Lambda^2} = \left(\frac{2.405}{R}\right)^2 + \left(\frac{\pi}{H}\right)^2 \quad . \tag{3.29}$$

A modification of Λ was introduced by [Cha87] in order to address the effect of a wall not being an ideal sink for a neutral particle i.e. a finite reflection probability is present. Such a particle **sticking** is relevant for example for atomic hydrogen and can be accounted via an enlarged characteristic diffusion length $\tilde{\Lambda}$:

$$\tilde{\Lambda}^2 = \Lambda^2 + \alpha d \quad \text{with} \quad \alpha = \frac{2}{3}\lambda_{\text{free}}\frac{2-s}{s} \quad , \tag{3.30}$$

with the so-called *sticking coefficient* $s \in [0, 1]$.

At low pressure, i.e. for $\lambda_{\text{free}} \gg d$ the **diffusion is called molecular** and wall collisions dominate. In this case, the confinement time is given by the ratio of a characteristic length $\Pi = 2d$ and the mean velocity $\langle v \rangle$:

$$\tau_{\text{conf}}^{\text{mol}} = \frac{\Pi}{\langle v \rangle} \quad . \tag{3.31}$$

Again a modification due to a particle sticking can be addressed by a modified effective length $\tilde{\Pi} = 2d(2-s)/s$.

The presence of a **magnetic field** leads to an increased confinement of charged particles moving perpendicular to the field lines. While the velocity component along the field lines is unaffected, a transport perpendicular to the magnetic field is only possible due to collisions allowing a charged particle to shift its cycloidal motion from line to line [CB11]. A characteristic length scale for shifting from one line to another is thereby given by the radius of the cycloidal motion.
Assuming a strong magnetic field where the gyration radii of charged particles are significantly lower than typical vessel dimensions, the diffusion coefficient for a charged particle moving perpendicular to this magnetic field $D_\perp$ is [LL05]:

$$D_\perp = \frac{k_{\text{B}} T \nu_{\text{coll}}}{m \omega_{\text{c}}} \quad . \tag{3.32}$$

Here, ν_{coll} denotes the collision frequency of electrons or ions with particles leading to a cycloidal shift and ω_{c} the corresponding cyclotron frequency. Assuming

electrons being the only negatively charged particle species, the ambipolar diffusion coefficient perpendicular to a magnetic field $D_{\perp a}$ can be approximated by [LL05]:

$$D_{\perp a} \approx D_{\perp \mathrm{e}} \left(1 + \frac{T_\mathrm{e}}{T_i}\right) \quad . \tag{3.33}$$

Here, the diffusion coefficient for electrons $D_{\perp \mathrm{e}}$ is given via equation (3.32). The diffusion length Λ in the presence of a magnetic field can then be expressed by [Rot95]:

$$\frac{1}{\Lambda^2} = \left(\frac{2.405}{R}\right)^2 \frac{\nu_\mathrm{coll}^2}{\nu_\mathrm{coll}^2 + \omega_\mathrm{ce}^2} + \left(\frac{\pi}{H}\right)^2 \quad . \tag{3.34}$$

Ionisation balance

In low temperature, low pressure plasmas positive ions are dominantly produced via electron impact ionisation and lost via diffusion and subsequent recombination on the plasma confining walls [Beh91]. By balancing these two processes, a qualitative behaviour of the electron temperature can be obtained. Assuming a Maxwellian EEDF and only one positive ion and neutral particle species of densities $n_{\mathrm{i}+}$ and n_0 equation (3.17) yields in steady state:

$$n_\mathrm{e} n_0 X_\mathrm{ion}(T_\mathrm{e}) = \frac{n_{\mathrm{i}+}}{\tau_\mathrm{conf}} \quad , \tag{3.35}$$

where $X_\mathrm{ion}(T_\mathrm{e})$ is the corresponding ionisation rate coefficient. Due to the quasi-neutrality n_e and $n_{\mathrm{i}+}$ cancel out. As X_ion is very sensitive on electron temperature variations, the inverse linear dependence of τ_conf on T_e can be neglected and equation (3.35) can be rewritten:

$$X_\mathrm{ion}(T_\mathrm{e}) \propto \frac{\lambda_\mathrm{ion}}{n_0 \sqrt{m_\mathrm{i}}} \quad . \tag{3.36}$$

Thus, the particle diffusion is correlated with the present electron temperature within a discharge: Influencing the particle diffusion by increasing the mean free path, e.g. by decreasing the pressure, is balanced by a higher ionisation rate coefficient. Consequently a higher electron temperature arises, needed to balance the loss of positive ions at a surface. In turn, a lower diffusion e.g. given for a heavier particle results in a lower electron temperature. In case of more than one neutral and ion species, equation (3.35) has to be modified by the sum of the corresponding densities, ionisation rate coefficients and confinement times.

3.4 Sheath Formation

A plasma facing a surface like the plasma confining wall results in the formation of a transition region between the bulk plasma and the wall. This transition region is composed of a pre-sheath and a sheath region. In a low pressure, low temperature plasma, the flux of positive ions towards a surface would be significantly smaller compared to the electron flux due to the different particle temperatures and masses. Thus, to fulfil quasi-neutrality in steady state the potential of the plasma relative to the surface is increased to balance the charged particle fluxes. This potential difference accelerates positively charged particles and decreases the electron flux. The arising density and potential profiles obey the Poisson's equation and are depicted schematically as a function of distance in figure 3.1. Within the pre-sheath region positive ions are accelerated to the so-called Bohm velocity

$$v_{\mathrm{B}} = \sqrt{\frac{k_{\mathrm{B}} T_{\mathrm{e}}}{m_i}} \quad . \tag{3.37}$$

This velocity is the minimum speed of positive ions with density n_{i+} required to fulfil flux equality within the sheath region. Accordingly, the positive ion flux can be assessed via

$$\Gamma_{\mathrm{B}} = n_{i+} v_{\mathrm{B}} \quad . \tag{3.38}$$

In the vicinity of the surface, i.e. the sheath region, quasi-neutrality is no longer fulfilled and the electron density decreases more pronounced than the positive ion density. The dimensions of the sheath and pre-sheath are quite different. While the thickness of the sheath is in the order of a few Debye lengths, the pre-sheath dimension is linked to the mean free path of positive ions that is in low pressure, low temperature plasmas in the range of few mm to cm. In physics textbooks (e.g. [LL05, CB11]) commonly the potential evolution is calculated relative to the sheath edge, i.e. the transition between pre-sheath and sheath region, defining at this location $\phi \equiv 0$. The potential difference between the undisturbed bulk plasma and this sheath edge is called plasma potential $\phi_{\mathrm{pl}}$and can be represented by:

$$\phi_{\mathrm{pl}} = \frac{k_{\mathrm{B}} T_{\mathrm{e}}}{2\mathrm{e}} \quad . \tag{3.39}$$

In case of the surface being insulated, i.e. is electrically floating, the fluxes of positively and negatively charged particles are towards this surface balanced. The potential of the surface is the so-called floating potential ϕ_{fl} is can be represented

relative to the sheath edge potential where $\phi \equiv 0$ as:

$$\phi_{\mathrm{fl}} = \frac{1}{2}\frac{k_{\mathrm{B}}T_{\mathrm{e}}}{\mathrm{e}} \ln\left(\frac{2\pi m_{\mathrm{e}}}{m_i}\right) \quad . \tag{3.40}$$

As shown in figure 3.1, the potential difference between bulk plasma and sheath edge is significantly smaller then between the sheath edge and the floating wall. Exemplary, for an electron temperature of 1 eV in a plasma with H_2^+ being the dominant positive ion species the potential difference between the bulk plasma and the sheath edge is ≈ 0.5 V whereas the potential drop within the sheath is $\approx$ 3.2 V. In many cases of experimental applications, the potentials are considered

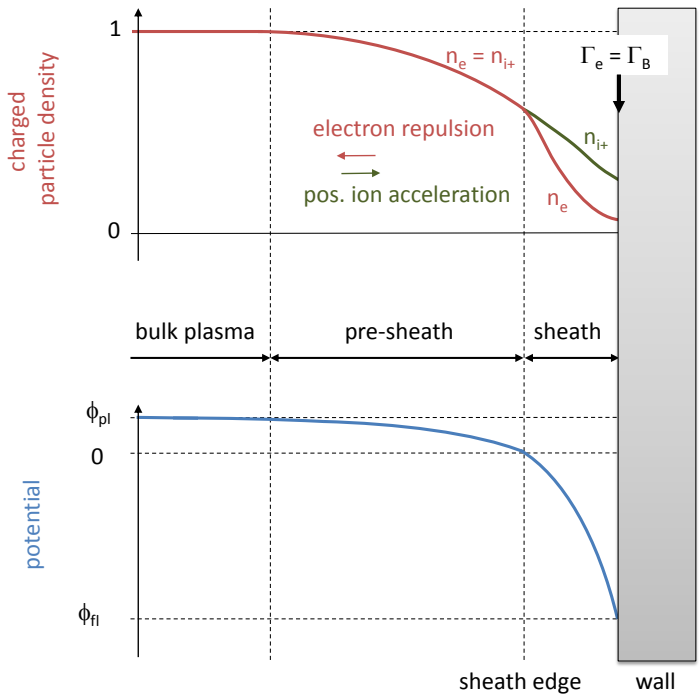

Figure 3.1: *Schematic density and potential profile as a function of distance to a floating surface after [LL05].*

relative to a grounded surface, e.g. the experimental vessel walls. The plasma and floating potentials shift correspondingly, i.e. the potential difference between the bulk plasma and an insulated surface $\phi_{\mathrm{pl}} - \phi_{\mathrm{fl}}$ is conserved. It has to be pointed out that for a large conducting surface like a vacuum vessel made of stainless steel, the balance of the overall fluxes can include compensating currents within the walls and local fluxes onto a wall do not have to be in balance.

When additionally to electrons **negatively charged ions** are present, the tran-

sition region between the bulk plasma and a wall can be modified depending on the amount of negative ions relative to the electron density $\alpha = n_{i-}/n_{\mathrm{e}}$, the corresponding temperature ratio $\gamma = T_{-}/T_{\mathrm{e}}$ and the region of origin for negative ions, i.e. volume or surface produced.
Fluxes of positive ions onto a floating surface balance the flux of all negatively charged particles. For volume produced negative ions, their higher mass compared to electrons leads to a decreased negative particle flux coming from the volume assuming $\gamma \geq 1$. After [CB11, SCB99], negative ions are well confined within the plasma volume except for $\alpha \ll 1$ and a lower positive ion flux is required to balance this negative particle flux. Thus, a lower potential difference between the bulk plasma and the sheath edged accelerates the positive ions to the Bohm velocity. After [CB11] the Bohm velocity $v_{\mathrm{B}}*$ in the presence of negative ions in the plasma bulk can be represented by:

$$v_{\mathrm{B}}* = v_{\mathrm{B}}\sqrt{\frac{1+\alpha_{\mathrm{s}}}{1+\gamma\alpha_{\mathrm{s}}}} \quad , \tag{3.41}$$

where α_{s} is the density ratio at the sheath edge that can be approximated by $\alpha_{\mathrm{s}} = \alpha \exp(e\phi_{\mathrm{pl}}/(k_{\mathrm{B}}T_{\mathrm{e}})(1-\gamma))$. Furthermore, the Debye length is reduced, given by [LL05]:

$$\lambda_{\mathrm{D}}* = \lambda_{\mathrm{D}}\sqrt{\frac{1}{1+\gamma\alpha}} \quad . \tag{3.42}$$

In the presence of surface produced negative ions, the sheath topology has to balance fluxes coming from the plasma volume directed to the surface and the negative ion flux directed into the plasma. The treatment is generally more complex and specific particle-in-cell (PIC) codes have to be applied for individual scenarios. For the purpose of a negative ion source based on H^- surface formation induced by the application of caesium, the sheath topology and density profiles were investigated via a PIC code by [WGF09]. While the H^- density monotonously decreases from its highest value in the vicinity of the surface with increasing distance, the density profiles of positive ions and electrons evolve comparable to the case of a classical transition region shown in figure 3.1. However, in the presented case, surface formation of negative ions predominantly proceeds via atomic particle conversion and it was found that in this case a potential well in the vicinity of the surface can result depending on the amount of surface produced negative ions and the flux of positive ions. For a high amount of surface produced negative ions and an insufficient flux of positive ions to fulfil quasi-neutrality, the

evolving potential well can hinder the transport of surface produced negative ions into the bulk plasma and thus a space charge limitation for the emission of surface produced negative ions is given.

4 Negative Hydrogen Ions

4.1 Formation and Destruction Mechanisms

The negative hydrogen ion density in a plasma is a consequence of formation and destruction mechanisms. Generally, surface and volume processes can be distinguished. While negative ion formation can proceed via mechanisms at a surface as well as within the plasma volume, the destruction is mainly given by volume processes. The minor relevancy of surface related destruction mechanisms is a consequence of the repelling sheath potentials present at the plasma boundaries, confining negative ions within the plasma volume. However, obviously a relevant loss channel can be given by neutralisation of negatively charged particles at surfaces when those are bias positively e.g. when electrodes are used and a negative ion attracting sheath is formed.

4.1.1 Volume Formation

As described in section 3.3.2, the formation of negative hydrogen ions in the plasma volume proceeds via the *dissociative attachment* process DA:

$$\mathrm{H_2(X,\nu) + e \rightarrow H_2^- \rightarrow H + H^-}. \tag{4.1}$$

The rate coefficient, calculated on basis of cross sections after [JRS03] and a Maxwellian EEDF is shown in figure 4.1. A strong dependency on the initial vibrational state is given by which X_{DA} increases with increasing vibrational quantum number. The relative position of vibrational states in the electronic ground state and the transient negative ion molecule and the linked transition probabilities cause that this increment is most pronounced for $\nu \leq 5$ in the case of hydrogen and for $\nu \leq 8$ for deuterium [JRS03, BW79]. At $T_{\mathrm{e}} = 1\,\mathrm{eV}$ the rate coefficient for dissociative attachment rises by more than four orders of magnitude from $\nu = 0$ to $\nu = 5$ for hydrogen and up to seven orders of magnitude for $\nu = 0$ to $\nu = 8$ for deuterium. For higher vibrational states the rate coefficient

furthermore increases. With increasing electron temperature, the formation rate via dissociative attachment decreases and the process is most efficient for low energetic electrons.

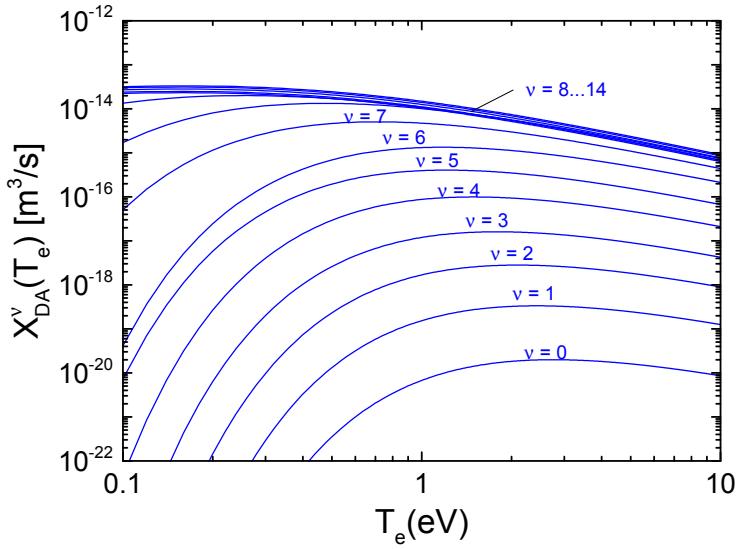

Figure 4.1: *Rate coefficient for dissociative attachment calculated on basis of a Maxwellian EEDF and cross section data after [JRS03].*

The rate of producing negative ions via the dissociative attachment process is given after equation (3.17) by:

$$R_{DA} = \sum_{\nu} n_{\mathrm{e}} n_{\mathrm{H_2(X,\nu)}} X^{\nu}_{\mathrm{DA}}(T_{\mathrm{e}}) \quad . \tag{4.2}$$

Thus, a high volume production rate for negative ions is given for high electron densities at low temperature and a high amount of highly vibrationally excited molecules $\mathrm{H_2(X,\nu)}$. The population density of a certain vibrational state can be calculated by the product of the ground state molecular hydrogen density $n_{\mathrm{H_2}}(X)$ and the relative vibrational population coefficient P_ν:

$$n_{\mathrm{H_2(X,\nu)}} = n_{\mathrm{H_2}}(X) P_\nu \quad , \tag{4.3}$$

where $\sum_\nu P_\nu = 1$. For the population of the vibrational states being Boltzmann distributed, the relative vibrational population coefficient can be described via a

vibrational temperature T_{vib}:

$$P_\nu = \frac{\exp\left(-\Delta E_\nu / k_{\mathrm{B}} T_{\mathrm{vib}}\right)}{\sum_\nu \exp\left(-\Delta E_\nu / k_{\mathrm{B}} T_{\mathrm{vib}}\right)} \quad , \tag{4.4}$$

with the corresponding energy difference $\Delta E_\nu = E_\nu - E_{\nu=0}$. In general, the population distribution is determined by numerous mechanisms in the plasma volume as well as by plasma wall interaction (see sections 3.1 and 4.1.2) and deviations from a Boltzmann distribution can arise.
A significant source for producing highly vibrationally excited molecules is given by collisions of high energetic electrons with hydrogen molecules in the electronic ground state [His80, Gra84, Bac06]. For sufficient electron energy, ground state molecules are excited into the singlet $\mathrm{H_2(B}, \nu)$ and $\mathrm{H_2(C}, \nu)$ states. By a subsequent radiative decay, vibrationally excited molecules in electronic ground state $\mathrm{H_2(X}, \nu'')$ can be formed:

$$\mathrm{H_2(X}, \nu) + e_{\mathrm{f}} \rightarrow \mathrm{H_2(B}, \nu), \mathrm{H_2(C}, \nu) + e_{\mathrm{s}} \rightarrow \mathrm{H_2(X}, \nu'') + \mathrm{h}f + e_{\mathrm{s}} \quad , \tag{4.5}$$

where $\mathrm{h}f$ denotes the energy of the emitted photon. For collisions between low energetic electrons and $\mathrm{H_2}(X, \nu)$ an alternative to the dissociative attachment process represents the change of the ground state hydrogen molecule's vibrational state. After [Bac06] this process results most probable in a change of ν by ± 1. Thus, for an initially pronounced population of the $\nu = 0$ state, a high collision rate is requisite for a significant population of vibrationally highly excited states. The dissociative attachment process itself represents a significant depopulation channel for vibrationally highly excited hydrogen molecules in low temperature, low pressure hydrogen plasmas [WF01]. Furthermore, vibrationally excited states are depopulated by de-exciting collisions of $\mathrm{H_2(X}, \nu'')$ with atoms and other molecules. Thereby, vibrational energy is transferred to translational energy.

Since the distribution in steady-state can be calculated by 0-dimensional population models, which allows for investigating the influence of different population mechanisms, the vibrational population of $\mathrm{H_2}(X, \nu)$ has been calculated for a low pressure low temperature hydrogen plasma by [Wün14] for two different electron temperatures namely 1 and 4 eV via the collisional-radiative model *Yacora* H_2. A description of the model and included processes can be found in [WF01, Wün04]. The Boltzmann plot of the corresponding relative population is depicted in figure 4.2. For $T_{\mathrm{e}} = 1\,\mathrm{eV}$ the distribution is linearly decreasing with a slope given

by $-1/k_{\mathrm{B}}T_{\mathrm{vib}}$ where $T_{\mathrm{vib}} \approx 7000\,\mathrm{K}$. However, for $T_{\mathrm{e}} = 4\,\mathrm{eV}$ a deviation from a linear decrease starting at $\nu \approx 5$ can be seen showing an overpopulation of the higher vibrational levels. Like in the case of a Bi-Maxwellian EEDF (see equation (3.8)) this population can be described by the combination of two distribution functions with different 'vibrational temperatures' being $T_{\mathrm{vib},1} \approx 4500\,\mathrm{K}$, $T_{\mathrm{vib},2} \approx 15000\,\mathrm{K}$ and a weighting factor of 5 %. As can be furthermore seen, artificially excluding the redistribution via the singlet states $\mathrm{H}_2(\mathrm{B},\nu)$, $\mathrm{H}_2(\mathrm{C},\nu)$ results in a lower population of vibrationally highly excited states.

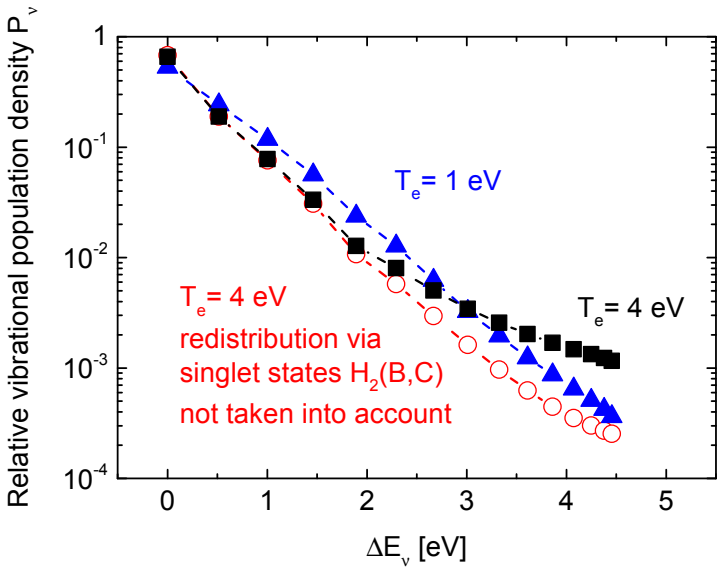

Figure 4.2: *Relative vibrational population density of $H_2(X,\nu)$ versus energy difference between energy eigenvalues of distinct vibrational states E_ν and $E_{\nu=0}$ calculated via Yacora H_2 by [Wün14] for $T_{\mathrm{e}} = 1$ and 4 eV. In a particular case study the influence on the population of highly excited vibrational levels by electron impact excitation is shown by artificially excluding these channels for $T_{\mathrm{e}} = 4$ eV.*

It has to be noted that for efficient negative ion formation within the plasma volume a high amount of vibrationally highly excited molecules and consequently high electron temperatures are needed. However, for a high rate of H^- formation via the dissociative attachment process low electron temperatures are needed as well. For solving this discrepancy, the so-called tandem-principle is applied in negative ion source design i.e. the source volume is providing distinct volumes with hot and cold electrons. This concept will be described in section 4.2.

4.1.2 Surface Assisted Formation

For the formation of negative ions via the interaction of a particle with a surface, generally two cases have to be distinguished:

- An indirect mechanism by enhancing the volume production, i.e. a two step process. Thereby vibrationally excited hydrogen molecules are catalytically produced at the surface and are subsequently transformed into negative ions via dissociative attachment in the plasma volume.
- A direct formation of a negatively charged particle by an electron transfer from the surface into the atomic particles affinity level that is in the vicinity of the surface.

Surface Supported Production of Negative Ions

The catalytic formation of vibrationally excited $H_2(X, \nu'')$ on a surface, i.e. the precursor species for the dissociative attachment process can basically be described via a three body reaction of the form

$$\mathrm{H} + \mathrm{H} + \mathrm{surface} \rightarrow \mathrm{H}_2(\mathrm{X}, \nu'') + \mathrm{surface} \quad . \tag{4.6}$$

The interaction is sensitive to the surface material, its structure, its purity and the binding energy of potential adsorbates. In literature there are numerous investigations focused on the effect on the vibrational population of desorbing hydrogen molecules for hydrogen gas as well as hydrogen plasmas interacting with different surface materials (see for instance [HCL+88, EBL+88, SPL+94, BIG+04]). An enhancing effect on the population of vibrationally excited molecules was found for example by [HCL+88, SPL+94, BIG+04] with tantalum and tungsten, two refractory metals that can be immersed to an ion source plasma.
Although investigated by various groups, the underlying mechanism for the formation of vibrationally highly excited molecules at different surfaces is still subject of on-going discussions. In the following a brief overview of the proposed pathways will be presented:
It is discussed that the underlying mechanism is either a direct formation of vibrationally excited molecules due to recombinative desorption via the Eley-Rideal (ER) or the Langmuir-Hinshelwood (LH) catalytic process or via a third possibility, the so-called *hot-atom* (HA) process[1]. A main difference between the

[1] A review of these processes can be found for instance in [BMT90].

proposed pathways is the amount of energy that can be transferred into internal and translational energy of the desorbing molecule.
In the ER process a chemisorbed H atom reacts directly with an impinging H atom, resulting in the immediate formation of a hydrogen molecule that subsequently desorbs. The internal energy of the resulting molecule is depending on the translational energy of the impinging atom and the binding energy for chemisorption [HK81]. According to [SPL+94], a maximal excitation of vibrational levels of up to $\nu'' = 4$ (2.17 eV) is possible for the ER process when hydrogen interacts with a metal surface, assuming a maximal energy of 2.24 eV for the free atom coming from the Franck-Condon Energy of a H_2 dissociating via the repulsive $b^3\Sigma_u^+$ state.
By [SPL+94] it was proposed that the formation of vibrationally highly excited molecules is related to the reaction of impinging hydrogen atoms with more loosely bound hydrogen atoms rather than chemisorbed ones. Such atoms are assumed to be physisorbed onto a layer of prior chemisorbed H atoms, so less energy is lost by breaking the binding between the trapped particle and the substrate and subsequently higher vibrational levels of the desorbing molecule can be populated.

In case of the LH process, two H reactants are in a chemisorbed state on the surface, capable to reformate on the surface e.g. when they are on adjacent surface sites. For this pathway the reformation process has to take energy from the bulk heat bath of the solid e.g. via electron-hole or phonon de-excitation and the formed molecule can subsequently desorbe in a vibrationally excited state depending on the energy provided by the solid [HK81, Chr88]. However, since the chemisorption potential of the two H atoms is quite deep (eV range), typically less energy is left for the vibrational excitation and consequently, only low vibrational states are expected to be populated [SPL+94].

The HA process can be seen as a process between the two extremes represented by the ER and the LH process. In this case, prior to the formation and desorption of vibrationally excited molecules a certain amount of incident H atoms are trapped in the chemisorption potential well (which is periodic in the surface plane). Due to the periodic potential, the trapped hydrogen atoms can be highly delocalized [PNM+83, Chr88]. These initial atoms are so-called *hot* atoms, when they possess a high kinetic energy parallel to the surface plane that can result for example from a high impinging energy in combination with the finite time span

for thermalization between the solid and such an ad-particle [HK81]. These hot atoms are capable to diffuse across the surface and a reformation can occur like in case of the LH process with another chemisorbed H atom or like in case of the ER process, by picking up another impinging H atom. In both cases and in contrast to the pure ER or LH process, an additional amount of energy is provided by the hot atom [HK81, Chr88].

A fourth alternative was proposed by [BIG+04], where investigations were directly focused on an enhancement of the negative ion volume formation in a negative ion volume source by modifying the stainless steel wall material by evaporating filaments made of tantalum and tungsten. Together with the results reported in [BGI+02], the authors propose the formation of vibrationally highly excited molecules to be given by a three step process: First vibrationally excited molecules with $\nu'' = 1$ and 2 are formed by recombinative desorption on the tantalum or tungsten covered walls. These 'precursor' $H_2(X, \nu'' = 1, 2)$ states can be excited within the bulk plasma volume via electron impact excitation into the singlet $H_2(\mathrm{B}, \nu)$, $H_2(\mathrm{C}, \nu)$ states and subsequently, higher vibrationally excited $H_2(X, \nu'')$ states are populated when these electronically excited states are relaxing via optical transitions. The description is based on the fact that within the investigations reported in [BGI+02] a higher population of excited $H_2(B, \nu)$ states was deduced via VUV spectroscopy in combination with a higher negative ion density when a tantalum covered wall was compared to tungsten covered wall. Although this pathway is possible from an energetic point of view, it has to be mentioned that the enhancement of excited $H_2(B, \nu)$ states could not be reproduced by the very same group in a later experimental campaign as reported in [BIG+04].
The identification of a material induced enhancing effect on the vibrational population of H_2 in a plasma environment is aggravated since additionally to the wall effects, numerous effects in the plasma volume determine the steady-state vibrational population.
By [HF01] the effect of tungsten was investigated in a low pressure hydrogen plasma environment. The authors found no enhancing effect on the vibrational population when a bulk tungsten sample was compared to stainless steel sample and moreover virtually the same vibrational temperatures were determined. This is in contradiction of the results reported by [SPL+94], where tungsten had an increasing effect on the vibrational population, but in gas phase experiments.

For tantalum and/or tungsten further investigations regarding directly the effect on negative hydrogen ions were performed in negative ion sources or corresponding test facilities by [LEP85, IMO+92, GBD+05]. Also in these investigations partly inconsistent or even contrary results were gained and the effects were explained by different approaches, all not related to any of the above mentioned ones. Briefly, higher negative ion yields were measured by [LEP85] when they installed tungsten rods in their experimental setup compared to tantalum and both metals resulted in a more enhanced negative ion yield than with stainless steel rods. The authors discuss this as a consequence of different secondary electron emission properties of the respective metals (stainless steel higher than the others) which increases the amount of high energetic electrons in their arc discharge that is in turn linked to an increased H^- destruction. In contrast, [IMO+92] has measured higher negative ion yields when the wall material was covered with tantalum than with tungsten, which they explained by different sticking coefficients for atomic hydrogen on the wall that subsequently differently affects the vibrational distribution of H_2. By [GBD+05] a diminishing effect on the extracted H^- current has been reported when a meshed grid (see section 4.2) manufactured of stainless steel was exchanged by one made of tantalum. However, no further explanation for this effect was given.

To summarize, different authors have measured the formation of vibrationally excited H_2 desorbing from different surfaces in gas phase and plasma environment, where different pathways for the formation process were described. In the context of negative ion formation these investigations are of relevance, since these $H_2(X, \nu'')$ are precursors for the dissociative attachment process. However, promising materials like tantalum or tungsten have resulted in partially inconsistent results and further experiments are necessary to investigate their effect on the negative ion density in the context of efficient negative ion formation.

Direct Surface Production of Negative Ions

Negative hydrogen ion surface formation is basically given by the transition of one or two electrons from occupied states within a solid into the energy levels of an atomic hydrogen particle being in the vicinity of the solid[2]. The process is thereby depending on the energetic structure of the solid (binding energy of

[2]The following descriptions are based on the concepts presented in [BN81, RWL82, WSA97], which are reviewed in [BW15] and [Win02, BE00, LG90] for example.

electrons, present band gaps and surface states,...) as well as on the position of the particle's affinity level relative to the level of occupied states within the solid. For hydrogen, the electron affinity E_A, i.e. the binding energy of the additional electron, at infinity is 0.75 eV.
The particle to be transformed can either be initially adsorbed at the surface and ejected as a negative ion via sputtering or an impinging particle can be directly converted to a negative ion and backscattered from the surface. For the latter case, the impinging particle can be a neutral atomic hydrogen or an atomic positive ion[3].
Basically, specific probabilities characterise the negative ion formation and the survival of formed negative ions in the outgoing trajectory. In case of a positive ion impinging onto the surface, the probability for negative ion formation is furthermore superimposed by a finite probability for the neutralisation process that proceeds either via resonant charge transfer or Auger-Neutralisation and a sequential or a simultaneous transition of two electrons is possible [BE00].
After formation, the negative ion can lose the incorporated additional electron back into the solid. This is correlated with the retention time of the formed negative ion in the vicinity of the surface. As the retention time is correlated with the translational energy of the particle, the net probability for negative ion formation is sensitive on the particles translational energy.

Direct negative hydrogen ion surface production in present negative ion sources for NNBI, proceeds via the conversion of positive ions and neutral atomic hydrogen impinging onto a metal converter surface i.e. the plasma grid. The plasma grid is therefore coated with an alkali metal (caesium) for reducing the surface's work function which allows for an efficient particle conversion.
Negative hydrogen ion formation has been furthermore found by different authors after formation at diamond surfaces [WSA97, GD99, HLU+01, KAP+11, APC+14] and diamond can consequently be seen as a potentially relevant material for being a caesium-free alternative grid material.
The physical properties of metals and diamonds significantly differ and consequently also the mechanisms for the formation of negative ions are supposed to be different. In the following negative ion formation at metals as well as at diamonds will be further described.

[3]Molecular ions are supposed to dissociate in front of a surface as has been reported by [IKS92, TKH+97, WSH85].

Formation at Metal Surfaces

In figure 4.3 a schematic of the energetic level diagram of an atomic hydrogen particle approaching in front of a metal surface is shown, illustrating the surface formation of negative ions at a metal surface.

For an approaching hydrogen atom, the affinity level is shifted downwards due to an attractive interaction with an induced image charge within the metal. Additionally, the affinity level broadens as a consequence of the coupling between electronic states within the metal and the affinity level (indicated by the evolution of the two blue lines in figure 4.3). As soon as the affinity level is comparable or below the Fermi Energy E_{F}, the tunnelling probability of a metal electron into the affinity level is significantly enhanced. The transition rate for the electron correlates with the width of the affinity level and furthermore with the energy difference between the affinity level and the Fermi energy.

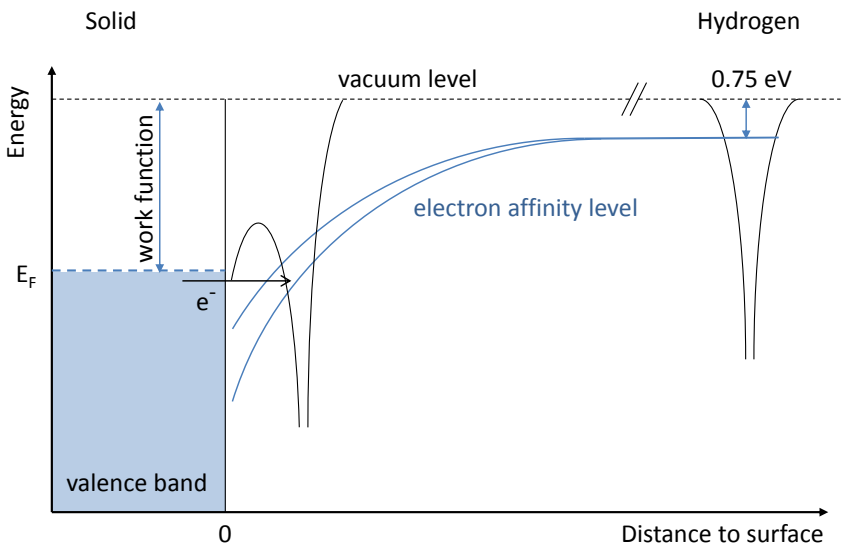

Figure 4.3: *Schematic of the energy levels for negative hydrogen ion formation at metal surfaces including the level shift and broadening of the affinity level.*

The difference between the vacuum level and the Fermi level of the solid state is given by the material's work function χ. After the so-called amplitude model [NL79], the formation probability for a negative ion β^- can be expressed as a function of the material's work function, the affinity level E_{A} and the normal velocity component relative to the surface plane of the negative hydrogen ion v_{H^-} [BN75]:

$$\beta^- \propto \frac{2}{\pi} \exp\left(-\frac{\phi - E_{\mathrm{A}}}{C v_{\mathrm{H}^-}}\right). \tag{4.7}$$

In equation (4.7) C is an exponential decay constant of the transition rate depending on the surface structure. Since a higher velocity v_{H^-} is correlated with an decreased dwelling time of the formed negative ion in the vicinity of the surface, the destruction of the formed negative ion is reduced and thus, the formation probability β^- is generally increased. The combination of the formation and the destruction probability given in equation (4.7) is why this probability is also called *net formation probability*.
For all refractory metals the work function is of the order of up to 5 eV [Mic77]. By covering the metal with an alkali metal, a significant reduction of a materials work function can be induced [Lan71] and thus the formation probability can be enhanced. Therefore, preferentially caesium is applied, which has as a bulk material the lowest work function of applicable alkali metals, namely 2.14 eV [Mic77]. When coated with a sub-monolayer of caesium, a reduction of the converter metals work function down to 1.44 eV has been reported by [Wil66a, Wil66b]. The consequent increment of the negative ion yield has been demonstrated by [BDD74, LS92] and [IKS92] for example and this technique is commonly used in present NNBI systems and respective test stands [SFF+06].

However, regarding caesium-free alternative grid materials, other materials characterised by a low work function can be seen as a potentially suitable alternatives for being a grid material and are therefore investigated within this work.

Formation at Diamond Surfaces
Negative hydrogen ion formation at diamond surfaces has been reported by [WSA97, GD99, HLU+01], measured in scattering experiments. And also in a low density hydrogen plasma [KAP+11] and [APC+14] have measured negative ions after formation at diamond and boron doped diamond materials. However, compared to studies on negative hydrogen ion formation on metal surfaces, investigations performed on insulating materials are generally '*fairly scarce*' [BE00] and hence theoretical models describing the formation process are less matured. Especially in case of diamond, the actual mechanism is not known at present.

The energetic structure of diamond differs from metals and for example the Fermi level lies in case of metals within the conduction band, while it is for diamond within a band gap that separates the conduction band minimum (CBM) from the valance band maximum (VBM) by about 5.5 eV. Depending on the surface termi-

nation and the purity of diamond, the Fermi level is located about 5 eV below the vacuum level [WSA97] and thus, electron tunnelling from the solids valence band into the affinity level of an atomic particle would require a significant reduction of the approaching particle's affinity level. The theoretical concept for negative ion formation at metals, including the hydrogen particles level shift is based on the assumption of 'free' charge carriers being present up to the Fermi level in the conduction band - an assumption that does not hold for diamond.
However, diamond is known to have a low electron affinity that can be positive or even negative (see schematic energy level diagram in figure 4.4). In case of positive electron affinity (PEA) the CBM is situated energetically below and in case of negative electron affinity (NEA) the CBM is energetically above the vacuum level [DKA+98]. While PEA is resulting for example when the diamonds surface is terminated with oxygen, NEA typically occurs in case of a hydrogen-termination [HKV+79, DKA+98, WZB+94]. It is quoted by [GD99] that especially NEA, resulting in the presence of an increased number of free electrons at the surface is beneficial for negative hydrogen ion formation.

Additionally to NEA, [APC+14] discusses a possible dependency of negative ion formation on the sp^3/sp^2 ratio, since they found increased relative negative ion yields for a changing ratio of sp^3 to sp^2 phases and see a possible correlation of this ratio and the field electron-emission properties reported by [KFK01, JEN+02] for nano-diamond/carbon composite films.
Although they pointed out that negative ion formation and field electron emission are two different mechanisms without having a direct correlation among each other, it is discussed that it may be also favourable for negative ion formation when electrons are easily released from the solid into vacuum. According to [KFK01, JEN+02] a negative electron affinity of diamond is not sufficient for high field electron-emission properties and among other conditions, also a good electron conduction is necessary. This is linked to the sp^2 content and their proper alignment, i.e. of the graphite phase of carbon that shows electrical conductivity [KFK01, HA98].
Another explanatory approach by [APC+14] is that negative hydrogen ion formation at diamond is linked to the hydrogen content in the sub surface layers. On the one hand this may be correlated with the increased probability of sputtering H as H^-, on the other hand the diamond's electronic structure may be beneficially modified, increasing the H^- formation probability like in case of tetrahedral

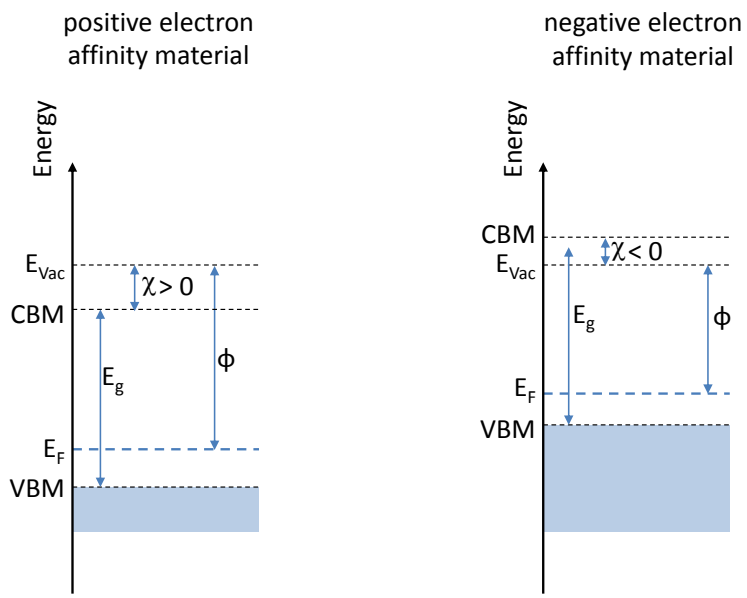

Figure 4.4: *Schematic energy diagram illustrating positive (left) and a negative electron affinity (right) after [DKA+98]. Labelled are the diamond's electron affinity χ, the work function ϕ, the band gap E_g, the valence band maximum (VBM), the conduction band minimum (CBM), the Fermi energy E_F and the vacuum energy E_{vac}.*

amorphous carbon, where increased negative ion yields in beam experiments have been found when the surfaces were hydrogen terminated which is according to [SWW+05] a result from a modification of the solid's energy levels.
For hydrogen terminated diamond films negative ion formation has also been observed due to electron stimulated desorption (ESD) by [GD99, GDF00, HLU+01] and according to [HLU+01] ESD is a consequence of one of the following two processes:

- In the dissociative electron attachment (DEA) process an electron impinges onto the solid, consisting of adsorbed H atoms on the diamond substrate. Thereby the electron is temporally captured and an excited, localized chemisorbed state results. This state can transform into a transient molecular negative ion state near the surface which subsequently can dissociate, resulting in the ejection of a negative ion and a remaining neutral or excited neutral surface state.

- In the dipolar dissociation process (DD), a hydrogen-carbon complex on the

surface is excited via electron impact collision. A subsequent fragmentation into a positive and a negative ion pair can occur where either the positive or the negative ion is ejected. The charge continuity is balanced by the surface acting as a source or a sink.

Independent of the underlying mechanism for negative hydrogen ion formation at a diamond surface, the net formation probability is expected to be increased compared to the metal case since the differences in the energetic structure should be correlated with an increased negative ion survival probability: Due to the diamond's band gap a decreased energy range is present where the affinity level of the formed negative hydrogen particle matches the states within the diamond which can be repopulated by the exchanged electron, i.e. which can lead to a neutralisation of the leaving particle [BE00].

Regarding the application of diamond materials in negative ion sources for future NNBI systems, the differing conditions between negative ion sources and experimental setups that have been used up to now for investigating negative ion formation on diamond materials have to be noted. A major difference is given for example in the overall particle fluxes: in contrast to the previously mentioned experimental setups, a high amount of charged particles, with comparably low energy is present in negative ion sources which are accompanied by a high flux of neutral atoms.
Only in the investigations on negative hydrogen ion formation performed by [KAP$^+$11, APC$^+$14] a combined flux of neutral and ionic hydrogen particles was present. However, for the experimental conditions within this low density discharge, a significantly lower atomic hydrogen flux is bombarding the investigated surfaces, deviating from a negative ion source plasma. Furthermore, the authors focused on the underlying mechanisms for negative ion formation and therefore they applied high bias potentials on the investigated surfaces. The resulting positive ion energies ($\sim 60\,\mathrm{eV}$) are significantly exceeding those in negative ion sources. Furthermore, the authors focused only on the relative increment of the negative ion yields comparing different carbon based materials and no absolute yields or a comparison with pure metal or caesiated metal surfaces was investigated by [KAP$^+$11, APC$^+$14]. Hence, an extrapolation of gained results to negative ion sources is very limited.

4.1.3 Volume Destruction

Negative hydrogen ions are easily destroyed due to the low binding energy of the second electron ($E_A = 0.75\,\mathrm{eV}$). As described in section 3.4, negative ions within the plasma volume are confined by the potential difference between the plasma and the surrounding wall. Hence, the drain of negative ions to the walls is reduced (depending on their energy and the amount of negative ions relative to the electron density) and the following processes within the plasma volume represent the main destruction channels:

- **Electron Detachment:** A collision of H^- with an electron creates a hydrogen atom and two electrons:

$$\text{ED:} \quad \mathrm{H}^- + e \rightarrow \mathrm{H} + e + e \quad . \tag{4.8}$$

- **Mutual neutralisation:** The collisional process between negative and a positive ion ($\mathrm{H}^+, \mathrm{H}_2^+, \mathrm{H}_3^+$) results in two neutral particles:

$$\text{MN:} \quad \mathrm{H}^- + \mathrm{H}_\mathrm{x}^+ \rightarrow \mathrm{H} + \mathrm{H}_\mathrm{x} \quad (\mathrm{x} = 1, 2, 3) \quad . \tag{4.9}$$

- **(Non-)associative detachment:** A negative ion colliding with a hydrogen atom leads to the formation of an electron and a hydrogen molecule or two H atoms:

$$\text{non-AD:} \quad \mathrm{H}^- + \mathrm{H} \rightarrow \mathrm{H} + \mathrm{H} + e \quad \text{, and} \tag{4.10}$$

$$\text{AD:} \quad \mathrm{H}^- + \mathrm{H} \rightarrow \mathrm{H}_2(\nu'') + e \quad . \tag{4.11}$$

- **Collisional Detachment:** A collision between a hydrogen molecule and a negative ion may lead to a hydrogen atom, a molecule and an electron:

$$\text{CD:} \quad \mathrm{H}^- + \mathrm{H}_2 \rightarrow \mathrm{H} + \mathrm{H}_2 + e \quad . \tag{4.12}$$

The rate coefficients for these processes are shown in figure 4.5. They have been calculated on basis of cross section data provided by [JRS03]. For electron detachment the rate coefficient has been calculated after equation (3.18) neglecting the negative ion motion. For the other processes, the rate coefficient were calculated after [SS74] taking the finite temperatures of both involved particles into account: For neutrals and positive ions a fixed temperature of 500 K for the solid lines in

figure 4.5. For particles of comparable masses, i.e. protons, atomic hydrogen and negative ions additionally rate coefficients are shown for $T_{\mathrm{H}} = T_{\mathrm{H}^+} = T_{\mathrm{H}^-}$ as dotted lines. In case of the associative and non-associative detachment the same collisional partners are involved. Thus, the sum of both rate coefficients is plotted in figure 4.5.

The rate coefficient for electron detachment shows a strong dependency on the electron temperature. For $T_{\mathrm{e}} = 0.5\,\mathrm{eV}$ X_{ED} is 1.1 $\times 10^{-15}\,\mathrm{m}^3/\mathrm{s}$ and for $T_{\mathrm{e}} = 10\,\mathrm{eV}$ it is $6.7 \times 10^{-13}\,\mathrm{m}^3/\mathrm{s}$. For H^- destruction via collisional detachment a high sensitivity of the rate coefficient on the negative ion temperature is present: between $T_{\mathrm{H}^-} \approx 0.3$ to $10\,\mathrm{eV}$ it increases by more than two orders of magnitude. For (non-)associative detachment and mutual neutralisation a comparatively small dependence on the H^- temperature is present (maximal a factor of 6.5 for T_{H^-} between 0.5 to $10\,\mathrm{eV}$).

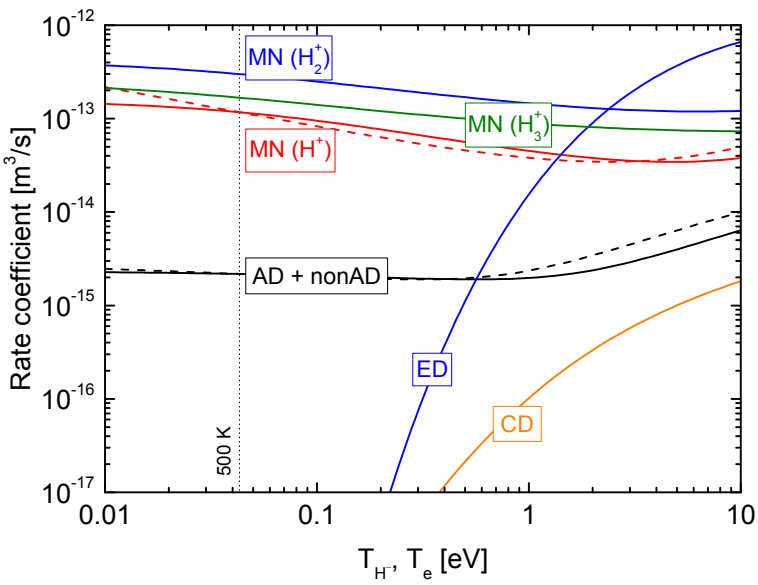

Figure 4.5: *Rate coefficients for negative ion destruction processes calculated on basis of cross sections after [JRS03] for fixed temperatures of neutrals and positive ions of 500 K (solid lines), and for $T_{\mathrm{H}} = T_{\mathrm{H}^+} = T_{\mathrm{H}^-}$ (dotted lines).*

According to equation (3.17) the destruction rate for each process is given by:

$$R_{\mathrm{d}} = n_{\mathrm{H}^-} n_{\mathrm{d}} X_{\mathrm{d}} \quad . \tag{4.13}$$

Here, the index d denotes the different destruction processes where n_{d} is the density of the corresponding collisional partner for H^- and X_{d} is the rate coefficient.

After equation (4.13) the negative ion destruction can be minimized by reducing the collisional partner's density n_d or by a beneficial particle temperature (see figure 4.5). However, this approach is only possible in a narrow range since it depends on the one hand on the relevancy of the distinct destruction channels and the controllability of the corresponding parameters and on the other hand on the dominant negative ion formation process, i.e. negative ion volume or surface production:
A reduction of the electron detachment is possible for example, by reducing n_e and/or T_e. However, especially when dissociative attachment represents the dominant formation channel, a reduction of n_e linearly reduces the formation rate and a lowered T_e hampers the production of required vibrationally highly excited molecules. For analogue reasons, a reduction of the molecular hydrogen density is limited.
Another possibility of decreasing the negative ion destruction rate would be given by reducing the positive ion density, i.e. by a reduction of the mutual neutralisation rate. Generally beneficial, this is limited as well since the positive ion density is coupled via quasi-neutrality with the density of negatively charged particles. Moreover, especially in ion sources based on the direct negative ion surface formation process, a high flux of positive ions ($\sim n_{\mathrm{i}+}$) onto the converter surface is required for a high negative ion yield. For the very same reason, a reduction of the (non-)associative detachment by reducing the atomic hydrogen density is limited.

4.2 Tandem Principle

Since contrasting plasma parameters for efficient negative ion formation on the one hand and minimized H^- destruction on the other hand are required, negative ion sources are designed after the so-called *tandem principle* which was introduced in volume negative ion sources first. The plasma volume is separated into distinct regions with tailored plasma conditions i.e. into a heated *driver* region with high electron temperatures and densities and in a diffusive downstream region located in front of the negative ion extraction system, with comparatively low T_e and n_e. In the heated driver region vibrationally highly excited H_2 molecules and atomic hydrogen particles are formed. Both particle species are characterised by long mean free paths[4] and therefore can diffuse into the downstream region. In this

[4]For the vibrationally excited molecules the long mean free path is caused by quantum mechanical selection rules which permit for the homo-nuclear molecules like H_2 and D_2 a depopulation of vibrational states by spontaneous emission (metastable character). The reformation

region, the dissociative attachment is promoted since the rate coefficients are generally increased at low electron temperatures (see figure 4.1). In case of negative ion surface formation, the flux of atomic hydrogen which comes from the driver impinges onto the converter surface and subsequently produces negative ions which can be extracted.
The low electron temperature and electron density is beneficial since linked to a reduced destruction via electron detachment. Furthermore and of special relevancy for negative ion sources is the lowered electron density in front of the extraction region, since a lowered co-extraction of electrons is given.

The separation of the plasma volume can be realized either by a magnetic filter field [LEB83] or a so-called meshed grid [FI92]. At the ion source for ITER NNBI a magnetic filter is going to be applied [IAE02]. Also at the IPP prototype sources a magnetic filter is used. The magnetic field lines are oriented parallel to the extraction grid system, forcing the electrons to gyrate. Thereby, the effective pathway of electrons is increased which results in an increment of the number of inelastic collisions between electrons and heavy particles and thus a reduction of the electron ensemble's energy, i.e. a reduction of the electron temperature. One major drawback of this technique is the resulting complex trajectory of all charged particles which is discussed to result in an unwanted plasma asymmetry in front of the plasma grid [FFKN09].
In the present work, the meshed grid method is used by mounting a stainless steel grid directly within the plasma volume. This is advantageous as a complex interplay among different magnetic field components are cancelled out. Originally, the meshed grid was introduced by [FI92] in their experimental setup for influencing the flux of electrons from the heated driver region into the none heated diffusive region by biasing the meshed grid. For wave heated plasma discharges, like in the present case, the meshed grid has another benefit (even without applying any bias). An efficient reduction of the electron temperature is given by limiting the electromagnetic wave propagation, i.e. the corresponding volume for power deposition. Electrons diffusing through the meshes are no longer heated and lose their energy by inelastic collisions with heavy particles, thus the electron temperature is diminished.

of atomic hydrogen to H_2 in the bulk plasma has a generally low probability caused by the low particle density typically present in low pressure discharges.

5 Applied Diagnostics

The effect of different materials on the negative ion density is investigated within this work in the downstream of a meshed grid of a ECR discharge. In this volume, plasma parameters, including the negative ion density are measured via optical emission spectroscopy (OES), Langmuir probe and laser photodetachment. OES is used for deriving the temperatures of neutral hydrogen particles (molecules and atoms) and the atomic to molecular hydrogen density ratio. The electron temperature, more precisely the EEDF as well as the positive ion density and the plasma and floating potential are determined via Langmuir probe measurements. In combination of Langmuir probe and laser photodetachment, the negative ion density is accessed.

5.1 Optical Emission Spectroscopy (OES)

Optical emission spectroscopy is a non-invasive diagnostic that allows for the determination of line-of-sight averaged plasma parameters. It is based on the measurement of the spectral intensity distribution $I(\lambda)$ that is related to the emissivity ϵ_{ik} via

$$\epsilon_{ik} = \frac{1}{l_{\text{plasma}}} \int_{\Delta\lambda_{ik}} I(\lambda) f(\lambda) \mathrm{d}\lambda \quad , \tag{5.1}$$

where l_{plasma} is the length of the line-of-sight within the plasma and $f(\lambda)$ a factor that takes the wavelength specific transmission of the applied spectroscopic system into account. Within the present work OES was used to determine the rotational and vibrational temperatures of the hydrogen molecule, the atomic hydrogen temperature and the density ratio of atomic to molecular hydrogen. From the latter the atomic hydrogen density can be derived by using the gas temperature, needed for determining the thermal atomic hydrogen flux onto investigated sample surfaces.

5.1.1 OES at Molecular Hydrogen

The rotational and vibrational temperatures of the electronic ground state of $H_2(X^1\Sigma_g^+)$ are evaluated by investigating the emission of the Fulcher system $(\mathrm{d}^3\Pi_\mathrm{u}, \nu', \mathrm{J}' \rightarrow \mathrm{a}^3\Sigma_\mathrm{g}^+, \nu'', \mathrm{J}'')$[1] after [FH98]. The ro-vibrational population distribution of the electronic ground state is thereby linked to the upper triplet state of the Fulcher system via electron impact excitation, assuming the validity of the *Franck-Condon principle*. The cross section data for these processes were taken from [MTG72]. The emission spectra of the Fulcher system range from 590 to 640 nm and for the diagnostic purpose the corresponding first five rotational Q-lines ($\mathrm{J}' = 1, ..., 5 \rightarrow \mathrm{J}'' = \mathrm{J}'$) of the first four diagonal vibrational bands ($\nu' = 0, ..., 3 \rightarrow \nu'' = \nu'$) were taken.

Determination of the gas temperature

The small energy difference of the rotational levels of the electronic ground state $n_{\mathrm{X}(\nu,\mathrm{J})}$ allows for a thermal population distribution by heavy particle collisions. Assuming the conservation of the rotational population distribution for electron impact excitation, the electronic ground state distribution is projected into the excited upper Fulcher state taking the ratio of the corresponding rotational constants $B^X_{\nu=0}$ and $B^d_{\nu'}$ into account [OOR+89]. This provides the diagnostic access for measuring the gas temperature. The corresponding emissivity of the ro-vibronic transitions is given by [Her50]

$$\epsilon_{\mathrm{d,a}}^{\nu',\nu''J',J''} \propto g_{\mathrm{core}} S_{J',J''} \exp\left(-\frac{\Delta E_{\mathrm{rot}}}{k_\mathrm{B} T_{\mathrm{rot}}^{\nu'}}\right) \quad , \tag{5.2}$$

where g_{core} is a statistical factor that is correlated with the nuclear spin and $S_{J',J''}$ the Hönl-London factor [Kov69]. ΔE_{rot} is the energy difference of the rotational levels of the corresponding upper states relative to $J' = 1$ and $T_{\mathrm{rot}}^{\nu'}$ the specific rotational temperature describing the thermal population distribution of a single vibrational state ν'. The latter can be deduced via the slope of the natural logarithm of $\epsilon_{\mathrm{d,a}}^{\nu',\nu''J',J''}/g_{\mathrm{core}} S_{J',J''}$ plotted versus ΔE_{rot}.
The rotational temperature in the electronic ground state can be obtained via [OOR+89]:

$$T_{\mathrm{rot}}^{\nu=0}(X) = \frac{B^X_{\nu=0}}{B^d_{\nu'}} T_{\mathrm{rot}}^{\nu'}(d) \quad . \tag{5.3}$$

[1] Within this work, the tick marks ' and " are used to differentiate between differently excited rotational and vibrational states.

It has to be noted that the rotational population in case of light molecules like hydrogen and deuterium can be varied in the electron impact excitation process and so different rotational temperatures can be given for different vibrational levels [OOR+89]. It has been reported by [FM01] that the rotational temperature derived from the $\nu' = 2$ state of the upper Fulcher level equals the gas temperature in a non-equilibrium hydrogen plasma after equation (5.2). For deuterium the gas temperature is derived from the rotational temperature of the $\nu' = 1$ state of the upper Fulcher level [Heg02].

Determination of the vibrational temperature

The determination of T_{vib}, describing a thermal population in the H_2 electronic ground state, via OES is performed by comparison of a measured relative vibrational distribution $n(\nu')/n(\nu' = 0)$ of the upper Fulcher level using the first four diagonal vibrational transitions, with a calculated one for a given vibrational temperature in ground state. Therefore, the measured vibrational distribution is deduced via the corresponding transition probabilities and the emissivities of each vibrational transition using equation (5.2) i.e. accounting for a Boltzmann population of the rotational states with the afore described rotational temperatures. This relative population distribution is compared to one, which is calculated for a distinct T_{vib} in ground state and projected into the upper Fulcher state, depending on the electron temperature, the corresponding Franck-Condon factors and vibrationally resolved relative rate coefficients [FH98].
It has to be noted that the evolution of the Franck-Condon factors for different vibrational states causes that this procedure gives access to the vibrational population distribution in electronic ground state of $\nu \leq 3$ in case of H_2 and $\nu \leq 4$ in case of D_2 only [FH98]. Thus, the vibrational temperature deduced via OES represents the low energy part of the vibrational population of H_2.

Determination of the entire Fulcher emission

For deriving the entire absolute emission of the Fulcher transition the measured emission of the first four diagonal transitions is extrapolated using a scaling factor $f(T_{\mathrm{vib}})$:

$$\epsilon_{\mathrm{Ful}} = f(T_{\mathrm{vib}}) \sum_{\nu'=0-3, J'=1-5} \epsilon_{\mathrm{d,a}}^{\nu' J'} \quad . \tag{5.4}$$

The scaling factor is taken from the ratio of a calculated emissivity of the first four vibrational bands to the calculated emissivity of the entire Fulcher transition.

Therefore, the population of the upper Fulcher level is calculated by balancing a population via electron impact excitation from electronic ground state, taking the Franck-Condon factors and vibrationally resolved, relative electron impact rate coefficients into account, against a depopulation via spontaneous emission (so-called *corona-model*) [FH98]. Since the vibrational population distribution in ground state is a function of the vibrational temperature, these scaling factors are functions of T_{vib}. Different scaling values[2] $f(T_{\mathrm{vib}})$ for H_2 and D_2, calculated for different vibrational temperatures by [Die10] can be found in table 5.1.

Table 5.1: *Scaling factors for extrapolation to the entire Fulcher emission after equation (5.4) calculated by [Die10].*

T_{vib} [K]	H_2	D_2
0	1.97	3.47
1000	1.97	3.44
2000	1.95	3.22
3000	1.92	2.97
4000	1.89	2.79
5000	1.87	2.67
6000	1.86	2.60
7000	1.86	2.59
8000	1.88	2.61
9000	1.92	2.67

5.1.2 OES at Atomic Hydrogen

Within the present work OES at atomic hydrogen is used for determining the atomic hydrogen temperature and the atomic hydrogen density. Particularly, the Balmer line emission $\epsilon_{\mathrm{H}(n'\rightarrow n''=2)}$ in a range between 410.2 to 656.3 nm, i.e. $H_\alpha, H_\beta, H_\gamma, H_\delta$ is used.

Determination of the atomic hydrogen temperature

For particles with distinct masses, e.g. for hydrogen molecules and atoms different temperatures can arise within a plasma. The temperature of atomic hydrogen can be derived via the Doppler broadening of the emission line profile. For an emitting

[2]The higher number of vibrational sates in D_2 causes that the measured emissivity represents a smaller fraction of the overall Fulcher emission compared to the case for H_2. Thus, higher scaling factors are required for extrapolating the measured to the entire Fulcher emission in case of deuterium.

particle of temperature T_{H^*} the Doppler effect leads to a Gaussian emission line profile whose full width at half maximum (FWHM) is given by

$$\Delta\lambda_{\mathrm{D}}(T_{\mathrm{H}^*}) = 2\lambda_0\sqrt{\frac{2k_{\mathrm{B}}T_{\mathrm{H}^*}\ln 2}{m_{\mathrm{H}}\mathrm{c}^2}} \quad . \tag{5.5}$$

Here λ_0 is the central wavelength of the emission line, m_{H} the mass of atomic hydrogen and c the speed of light. Taking fine structure splitting of the Balmer line as well as the apparatus profile of the optical system into account, the temperature of the excited atoms is accessible when other broadening mechanisms[3] can be neglected. Therefore, forward calculation can be used, i.e. the FWHM determined from measurement is compared to calculated ones where the temperature is used as input parameter. For the calculation each fine structure emission line has to be first convoluted individually, taking the Lorentzian line profile (coming from the natural broadening) and the Gaussian line profile (coming from the apparatus and the Doppler broadening which is characterised by the FWHM $\Delta\lambda' = \sqrt{\Delta\lambda_D^2(T_{\mathrm{H}^*}) + \Delta\lambda_{\mathrm{app}}^2}$ where $\Delta\lambda_{\mathrm{app}}$ is the FWHM of the apparatus profile) into account. On this bases the total emission line profile can be deduced when all fine structure lines are taken into account.

A main population mechanism of the upper atomic states is given by electron impact excitation of ground state atoms [WDF09]. During this collisional excitation process the kinetic energy of H(n = 1) is conserved due to the mass difference between atoms and electrons. Consequently, the temperature determined from the emission of excited particles equals the temperature of a thermalised ensemble in ground state:

$$T_{\mathrm{H}^*} = T_{\mathrm{H}} \quad . \tag{5.6}$$

Additionally, atoms can be directly formed via dissociative processes of hydrogen molecules or ionic molecules (see e.g. [JRS03]) and thus the population of excited atoms can be additional to the ground state atom, coupled to further species. This can, for example, be the case for recombining plasmas where the relevance of the population of excited hydrogen atoms via dissociative recombination (see equation (3.14)) can be significantly increased [WFF13]. Thereby high energetic H(n $\geq$ 2) can be formed [PTB+85].
The resulting emission due to optical de-excitation of such high energetic excited particles can lead to a well distinguishable Doppler broadened line profile when

[3]For a compilation of different broadening mechanisms see for instance [Gri74].

time scales for thermalisation among excited atoms are longer than spontaneous emission lifetimes. For such a case, the resulting emission line profile is shown in figure 5.1. By comparing the transition probability A_{ik} and the time scales for formation of and thermalization among the resulting ensembles, it has to be revised, whether and which of the determined temperatures represents the temperature of ground state atoms.

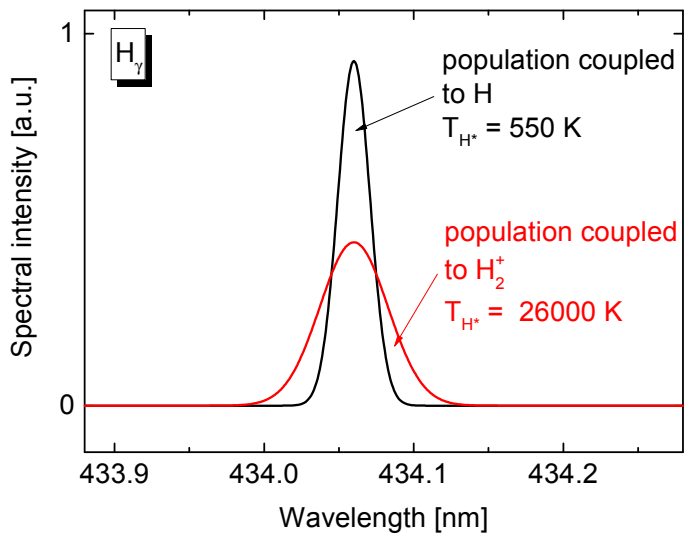

Figure 5.1: *Emission line profile of H_γ resulting from optical de-excitation of H(n=5) formed via processes coupled to the electronic ground state and from dissociative recombination, i.e. coupled to the positive hydrogen molecule ion H_2^+.*

Influence of different population channels on the Balmer emission

The influence on the Balmer emission due to population processes coupled to different species like the electron impact excitation from the atomic ground state, dissociative excitation ($H_2 + e_f \rightarrow H + H(n \geq 2) + e_s$) or the dissociative recombination (see equation (3.14)) can be assessed via *Yacora H* [Wün04]. In figure 5.2 the influence of the population coupled to the corresponding species on the H_γ emission is shown, as a function of the atomic to molecular hydrogen density ratio n_H/n_{H_2} as well as of the density ratio of molecular H_2^+ ions relative to the electron density $n_{H_2^+}/n_e$. Depicted data were calculated for 1 Pa total pressure and a gas temperature of 550 K. The electron temperature is set to 2 eV and $n_e = 1 \times 10^{16}\,\mathrm{m}^{-3}$.

As can be seen, with increasing n_H/n_{H_2}, the emission is less influenced by pro-

cesses coupled to molecular hydrogen. Only for $n_{\mathrm{H}}/n_{\mathrm{H_2}}$ lower than 1 %, the H_γ emission is significantly determined by H and $\mathrm{H_2}$. In this case, the emissivity is influenced by more than 20 % compared to H(n = 5) being populated solely via processes coupled to the atomic ground state. For higher atomic to molecular density ratios than 1 % this influence continuously diminishes.
In contrast, at chosen parameters, the influence on the emission due to a population coupled to $\mathrm{H_2^+}$ shows a strong increase with increasing $n_{\mathrm{H_2^+}}$. While at $n_{\mathrm{H_2^+}}/n_{\mathrm{e}} = 1\,\%$ the emission is influenced by less than 5 % compared to a population of H(n = 5) coupled only to the atomic ground state, it is influenced by more than 30 % for $n_{\mathrm{H_2^+}}/n_{\mathrm{e}} > 10\,\%$.

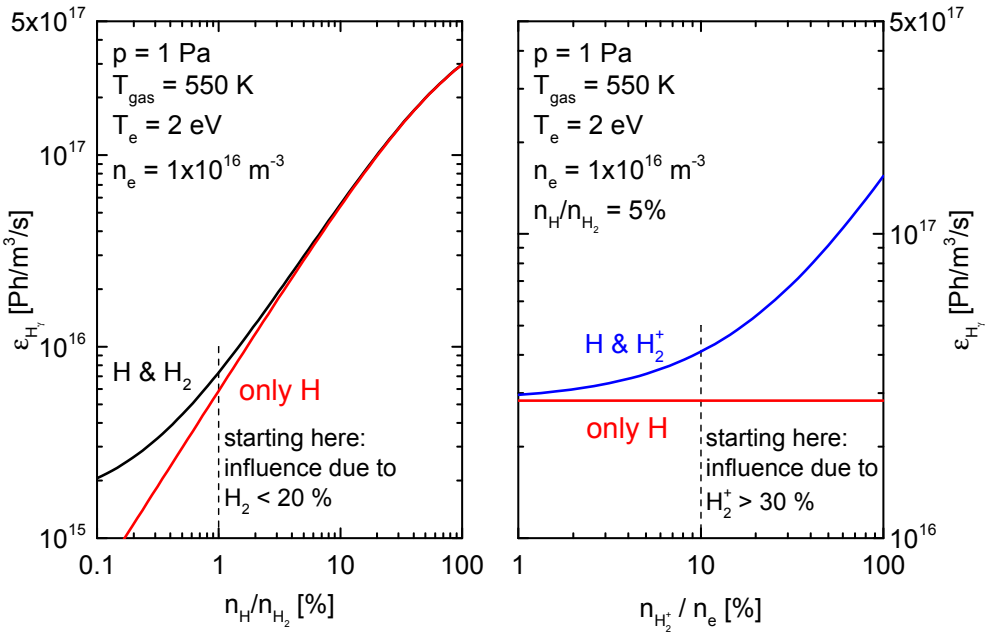

Figure 5.2: *Influence of the population via processes coupled to the neutral hydrogen atom, the hydrogen molecule and the molecular hydrogen ion* $\mathrm{H_2^+}$ *on the* H_γ *emission determined via Yacora H [Wün04].*

Determination of the atomic hydrogen density

The atomic hydrogen density can be derived via the atomic to molecular hydrogen density ratio. This ratio is determined by the emission ratio of atomic to molecular hydrogen taking *effective emission rate coefficients* X^{eff} into account. Such X^{eff} are given by the product of the corresponding Einstein-coefficient for spontaneous emission and the so-called *collisional-radiative coupling coefficients*

which describe the population processes coupled to the respective ground or ionic states [Fan06]. The calculation of collisional-radiative coupling coefficients can be performed via CR models. Under the assumption of dominant population of H(n = 5) and $H_2(d^3\Pi_u)$ via processes coupled to the neutral atom H and the molecule H_2 the emissivity is given by [Fan04]:

$$\epsilon_{H_\gamma} = n_e n_H X^{eff}_{H_\gamma} \quad \text{and} \tag{5.7}$$

$$\epsilon_{Ful} = n_e n_{H_2(X)} X^{eff}_{Ful} \quad . \tag{5.8}$$

Hence, the atomic to molecular density ratio is:

$$\frac{n_H}{n_{H_2}} = \frac{\epsilon_{H_\gamma}}{\epsilon_{Ful}} \left(\frac{X^{eff}_{H_\gamma}}{X^{eff}_{Ful}} \right)^{-1} \quad . \tag{5.9}$$

For known total pressure and temperatures of neutrals[4] the atomic hydrogen density is

$$n_H = \frac{p}{k_B T_{gas} (n_H/n_{H_2})^{-1} + k_B T_H} \quad . \tag{5.10}$$

The ratio of the effective rate coefficients calculated via the corresponding CR models *Yacora H* [Wün04] and H_2 [WDF09] for equation (5.9) is shown in figure 5.3. As can be seen, for electron densities between $1 \times 10^{16}\,m^{-3}$ and $1 \times 10^{17}\,m^{-3}$, relevant within the present work, the ratio is insensitive for a wide electron temperature range and is between 0.6 and 0.7.

It has to be noted, this evaluation is valid only for a dominant population of the relevant excited states coupled to the corresponding ground states. When additional species are relevant for the population of H(n = 5) or $H_2(d^3\Pi_u)$ equation (5.9) has to be modified. However, if the products of these additional population channels are spectroscopically identifiable, as shown for example in figure 5.1, a separate treatment of each ensemble is possible.

5.2 Langmuir Probe

A widely used diagnostic in plasma physics is the so-called Langmuir probe (after I. Langmuir [MSL26]). It is an electrostatic probe that allows for the determination of multiple local plasma parameters by drawing a current due to an applied

[4] It has to be noted, in the low temperature low pressure hydrogen plasmas investigated within this work, molecular hydrogen represents the dominant particle species. Thus, the corresponding temperature T_{H_2} represents the gas temperature.

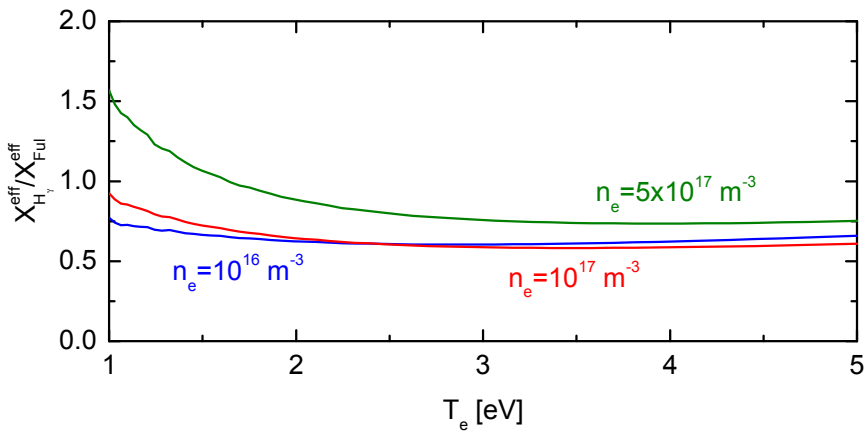

Figure 5.3: *Ratio of the effective emission rate coefficients for the* H_γ *and Fulcher emission versus the electron temperature for different electron densities, calculated via the CR models Yacora H and* H_2 *for dominant coupling to the corresponding ground states.*

variable voltage U between a probe tip and the conducting walls. In order to minimize the influence of this invasive diagnostic, typically small cylindrical probes (radius of $r_p = 50\,\mu$m and some mm length) are used drawing currents in the range of a few mA at applied biases of some ten volts. The basic concept is that depending on the applied probe voltage an energetic filter for charged particles is given that determines the corresponding electron and ion fluxes onto the probe tip. The collecting area of charged particles is given by the probe tip surrounding sheath whose radius r_s can be approximated for cylindrical probes after [Kie68] by

$$r_\mathrm{s} = \left(1 + \gamma^{-0.375}\tau(\alpha)\frac{1+Q}{1+\alpha}\left|\phi_\mathrm{pl} - U\right|\right) r_\mathrm{p} \quad . \tag{5.11}$$

Here ϕ_pl is the plasma potential and α and Q represent the temperature and charge ratios of attracted to repulsed particles respectively. The parameter γ is a function of these ratios, the probe radius and the Debye length: $\gamma = (r_\mathrm{p}/\lambda_\mathrm{D})^2(1+\alpha/Q)^{-1}$. For $\alpha \geq 1$, $\tau(\alpha)$ is $\tau(\alpha) = 1 + 0.23\alpha^{-0.68}$ and $\tau(\alpha) = 1.54 - 0.3542\alpha^{0.35}$ when $\alpha < 1$.

For an electropositive plasma, the measured current $I(U)$ is a superposition of the positive ion current $I_\mathrm{ion}(U)$ and the electron current $I_\mathrm{e}(U)$. While electrons reaching the probe are measured by definition as a positive current, positive ions recombine at the probe tip with electrons from the probe tip and the resulting

positive ion current is measured as a negative current:

$$I(U) = I_{\mathrm{e}}(U) - I_{\mathrm{ion}}(U) \quad . \tag{5.12}$$

5.2.1 Probe Characteristic

In the following, basic concepts for understanding the measured probe characteristic will be discussed. More detailed information about the physics of Langmuir probes can be found in literature e.g. [LL05], [CB11] and [Che03].

A typical current-voltage characteristic for an electropositive plasma is depicted in figure 5.4 where different regimes can be identified:

Applying a sufficiently high negative voltage ($\mathrm{e}U \gg k_{\mathrm{B}}T_{\mathrm{e}}$), a sheath is formed that is repulsive for electrons and attractive for positive ions. In this **ion saturation region** a negative current is measured that is mainly driven by positive ions. Although the name indicates a saturation, for cylindrical probes no real saturation can be measured, caused by the increase of the collecting sheath radius for increasing bias (see equation (5.11)).
Increasing the voltage from highly negative values to less negative values reduces the electron repelling potential. Hence more and more electrons reach the probe tip depending on their energy. The measured negative current $I(U)$ decreases. At a probe bias that equals the local **floating potential** ϕ_{fl}, the positive ion flux equals the electron flux and no net current is measured. Further increasing the probe bias decreases the electron repelling sheath size. In case of a Maxwellian EEDF, the electron current I_{e} rises exponentially in this **transition region**.
Reaching the local **plasma potential** ϕ_{pl}, the presence of the probe is not disturbing the plasma, and no sheath is surrounding the probe tip. Due to the temperature difference ($T_{\mathrm{e}} \gg T_{\mathrm{ion}}$) as well as due to the mass difference of electrons and positive ions, the electron flux is much higher than the positive ion flux. Hence the measured current is nearly solely given by the electron current:

$$I(U = \phi_{\mathrm{pl}}) \approx I_{\mathrm{e}}(U = \phi_{\mathrm{pl}}) \quad . \tag{5.13}$$

A further increment of probe bias leads to the formation of an electron attracting sheath and the ion current is more and more suppressed. In this so-called **electron saturation region** again no real saturation of the measured current is

obtained for cylindrical probe geometries due to the expanding collection radius.

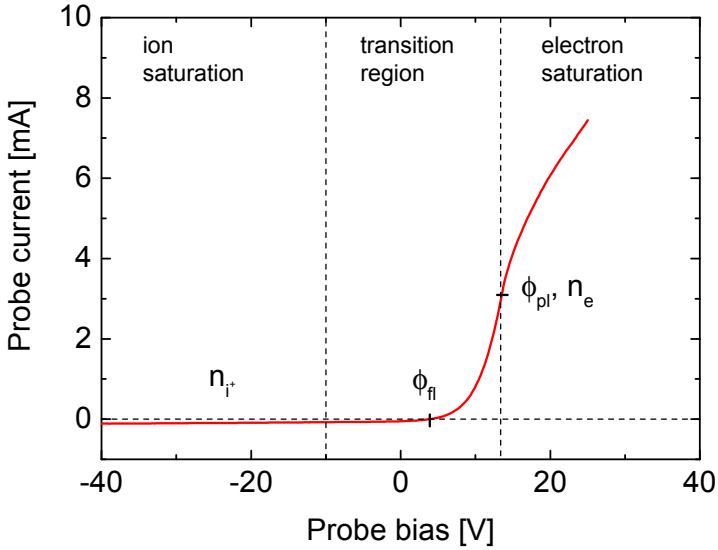

Figure 5.4: *Typical current-voltage characteristic for a cylindrical Langmuir probe in an electropositive plasma, including labels for the positive ion and electron density as well as floating and plasma potentials at corresponding sections for their determination.*

5.2.2 Determining Plasma Parameters

The I-U characteristics measured with a Langmuir probe provides access to various plasma parameters like the positive ion and electron densities, the EEDF and 'possibly' the electron temperature, as well as the local plasma and floating potentials. A Langmuir probe also can be used to measure the negative ion density. However, this is only possible for sufficiently high negative ion densities which will be addressed separately at the end of this section. In the following the main concepts for analysing probe characteristics will be briefly discussed. A detailed description can be found in literature, e.g. [Che03].

Potentials

As the **floating potential** is given for flux equality, it can be directly determined via $I(\phi_{\mathrm{fl}}) = 0$.

The **plasma potential** marks the end of the transition region. In case of a Maxwellian EEDF the electron current for a probe bias lower than ϕ_{pl} is given by

$$I_{\mathrm{e}}(U) = A\mathrm{e}\Gamma_{\mathrm{e}} = Ae\frac{1}{4}n_{\mathrm{e}}\exp-\left(\frac{\mathrm{e}(\phi_{\mathrm{pl}}-U)}{k_{\mathrm{B}}T_{\mathrm{e}}}\right)\langle v_{\mathrm{e}}\rangle \quad , \quad U \leq \phi_{\mathrm{pl}} \quad , \tag{5.14}$$

where A is the effective collection area of the probe, taking the probe tip dimensions and the surrounding sheath dimensions into account (see equation (5.11)) and $\langle v_{\mathrm{e}}\rangle$ the mean thermal electron velocity. Due to the exponential increase of equation (5.14) the slope of the measured current is maximal at $U = \phi_{\mathrm{pl}}$. Drawing a higher current in the electron saturation region by further increasing the probe bias is correlated with increasing the electron attracting sheath size. In this region, the electron current is no longer exponentially increasing with probe bias and as can be seen in figure 5.4, for $U > \phi_{\mathrm{pl}}$ a reduced slope of the measured current is given. This allows for deducing ϕ_{pl} via the determination of the maximal slope that is mathematically given by the inflection point:

$$\frac{d^2I(U)}{dU^2} = 0 \Leftrightarrow U = \phi_{\mathrm{pl}} \quad . \tag{5.15}$$

The determination of the plasma potential is illustrated in figure 5.5 on the left.

Electron Density

For known T_{e} the electron density can be derived after equation (5.14) from the measured current at the plasma potential where no sheath is present. Here the collecting area A can be approximated by the probe surface area, neglecting the top of the cylindrical probe tip, and the electron density is given by

$$n_{\mathrm{e}} = \sqrt{\frac{m_{\mathrm{e}}}{2\pi k_{\mathrm{B}}T_{\mathrm{e}}}}\frac{I(\phi_{\mathrm{pl}})}{\mathrm{e}r_{\mathrm{p}}l_{\mathrm{p}}} \tag{5.16}$$

where r_{p} and l_{p} are the corresponding probe radius and length.

EEDF and Electron Temperature

As the electron current in the transition region is depending on the electron energy $E_{\mathrm{e}} = \mathrm{e}(\phi_{\mathrm{pl}}-U)$, the Langmuir probe grants a direct access to the EEDF. However, it has to be noted that near the floating potential, the measured current is carried by electrons and positive ions. Thus, for deriving the EEDF from the measured

probe characteristic, the positive ion current first needs to be subtracted and the EEDF can be deduced from the resulting data. After [Dru30], the EEDF $f(E_\mathrm{e})$ is given via the second derivative of this probe current:

$$f(E_\mathrm{e}) = \frac{\sqrt{8m_\mathrm{e}E_\mathrm{e}}}{\mathrm{e}^{3/2}A}\frac{d^2I}{dU^2} \quad . \tag{5.17}$$

In figure 5.5 on the left the second derivative of a measured probe current is plotted, including a denotation of the range for determining the corresponding EEDF. The EEDF transformed into the EEPF $g(E_\mathrm{e})$ is depicted in a logarithmic scale on the right. As mentioned in chapter 3.1, plotted in this scale, a Maxwellian EEPF linear decreases. Thus, for electrons being thermalized, the electron temperature can be derived by the inverse of the slope of the measured EEPF. One can see in figure 5.5 that the measured EEPF significantly deviates in the low energy region from a linear evolution. This is an inherent characteristic for gaining the EEPF via a Langmuir probe, independent of a present thermalization of electrons. Among others, this is a consequence of the numerical procedure for deriving the EEDF. However, the deviation can also arise due to technical measurement reasons like rf-noise and stray capacitances, as well as due to oscillations of the plasma potential [GPA92].

Obviously, a deviation from the linear regression can also be the result of the EEDF being non-Maxwellian. For that case the above mentioned procedure still can be applied but only the determination of an effective temperature via the mean energy is possible (see equation (3.9)). However, it has to be noted that determining the mean energy by using equation (3.6), i.e. by integration of the measured EEDF, always leads to an inherent underestimation of $\langle E \rangle$ due to the afore mentioned underpopulation of the measured EEDF close to the plasma potential. Another approach for characterising the measured EEPF is possible by fitting a corresponding EEPF like a Bi-Maxwellian to the measured one.

The measurement of the EEDF by a Langmuir probe is always limited to the low energy region. This is a consequence of the rapid decay of the electron current in the transition region down to the floating potential leading to an unfavourable signal-to-noise ratio and the EEDF is overlaid by distortions at higher electron energies.

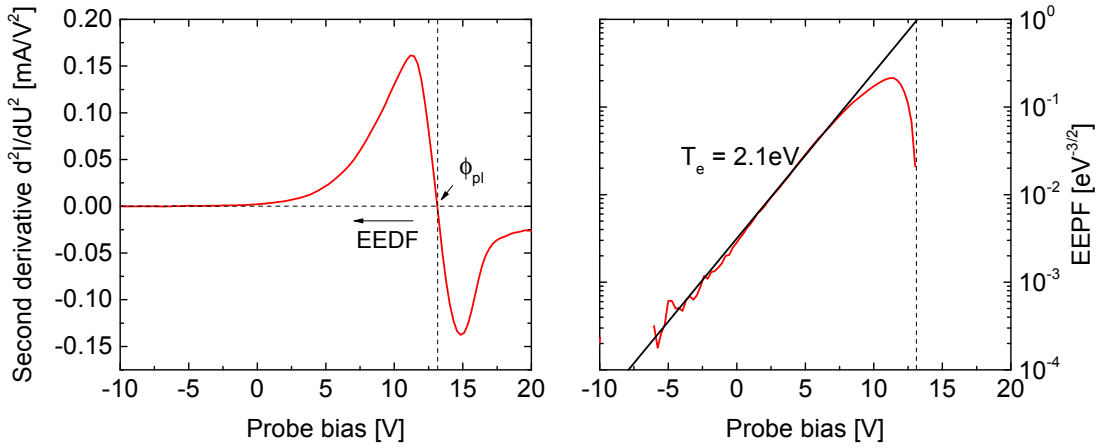

Figure 5.5: ***Left:*** *Second derivative of a measured Langmuir probe characteristic for determining the plasma potential as marked and the position of the EEDF.* ***Right:*** *Plot of the EEPF calculated from the second derivative of the measured probe current, including a linear fit for determining the effective electron temperature.*

Positive Ion Density

The positive ion density is derived from the positive ion current in the ion saturation region. However, the description of the dependence of I_{ion} on the probe bias requires a proper description of the sheath surrounding the probe including the collection of particles. In practice, the positive ion density is derived by fitting a theoretical evolution of the positive ion current to the measured one. For cylindrical probes three theoretical approaches are most commonly used to describe the ion saturation current: the Orbital Motion Limited (OML) theory, the theory developed by Allen, Boyd and Reynolds (ABR) as well as the one by Bernstein, Rabinowitz and Laframboise (BRL). All these theories have in common that they assume collisionless sheaths. They differ in the description of the sheath and the particle motion. There is no general rule at which circumstances a certain model is valid and the applicability of a model has to be assessed carefully e.g. by benchmarking the derived density against other diagnostics. A brief description of the different theories is given in the following. A review and a discussion of the applicability can be found for instance in [Che03].

- The **Orbital Motion Limited (OML) theory** ([MSL26]) is based on the assumption that the potential applied to the probe decays homogeneously from $\phi = U$ at the probe tip to $\phi = 0\,\text{V}$ at infinity. Within this infinite

sheath the ion current is only determined by the orbital motion of the particles and the particle trajectory can be calculated by angular momentum and energy conservation. After [Che09], the positive ion current I_{ion} onto a cylindrical probe is proportional to the positive ion density, the applied probe bias and depends on the positive ion mass:

$$I_{\text{ion}} \propto n_{\text{i}} \sqrt{\frac{U}{m_{\text{i}}}} \tag{5.18}$$

The applicability of the OML theory was shown for densities in the range of some $10^{14} - -10^{16}\,\text{m}^{-3}$ and probe tip radii of up to $60\,\mu$m, i.e. for comparable conditions like within the present work by [Che09].

- A model of the ion sheath for spherical geometries was presented by **Allen, Boyd and Reynolds (ABR)** ([ABR57]) and extended to cylinders by Chen [Che65]. In this theoretical description, the potential distribution within the sheath is calculated by solving the Poisson equation assuming cold ions at start ($T_{ion+} = 0$) that move radial onto the probe. An orbital motion is neglected and so the theoretical predictions typically overestimate the calculated positive ion current and in turn, the positive ion densities derived via the ABR theory tend to underestimate the actual positive ion density [CEZ12].

- **Bernstein and Rabinowitz** calculated the ion current taking the orbital motion within a finite sheath into account [BR59]. This approach was extended by **Laframboise** [Laf66] for a Maxwellian distribution describing the positive ion energy. Thus, from a theoretical point of view the most accurate description of the positive ion current is given by the **BRL** theory. Although this rather sophisticated model accounts for several physical processes, different authors reported that positive ion densities determined via BRL often overestimate the correct value (see for instance [Che09], [Che03]).

Only in case of the OML theory an analytical solution can be derived for determining the positive ion density. In contrast, for the ABR and BRL theory no analytical formulas describing the positive ion current can be derived and numerical computations are necessary. For these theories, a determination of the positive ion density is possible via an iterative procedure based on the parametrization after [Che01].

Within this work the applicability of these different theories has been investigated

by comparing the measured ion current evolution with a theoretical calculated current evolution. In case of hydrogen, the measured ion saturation current showed within the investigated parameter space a linear dependency of I^2 versus the probe bias. After [Che09], such a linear dependence indicates a perfect orbiting and the OML theory can be applied. In contrast, positive ion currents calculated via ABR and BRL theory do not show a linear dependence of I^2 on probe bias.
In case of deuterium, $I^2(U < \phi_{\mathrm{fl}})$ does not evolve as a straight line, which is caused by the higher mass of the corresponding positive ions that hinders their perfect orbiting at given potential differences between probe and plasma. Here the theoretical positive ion current predicted by the BRL theory shows the best accordance with the measurements.

All described ion theories are functions of the positive ion mass. For the investigated hydrogen plasmas three different species of positive ions H^+, H_2^+ and H_3^+ are contributing to the overall ion current. This can be taken into account by using an effective ion mass $m_{\mathrm{ion}}^{\mathrm{eff}}$ calculated on basis of the corresponding relative ion concentrations.
The relative positive ion concentration in low pressure low temperature hydrogen discharges is depending on various parameters and can be measured using ion mass spectrometry for example. However, within this work no diagnostic access to the relative positive ion concentrations is given and therefore, measurements of the positive ion concentrations performed by other groups at comparable experimental conditions were consulted.
Typically, for low pressure low temperature hydrogen discharges up to several Pascal pressure and low discharge powers (below 500 W), the positive ion concentration is dominated by H_3^+ followed by H_2^+ and H^+ [MGH+06, NK07, MFS+08]. With decreasing pressure [MGH+06] measured an increasing share of H_2^+, developing to be the dominant species at electron densities of several $10^{16}\,\mathrm{m}^{-3}$ and T_{e} in the range of 2 to 8 eV. Also within other low pressure low temperature hydrogen discharges, a comparable result was found [SCC+08, Ert10]. Thus, for the evaluation of the positive ion density within this work an effective positive ion mass of 2 u for hydrogen and 4 u for deuterium is assumed.

Influence of Negative Ions

In the presence of negative ions, the measured probe current in the transition and electron saturation region is modified depending on the ration of negative ions to electrons and the corresponding particle temperatures. When the probe is biased to the plasma potential, no sheath is present and the measured current is given by

$$I(U = \phi_{\mathrm{pl}}) = I_{\mathrm{e}} + I_{\mathrm{H^-}} \propto n_{\mathrm{e}}\sqrt{\frac{k_{\mathrm{B}}T_{\mathrm{e}}}{m_{\mathrm{e}}}} + n_{\mathrm{H^-}}\sqrt{\frac{k_{\mathrm{B}}T_{\mathrm{H^-}}}{m_{\mathrm{H^-}}}} \quad . \tag{5.19}$$

Caused by the high mass difference between ions and electrons, the flux of negative ions is by a factor of $\sqrt{m_{\mathrm{e}}/m_{\mathrm{H^-}}}$ lower compared to a pure electron driven flux, even for $T_{\mathrm{H^-}} \approx T_{\mathrm{e}}$ and $n_{\mathrm{H^-}}/n_{\mathrm{e}} = 1$. For those conditions, $I(U = \phi_{\mathrm{pl}})$ is minor effected by the presence of negative ions (about 2%). For lower negative ion temperatures, the influence of negative ions on the probe characteristic is even more decreased and can be neglected.
In case of high negative ion concentrations ($n_{\mathrm{H^-}}/n_{\mathrm{e}} \gg 43$ for $T_{\mathrm{H^-}} \approx T_{\mathrm{e}}$) an ion-ion plasma is formed and due to the comparable masses of positive and negative ions the probe characteristic is getting symmetric [WPL73].

Influence of a Magnetic Field

In the presence of a magnetic field the probe characteristic can be modified as a consequence of the magnetization of charged particles. Since diffusion perpendicular to B-field lines is hindered for charged particles, the effective collection area of a probe is modified [Che65]. In general, the magnitude of this effect is dependent on the orientation of the probe relative to the field lines and the mean free path of particles moving perpendicular to the magnetic field. Furthermore, a magnetic field differently affects the currents of electrons and ions onto a probe. After [PT01] the applicability of a Langmuir probe in the presence of a magnetic field is depending on the dimensionless parameter $\kappa = r_{\mathrm{p}}/r_{\mathrm{L}}$, i.e. the ratio of probe radius and the Larmor radius. When $\kappa \ll 1$, the magnetic field is negligible and an evaluation of the probe characteristic for the charged particle densities is possible [PT01]. For typical values in the present experimental setup ($T_{\mathrm{e}} = 1\,\mathrm{eV}$, $B = 87.5\,\mathrm{mT}$) the gyration radius of electrons ($r_{\mathrm{L}} \approx 44\,\mu\mathrm{m}$) is comparable to the probe radius ($r_p = 50\,\mu\mathrm{m}$) and $\kappa \approx 1$. In this case, a significantly reduced electron current is resulting compared to a field free situation and a direct measure of the electron density at the plasma potential after equation (5.16) is not possible. Due to the larger gyration radii of ions κ is$\ll 1$ and consequently,

the positive ion density can be determined from the measured positive ion saturation current as described above. It has to be noted that since the electron energy is not influenced by the an homogeneous, conservative B-field, no effect on the EEDF evaluation is given.

5.3 Laser Photodetachment

Laser photodetachment is a diagnostic to determine spatially resolved the negative ion density, based on the photodetachment process:

$$\mathrm{H}^- + \mathrm{h}f \rightarrow \mathrm{H} + e \quad . \tag{5.20}$$

A sketch of the principle setup for the laser photodetachment diagnostic is shown in figure 5.6. A laser is used to inject photons of suitable energy ($E_{\mathrm{Ph}} > E_{\mathrm{A}}$) into the plasma within a short laser pulse of some nanoseconds duration. Negative ions in the illuminated laser beam are destroyed, resulting in a localised increment of the electron density that is proportional to n_{H^-}. Via a Langmuir probe this increment is measured. Therefore, the probe tip is axially centred to the laser beam axis and positively biased at a constant voltage U in the electron saturation region ($U > \phi_{\mathrm{pl}}$) [BHB+79]. An ideal evolution of the laser photodetachment

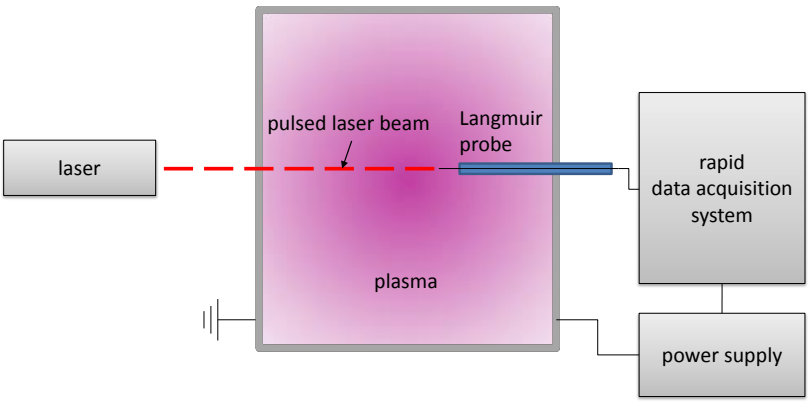

Figure 5.6: *Schematic of the laser photodetachment setup.*

signal is shown schematically in figure 5.7. The following description is based on the theoretical model after [SDB+90] and applies for an electropositive plasma. For simplification, the volume that is illuminated by the laser is labelled in the following as such even in the absence of the laser light in order to distinguish between the surrounding undisturbed plasma and the beam volume. It has to be noted that the injection of the laser does not alter the net charge within the laser beam volume but changes the net mobility of negatively charged particles.

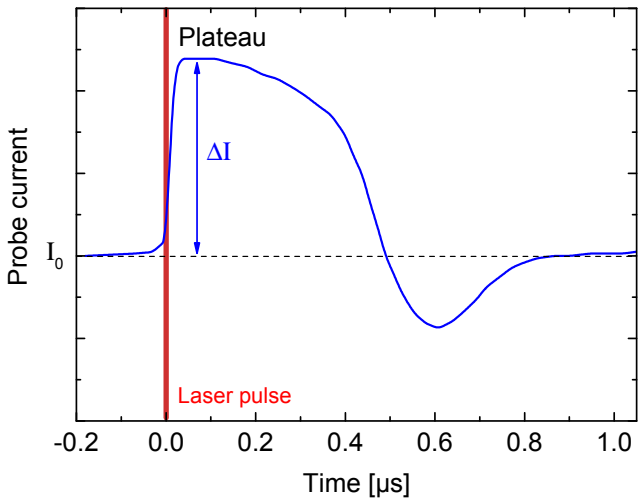

Figure 5.7: *Time evolution of a theoretical laser photodetachment signal after [SDB+90].*

For $t < 0$, just before the laser pulse, the fluxes of negatively charged particles entering and leaving the beam volume are balanced. A constant current I_0 is given that is due to the high mobility of electrons, proportional to the steady-state electron density n_e (see equation 5.14).
At $t = 0$ the short laser pulse is injected which duration is chosen to be short enough not to influence the following particle dynamics. Due to the negative ion destruction, the electron density in the beam volume is increased to $n'_e = n_e + n_{e\,\mathrm{from\,H^-}}$, leading to a sudden increase of the probe current by ΔI. The ratio of the electron current onto the probe before and shortly after the laser pulse is given by

$$\frac{I_0 + \Delta I}{I_0} = \frac{\frac{1}{4}A\left(n_e + n_{\mathrm{H^-}}\right)\langle v_e\rangle}{\frac{1}{4}An_e\langle v_e\rangle} = \frac{n_e + n_{\mathrm{H^-}}}{n_e} \quad . \tag{5.21}$$

Here, a constant mean thermal electron velocity $\langle v_e \rangle$ of steady-state electrons and those that are created by the photodetachment process can be assumed as the corresponding thermalization proceeds in sufficiently short time scales ($\sim 10\,\mathrm{ns}$) [Bac00]. Furthermore, a constant collection area of the probe A can be assumed within the present short time scales [BBB96]. Thus, the relative negative ion density, i.e. the ratio of the negative ion density to the steady-state electron density is

$$\frac{\Delta I}{I_0} = \frac{n_{\mathrm{H}^-}}{n_e} \quad . \tag{5.22}$$

The absolute negative ion density n_{H^-} can be subsequently derived by simple multiplication of the relative negative ion density with n_e that has to be determined at the same location by an independent measurement via the Langmuir probe.

The dynamic of the laser detachment system can be understood in terms of the changed mobility, taking the ambipolar diffusion of the different particle species within the beam volume and the surrounding volume into account. The injection of the laser pulse, i.e. the creation of electrons by the photodetachment process results in an increased flux of negatively charged particles leaving the beam volume. As the negative ions in this region have been destroyed, this leaving flux is a flux of highly mobile electrons. As this flux is increased compared to the overall flux of electrons and negative ions, this would lead to a depletion of negatively charged particles within the laser beam volume. In order to keep quasi-neutrality fulfilled, a potential barrier evolves, to diminish the electron drain. The resulting electron confinement leads to the occurrence of a so-called plateau in the laser detachment signal (see figure 5.7). The duration of the plateau (typically 100 to 200 ns) is a function of the laser beam diameter and the velocity of negative ions in the undisturbed, surrounding plasma as the flux of negative ions entering the beam volume continuously reduces the potential barrier. Thus, correlated with the diminishment of the potential, the electron confinement reduces and the probe current decays over time.
As can be seen in figure 5.7, at $0.5\,\mu\mathrm{s}$ an overshoot, i.e. an even lower current than the initial I_0 evolves. This is a consequence of the positive ion's inertia: Positive ions are repelled by the aforementioned electron confining potential and are accelerated out of the beam volume. The positive ions are characterised by a lower mobility compared to the net mobility of negatively charged particles and do not react within the same time scale on changes of the potential topology.

Thus, a depletion of positively charged particles in the laser beam volume arises. This in turn is balanced by a reduction of electrons in the beam volume and consequently the overshoot evolves. As the dynamics are damped over time the measured current typically tends to I_0.

Required laser beam diameter

The required size of the laser beam diameter is dependent on the region in which electrons that are created by the photodetachment process are collected by the Langmuir probe. Hence, it is dependent on the probe bias and according to [BBN81, Bac93], in combination with a cylindrical probe which radius is r_p, the laser beam radius r_c can be approximated to be at least:

$$r_\mathrm{c} \gtrsim r_\mathrm{p} + c \cdot r_\mathrm{s}(U) \quad , \tag{5.23}$$

where r_s represents the collection radius of a cylindrical probe given by equation (5.11) and c an empirically determined correction factor that ranges between two and three. For low temperature, low pressure hydrogen discharges with electron densities of some 10^{15} to $10^{16}\,\mathrm{m}^{-3}$ and an electron temperature of 1 eV, a beam radius of around 3 mm is required when a Langmuir probe of radius 50 μm is used biased to about 40 V.

Pulse energy and detachment efficiency

The cross section σ_PD for photodetachment at negative hydrogen ions is depicted after [Lab77] in figure 5.8. Nd:YAG lasers are capable to produce short high energetic laser pulses at a wavelength of 1064 nm ($E_\mathrm{Ph} = 1.17\,\mathrm{eV}$) where the cross section is $\sigma_\mathrm{PD} = 3.5 \times 10^{-21}\,\mathrm{m}^{-2}$, i.e. only slightly lower than the maximal value of $\sigma_\mathrm{PD} = 4 \times 10^{-21}\,\mathrm{m}^{-2}$ at 800 nm. Therefore, Nd:YAG lasers are frequently used for determining the negative hydrogen ion density via laser photodetachment at hydrogen discharges [Bac00].
After [BHB+79] the detachment efficiency $\Delta n_{\mathrm{H}^-}/n_{\mathrm{H}^-}$ for a beam radius of r_c can be calculated via:

$$\frac{\Delta n_{\mathrm{H}^-}}{n_{\mathrm{H}^-}} = 1 - \exp\left(-\frac{\sigma_\mathrm{PD}\lambda}{\mathrm{hc}}\frac{E_\mathrm{pulse}}{\pi r_\mathrm{c}^2}\right) \quad . \tag{5.24}$$

Thus, in order to destroy more than 99 % of negative hydrogen ions within the laser beam volume by a single laser pulse at 1064 nm, a Nd:YAG laser has to

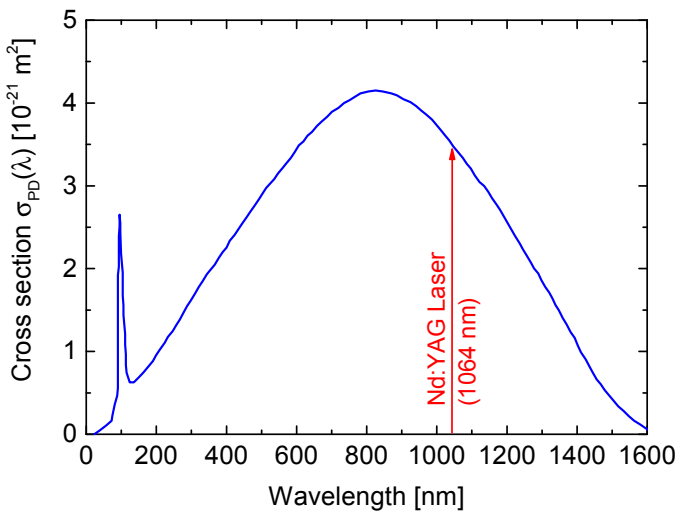

Figure 5.8: *Cross section for the photodetachment process after [Lab77].*

provide a laser pulse energy per unit area of E_{pulse}/A of 245 J/m^2. This energy density lies within the typical specification of commercial available high power Nd:YAG lasers (see for instance [Qua16]).

It has to be noted that using a wavelength of 1064 nm is beneficial as the corresponding photon energy is too low for other photo induced processes that produce electrons like photo-ionisation of ground state[5] H and H_2 and consequently the negative ion density determination is not influenced by these particle species. Furthermore, the wavelength is advantageous when a small amount of impurities like oxygen is present. For the corresponding negative oxygen ions O^-, O_2^- and O_3^- the electron affinities are 1.46 eV, 0.44 eV and 2.1 eV respectively. Thus, for O^- and O_3^- the photon energy of 1.17 eV isn't sufficient for affecting negative oxygen photodetachment. In [Bac93] the detachment efficiency for O_2^- has been investigated and found to be sufficiently low to be neglected compared to negative hydrogen ions at the same pulse energy.

Influence of a Magnetic Field

In the presence of a magnetic field, charged particle motion is anisotropic and the electron current measured by a Langmuir probe is reduced. However, this is not affecting the measurement of the relative negative ion density via laser

[5] For excited hydrogen atoms and molecules an ionisation and further excitation or dissociation can occur but is negligible due to the low density of such particles.

photodetachment as the effect of a magnetic field on electrons is constant over time and only the relative change of the electron current before and after a laser pulse is measured. As has been described in chapter 5.2, it is dependent on the dimensionless parameter κ whether the determination of the electron density and of the positive ion density is possible in the presence of a magnetic field. When a determination of the positive ion density is possible, absolute negative ion densities can be derived by the use of quasi-neutrality via

$$n_{\mathrm{H}^-} = n_{\mathrm{i}+}\left(1 - \frac{1}{\alpha+1}\right) \quad \text{with} \quad \alpha = \frac{n_{\mathrm{H}^-}}{n_{\mathrm{e}}} \quad . \tag{5.25}$$

5.4 Modelling of H^- Volume Processes

The negative ion density resulting from volume processes can be determined in a global, i.e. 0-dimensional approach by balancing the different production and destruction rates described in sections 4.1.1 and 4.1.3. The rate equation is given by

$$\begin{aligned} &\sum_{\nu} n_{\mathrm{H_2(X},\nu)} n_{\mathrm{e}} X^{\nu}_{\mathrm{DA}}(\mathrm{EEDF}) = \\ &= n_{\mathrm{H}^-}(n_{\mathrm{e}} X_{\mathrm{ED}}(\mathrm{EEDF}) + n_{\mathrm{H}} X_{\mathrm{(non)AD}}(T_{\mathrm{H}}, T_{\mathrm{H}^-}) + \\ &+ n_{\mathrm{H_2}} X_{\mathrm{CD}}(T_{\mathrm{H_2}}, T_{\mathrm{H}^-}) + \sum_{\mathrm{x}=1,2,3} n_{\mathrm{H_x^+}} X_{\mathrm{MN}}(T_{\mathrm{H_x^+}}, T_{\mathrm{H}^-})) \quad . \end{aligned} \tag{5.26}$$

This equation can be solved for n_{H^-} via the flexible solver *Yacora* [WDF09] when the corresponding cross section data are known. The required input data, i.e. the densities and temperatures of electrons, positive ions, atomic and molecular hydrogen particles can be determined experimentally for example. In the following this model is called *Yacora* H^-.

Within *Yacora* H^- the production rate via dissociative attachment is implemented vibrationally resolved by parameterizing the vibrational population $n_{\mathrm{H_2(X},\nu)}$ after equation (4.3). For a relative vibrational population after Boltzmann, P_ν is calculated via a vibrational temperature T_{vib} that is defined as input parameter. As described in chapter 4.1.1, in a low temperature, low pressure hydrogen plasma also a vibrational population can arise that is characterized by a superposition of two Boltzmann distributions with distinct vibrational temperatures. For this

case, the relative vibrational population is calculated within the model using:

$$P_\nu = \frac{(1-\beta)\exp\left(\frac{-\Delta E_\nu}{k_\mathrm{B}T_\mathrm{vib,1}}\right) + \beta\exp\left(\frac{-\Delta E_\nu}{k_\mathrm{B}T_\mathrm{vib,2}}\right)}{\sum_{\nu=0}^{14}(1-\beta)\exp\left(\frac{-\Delta E_\nu}{k_\mathrm{B}T_\mathrm{vib,1}}\right) + \beta\exp\left(\frac{-\Delta E_\nu}{k_\mathrm{B}T_\mathrm{vib,1}}\right)} \quad . \tag{5.27}$$

The weighting factor β is $\in [0,1]$ and $T_\mathrm{vib,1}$ describes the population of the low vibrational levels and $T_\mathrm{vib,2}$ correspondingly the population of the highly excited vibrational H_2 states. As described in section 5.1.1, the vibrational population up to $\nu = 3$ can be derived via OES yielding the vibrational temperature $T_\mathrm{vib}^\mathrm{OES}$. Thus, $T_\mathrm{vib}^\mathrm{OES}$ is used as experimentally determined input parameter $T_\mathrm{vib,1}$ in *Yacora* H^-. The measured population of $n_{\mathrm{H}_2,\nu\leq 3}$ can be well reproduced by a calculated population after equation 5.27 using $\beta = 0.05$ and consequently, β is chosen to be 0.05 fixed within the model. The second vibrational temperature $T_\mathrm{vib,2}$ is experimentally not accessible. It is taken as a free adjustable parameter to match the measurements within reasonable limits that have been assessed with the vibrationally resolved CR model *Yacora* H_2.

The positive ion density as well as the EEDF are experimentally determined via the Langmuir probe (see section 5.2). Within the model, the rate coefficients for dissociative attachment X_DA^ν are calculated on basis of vibrationally resolved cross section data provided by [JRS03], using a definable EEDF. Therefore, an externally calculated EEDF can be used directly via an input file. Optionally, for a Maxwellian EEDF the electron temperature can be used as input parameter[6]. Analogue to the calculation of X_DA^ν, the rate coefficient for electron detachment X_ED is calculated within the model taking the determined EEDF into account.

The neutral particle densities of atomic and molecular hydrogen as well as the corresponding temperatures T_H and T_{H_2} are determined via OES (see section 5.1). Within the range of within this work present neutral particle temperatures (between 500 and 1000 K) a negligible sensitivity of the corresponding rate coefficients on these temperatures, i.e. of $X_\mathrm{(non)AD}$ and X_CD is given. Following the reported negative ion temperatures of around 0.2 eV, measured by [NSB98, CBB95, DAB+89, BBB+91] in volume sources, at comparable plasma parameters, a fixed negative ion temperature of 0.2 eV is assumed. Thus, for (non-)associative detachment $X_\mathrm{(non)AD} = 2\times 10^{-15}\,\mathrm{m^3/s}$ and for collisional detachment $X_\mathrm{CD} = 1.3\times 10^{-18}\,\mathrm{m^3/s}$ is used in the model.

For mutual neutralisation, the sum of the different positive ion densities is ap-

[6] X_DA^ν are depicted in figure 4.1 for a Maxwellian EEDF.

proximated by using the experimentally determined positive ion density as derived from the Langmuir probe characteristics. Due to the efficiency of thermalization between particles of comparable masses, positive ion temperatures are assumed to be comparable to neutral particle temperatures. The rate coefficients for mutual neutralisation for this temperature range are nearly independent on the involved particle temperatures. Thus, for mutual neutralisation a combined value of $X_{\mathrm{MN}} = 1 \times 10^{-13}\,\mathrm{m}^3/\mathrm{s}$ is used in the model.

The introduced model allows for the calculation of n_{H^-} resulting from present volume processes. On basis of independently derived experimental data, the resulting negative ion density can be compared with n_{H^-} measured via laser photodetachment by varying $T_{\mathrm{vib},2}$. Like this, the relevance of the individual destruction mechanisms can be evaluated.

6 Experimental Setup and Diagnostic Systems

6.1 Experimental Setup

The investigations on caesium-free alternative materials for negative ion formation are carried out at the experimental setup HOMER (**HOM**ogeneous **E**lectron cyclotron **R**esonance plasma). The setup is an ECR experiment and provides ion source relevant parameters in combination with a high flexibility and diagnostic accessibility. A schematic drawing of the setup in front view is shown in figure 6.1. The discharge chamber is a cylindrical vessel of 7.5 cm radius and 31 cm height, manufactured of stainless steel. At a height of 15.5 cm four ports are symmetrically arranged at the cylindrical vessel, granting access for diagnostics, gas supply and the connection to the vacuum pumps. The minimal background pressure of some 10^{-5} mbar is maintained via a roughing pump in combination with a turbo molecular pump. For monitoring the background pressure a compact pressure gauge is used comprising a Pirani gauge and a cold cathode gauge. The gas supply is managed via mass flow controllers maintaining a fixed H_2 or D_2 gas flow of 9 sccm. By an inline-valve, installed in between the connection between the vessel and the pumps, the gas outflow is regulated and thereby the absolute working pressure is adjusted. A pressure range between 0.3 to 100 Pa is accessible, monitored via a gas type insensitive, capacitive pressure gauge.

The H_2/D_2 plasma are generated via a microwave ($f_{\mathrm{MW}} = 2.45$ GHz) introduced from the top of the vessel through a, for the microwave transparent, borosilicate window. The microwave is generated in a water cooled magnetron with a maximal output power of $P_{\max} = 1$ kW and directed into the discharge chamber via a wave guide system.
For resonant coupling of the microwave to the plasma electrons a magnetic field is created via a system of three DC current driven solenoids made from copper

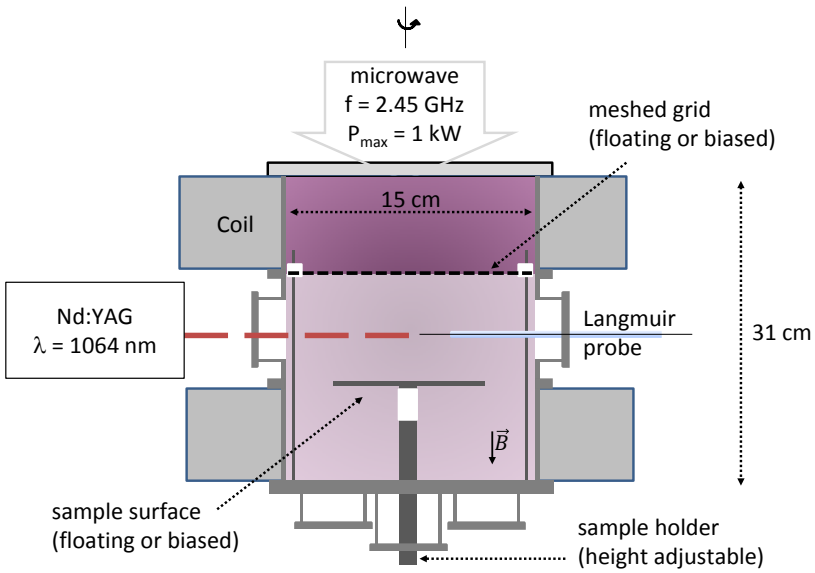

Figure 6.1: *Schematic drawing of the experimental setup HOMER (front view).*

tubes that are concentric surrounding the vacuum vessel. By two main solenoids of 198 windings each, a Helmholtz coil system is created that is symmetrically placed above and beneath the four aforementioned ports, allowing for creating a homogeneous magnetic field of 87.5 mT at the height of the ports. A third solenoid of 70 windings is placed at the top of the experiment surrounding the borosilicate window, for providing a localized magnetic field increment at the introduction region of the microwave into the plasma accomplishing the high-field coupling of the microwave (see chapter 3.2). The serial to the two solenoids applied current at the top of the experiment and separately the current through the bottom solenoid is maintained by two distinct high-current generators. The current can be adjusted between 0 and 55 A. To remove heat loads caused by ohmic heating of the solenoids, a high pressure water cooling system (0.5 l/s at $p \gtrsim 32$ bar) is used for pumping water through the solenoids' copper tubes.
For maintaining the tandem-principle (see section 4.2) a meshed grid (radius $r \approx 7$ cm) is installed at a height of 19 cm relative to the bottom plate, electrically insulated against the grounded vessel walls. Thereby, the vessel volume is separated into a heated driver region of 2.1 l and a diffusive downstream region of 3.4 l. The meshed grid is manufactured of stainless steel wires which have a thickness of $d = 0.25$ mm each. The mesh size is 1 mm^2 resulting in a grid transparency of 64 % defined by the ratio of the total grid area to the sum of the mesh

area. The grid design is chosen to allow a significant amount of plasma particles to diffuse from the driver region to the downstream region while simultaneously limiting the microwave to the driver region. A bias control of the meshed grid relative to the grounded vessel walls is given by an electrical connection through a feedthrough at the vessel bottom.
For hosting sample materials within the diffusive downstream region a mounting platform of $6\times8.5\,\mathrm{cm}^2$ is present, manufactured of stainless steel and arranged perpendicular to the vacuum cylinder axis. The mounting platform is affixed via a ceramic coupling to a stainless steel hollow cylinder and is thereby electrically and thermally insulated. The sample holder as a whole (mounting platform and hollow cylinder) is vertically movable via a mechanical vacuum feedtrough at the bottom plate. This allows for performing distance scans by adjusting the sample holder position relative to the stationary probe (see below). The arrangement allows for variations of the distance between the mounting platform and the stationary probe of maximally 5 cm.
Via a coaxial heating wire a temperature of maximal 550 °C can be applied to the investigated sample by heating the mounting platform. The temperature is monitored by a coaxial thermocouple which is positioned inside the sample holder. A schematic of the sample holder including the arrangement of the heating wire and the thermocouple is shown in figure 6.2. Furthermore, the mounting platform can be biased against the grounded walls in a voltage range between ±40 V.

6.2 Diagnostic Systems

For monitoring purposes the potentials of the sample holder and the meshed grid relative to the grounded vessel walls are measured via multimeters. Furthermore, the diagnostic systems described in chapter 5 are applied. The line-of-sight (LOS) for OES and the position of the Langmuir probe and the laser photodetachment are located to the diffusive downstream volume above the sample surface. The plasma volume above the meshed grid is diagnostically not accessible within the present work. However, plasma parameters in this region are assessable via the extensive studies in [Die10].

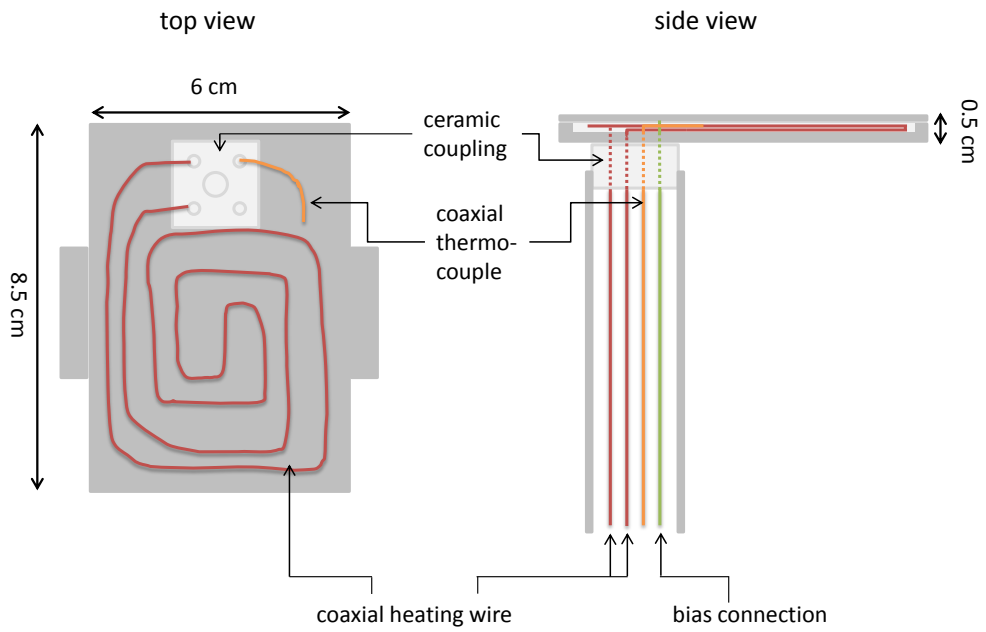

Figure 6.2: *Schematic drawing of the sample holder..*

6.2.1 Spectroscopic Systems

Two **spectroscopic systems** are used within the present work. For constantly monitoring the plasma emission of prominent emission lines during a measurement campaign a survey spectrometer is used that records a wide spectral range at once (200 – 1100 nm) with moderate spectral resolution. The plasma emission is collected via a lens head which is equipped with a quartz lens and the collected emission is transmitted via an optical fibre (600 μm diameter) to the Czerny-Turner type spectrometer having a focal length of 4.5 cm and a grating with 300 grooves per mm. The entrance slit width of the spectrometer is 25 μm and the apparatus profile is Gaussian with a FWHM of 1.5 nm at 400 nm and 1.2 nm at 850 nm. The CCD chip line has 2048 pixels with 14 $\times$ 200 μm^2 each. The corresponding LOS is stationary and directed through a quartz window parallel to the laser beam used for laser photodetachment into the volume above the investigated sample material.

For quantitative optical emission spectroscopy a spectrometer with higher resolution is used. The plasma emission is collected via a lens tube having a solid angle limiting aperture of 10 mm in diameter. Within the lens tube a quartz lens (focal length 75 mm) is mounted, focusing parallel collected light at the focal point where a UV enhanced optical fibre (400 μm in diameter) is placed. For suppressing higher diffraction orders of lower wavelengths an edge filter can be

introduced into the lens tube for measurements of emission lines above 520 nm. Being also of Czerny-Turner type, this second spectrometer has a focal length of 75 cm with a grid comprising a grating constant of 1800 mm^{-1}. The entrance slit width has been adjusted during this work to be 45 μm. The Gaussian apparatus profile has a FWHM of 23 pm at 400 nm monotonously decreasing to 17 pm at 850 nm. The CCD chip with 2500 $\times$ 600 pixel (12 $\times$ 26 μm^2 each) is actively cooled to -35 °C to reduce thermal noise. The LOS is directed parallel to the investigated sample and perpendicular to the LOS of the laser. Furthermore, the lens head is height adjustable, thus allowing for distance scans of the emission relative to the sample.

Calibration of the Spectroscopic Systems

For deriving plasma parameters via OES, the spectroscopic system has to be absolutely wavelength and intensity calibrated. Wavelength calibration was done by recording emission lines of known wavelength using a mercury and rare gas lamps. A derivation between the measured wavelength and values known from the spectroscopy database [KRR+15] of ± 0.01 nm has been identified which can be seen as negligible for the present application.
An intensity calibration has been performed by using an Ulbricht sphere, i.e. a diffuse and homogeneously emitting secondary radiation standard. For this light source the absolute emission is known and a calibration factor $f(\lambda)$ (which unit is $[(\mathrm{s\ m^2 nm(Cts/s)})^{-1}]$) can be derived by dividing the known emission of the Ulbricht sphere $[(\mathrm{s\ m^2 nm})^{-1}]$ by the emission measured with the present spectroscopic system [Cts] after normalisation to the integration time [s]. The calibration was performed in a spectral range between 400 and 850 nm, covering the for the present work relevant spectral range of the Balmer and Fulcher emission. In order to prevent the higher diffraction orders of lower wavelengths to interfere the measurements, an edge filter is used when emission lines above 520 nm are recorded. For the survey spectrometer the calibration factor was determined via a single full range spectrum, whereas for the second spectrometer the emission was recorded in 10 nm steps and linearly interpolated in between. The resulting calibration factor for a spectral range between 400 and 850 nm for the two spectrometers is presented in figure 6.3.

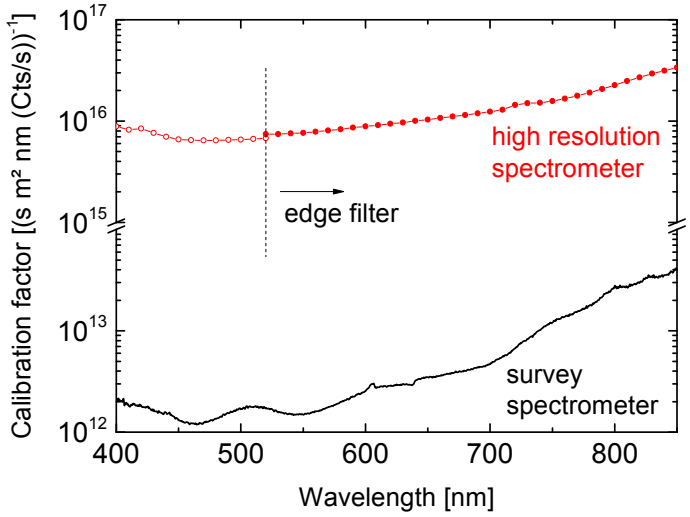

Figure 6.3: *Calibration factor for the applied spectroscopic systems including the corresponding lens heads, optical fibres and quartz window.*

Error estimation

Parameters derived via optical emission spectroscopy are influenced by different sources of errors. On the one hand, an uncertainty arises from the determination procedure of the calibration factor via the known and measured Ulbricht sphere emission. On the other hand a limited accuracy is given for the determination of the emissivity via the line integral by fitting the measured spectral intensity. Furthermore, an uncertainty is linked to the accounted plasma length. This results in a measurement error for the emissivity of $\pm 10\,\%$. For deriving parameters via the applied CR models *Yacora H* [WDF09] and *Yacora* H_2 [WF01], errors arise together with the uncertainty for the emissivity determination from the input parameters like the limited accuracy of underlying cross section data and particle densities. Taking the input data for granted, an uncertainty of the determination of $n_{\mathrm{H}}/n_{\mathrm{H}_2}$ of $\pm 20\,\%$ is given. The sensitivity for deducing the gas, the vibrational and the atomic hydrogen temperatures is given only for temperatures exceeding the values given in table 6.1.

Table 6.1: *Uncertainties for parameters determined via OES.*

Parameter	Error
T_{gas}	$\pm 50\,\mathrm{K}$
T_{vib}	$\pm 500\,\mathrm{K}$
T_{H}	$\pm 250\,\mathrm{K}$

6.2.2 Langmuir Probe and Laser Photodetachment System

As described in section 5.3, for determining n_{H^-} the electron current at a distinct probe bias I_0 in steady state and the current including the signal increment caused by the laser induced photodetachment of H^-, $I_0 + \Delta I$, has to be measured together with the positive ion density. Therefore, a combined diagnostic system, comprising the control unit and data acquisition system for the Langmuir probe and the laser photodetachment diagnostic is used. The basic system has been developed and described in [Mai11] and was revised and recommissioned within the present work.
The Langmuir probe is installed horizontally in a fixed height of 17 cm relative to the bottom of the vessel. It is perpendicular oriented to the axis of the cylindrical vessel and thus to the present magnetic field lines. A variation of the relative position between the investigated sample surfaces and the probe is possible via the height adjustable sample holder. The probe tip, a 1 cm long tungsten wire of 50 μm radius, is placed in the centre of the plasma and thus centered above the sample material, allowing for local measurements. A borosilicate glass tube is used for hosting the electrical feedthrough and maintaining its electrical insulation against the plasma. For minimizing the noise level of the measured probe signal, the connection to the data acquisition system is completely coaxially shielded. A maximal probe bias of $U = \pm 100\,\mathrm{V}$ can be applied against the grounded vessel walls via a bipolar power supply.
For laser photodetachment a pulsed Nd:YAG laser is used, creating short laser pulses of 8 ns at the fundamental wavelength $\lambda = 1064\,\mathrm{nm}$. The laser system is capable to provide a maximal energy per laser pulse of 50 mJ with a maximal repetition frequency of 20 Hz. The line of sight of the laser beam is axially adjusted to the centre of the probe tip and the beam diameter is enlarged via a plane-concave lens to be 6 mm at the location of the probe tip.

The diagnostic system comprises a sophisticated triggering system which is required as the power output of the microwave that sustains the plasma is not stabilised. The power output and in turn the power deposition is oscillating with a frequency of about 48 kHz that is furthermore superimposed by an unsettled amplitude modulation. As a consequence, the electron density and thus the measured probe current is not constant at a fixed probe bias. For a biased probe of 35 V the measured probe current is depicted in figure 6.5 (a). The triggering sys-

tem ensures measurements at comparable plasma parameters by synchronizing the ignition of laser pulses to the probe current measurement via a quick-response circuit (reaction times in nanosecond range). In figure 6.4 an equivalent circuit diagram of the control unit and data acquisition system for the Langmuir probe and the laser photodetachment diagnostic is depicted. The measurement is basi-

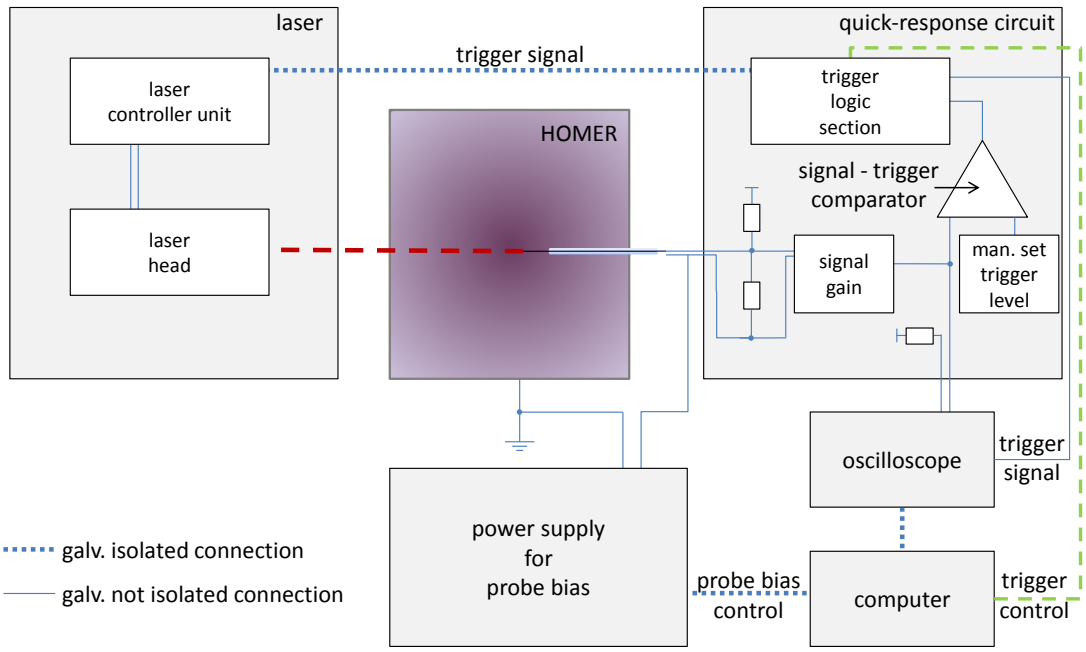

Figure 6.4: *Equivalent circuit diagram of the control unit and data acquisition system for the Langmuir probe and the laser photodetachment diagnostic.*

cally divided into two subsections. To illustrate the measurement procedure the correspondingly measured signals are presented in figure 6.5 (a) and in (b), (c): In a first step (figure 6.5 (a)), the oscillating current onto the constant biased probe is recorded over a time range of 1000 μs ($\approx$ 48 oscillations) to determine a mean current I_{mean}. The probe bias is therefore applied by the computer controlled power supply. This mean value is used to manually define the trigger level for a comparator in the quick-response circuit. When the constraint for the trigger is fulfilled, i.e. the measured current equals I_{trg}, the laser pulse is released and a detachment signal is subsequently recorded (figure 6.5 (b)). The signal is stored in a volatile buffer depending on the signal quality which is rated after the following characteristics:

- Laser pulse successfully triggered at defined set value in a tolerance range of $\pm$ 2.5 % of I_{trg}.
- Low RF noise level of $\lesssim$ 2 % within the signal 'shortly before' (-0.1 < t < -0.04 μs) and 'after' the detachment (1 < t < 1.5 μs).

Following this procedure ten single signals[1] are acquired with and without a shutter hindering the laser beam to enter the plasma and a corresponding mean current signals are calculated (figure 6.5 (b)). The current I_0 is consequently derived from these mean currents at $t = 0.0\,\mu$s. The difference of the recorded void measurements and the previously recorded currents with the laser entering the plasma is calculated to give ΔI. Subsequently $\Delta I/I_0 = n_{\mathrm{H^-}}/n_{\mathrm{e}}$ is derived. It has to be noted that the measured detachment signal which is presented in figure 6.5 (c) deviates from the theoretical evolution shown in figure 5.7. This basically can be attributed to the finite electrical response times of the applied triggering and data acquisition circuit.

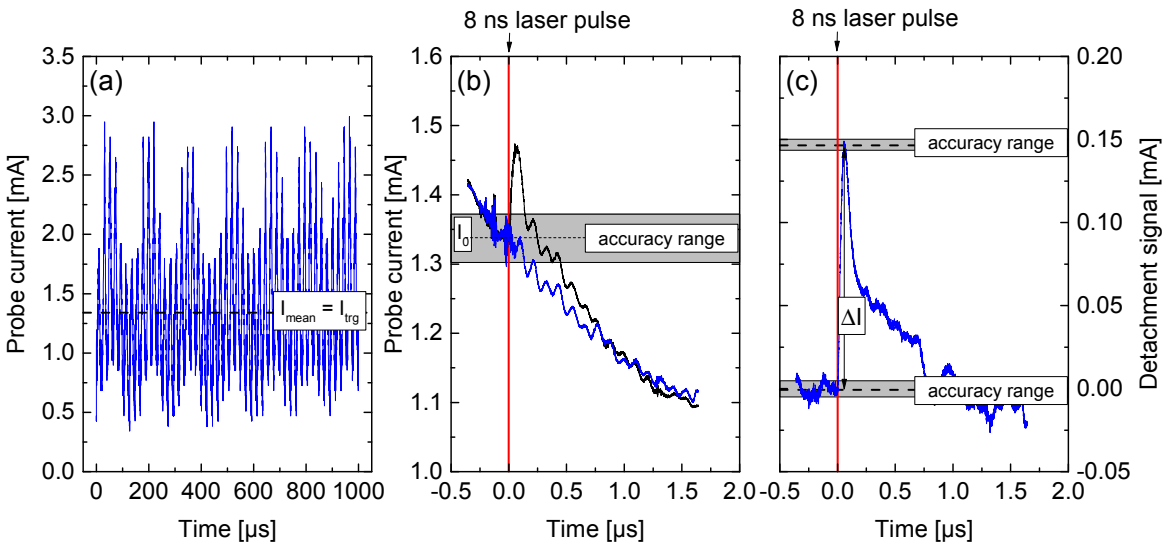

Figure 6.5: *Exemplary probe currents at constant probe bias of 35 V for laser detachment measurement: (a) Probe current for determining the mean value used for triggering the laser detachment measurement. (b) Mean values of ten acquired signals with and without the laser for determination of I_0. (c) Difference between signal and void measurements for determining ΔI.*

[1] After this number of recorded signals the difference between the mean value and the standard derivation have shown its minimal level.

Parameters for laser photodetachment

As described in section 5.3, several constraints have to be fulfilled for applying laser photodetachment as a diagnostic for measuring the negative ion density. For the determination of the external parameters fulfilling these constraints, distinct measurements were conducted at conditions comparable to the subsequent investigations on caesium-free alternatives, i.e. at 300 W discharge power and 1 Pa hydrogen gas pressure. Furthermore, a stainless steel sample in a relative distance of 4.5 cm to the Langmuir probe has been installed, not biased or heated.

The accurate measurement of the negative ion density is sensitive to the correct choice of the **collection radius** of the Langmuir probe together with the **laser beam radius**, where the collection radius of the probe has to be slightly smaller than the beam radius. The beam radius is predefined within this work to be 3 mm whereas the collection radius can be influenced via the applied probe bias. A lower limit of the probe bias can be approximated for known charged particle temperatures and densities using equation (5.23). For the given laser beam radius, a probe tip with 50 μm radius in a plasma with $T_\mathrm{e} = 1\,\mathrm{eV}$ and $n_\mathrm{e} = 1 \times 10^{16}\,\mathrm{m}^{-3}$ and a positive ion temperature of 0.05 eV the approximation leads to a bias of about 50 V.
Generally, a high probe bias is required for a high signal-to-noise ratio as for an increased bias an increased electron current is drawn. However, increasing the probe bias is limited as thermal stresses of the probe tip by high electron currents can result. The investigation of the probe bias at given experimental conditions was performed by investigating the evolution of $\Delta I/I_0$ for bias variations. Within these investigations, a plasma potential of $\phi_\mathrm{pl} \approx 1.4\,\mathrm{V}$ was determined. The probe bias was varied between 20 to 60 V, i.e. in a wide range of the electron saturation region. As the investigated probe bias range was fulfilling the constraint of being significantly above the plasma potential, a virtually constant $\Delta I/I_0$ was measured independent of the applied probe bias. Thus, at the given beam diameter, the collection radius of photodetached electrons is sufficiently large when the probe bias is chosen within the investigated bias range. However, for higher probe biases, an overall increasing RF noise of the measured signals evolved. Thus, in order to have a trade-off between a high signal-to-noise level and minimizing a potential stress and keeping the RF noise at a reasonable level, the probe bias was set to 35 V.
In a further campaign, the **laser pulse energy** was investigated regarding the

detachment efficiency (see equation (5.24)). This was done by measuring the evolution of ΔI at a constant probe bias of 35 V for varying laser pulse energy. In order to check the actually emitted pulse energy and its reproducibility the emitted pulse energy was furthermore measured at distinct relative energies with a Joulemeter. Therefore, the energy was recorded for ten pulses at a single relative energy and the standard deviation derived. In figure 6.6 the evolution of the ΔI together with the evolution of the measured pulse energy as a function of adjusted relative laser pulse energy is shown. The depicted signal increment ΔI is normalised to the maximally acquired ΔI which corresponds to $\Delta n_{\mathrm{H}^-}/n_{\mathrm{H}^-}$ (see equation (5.24)). As can be seen, the mean values of the measured laser

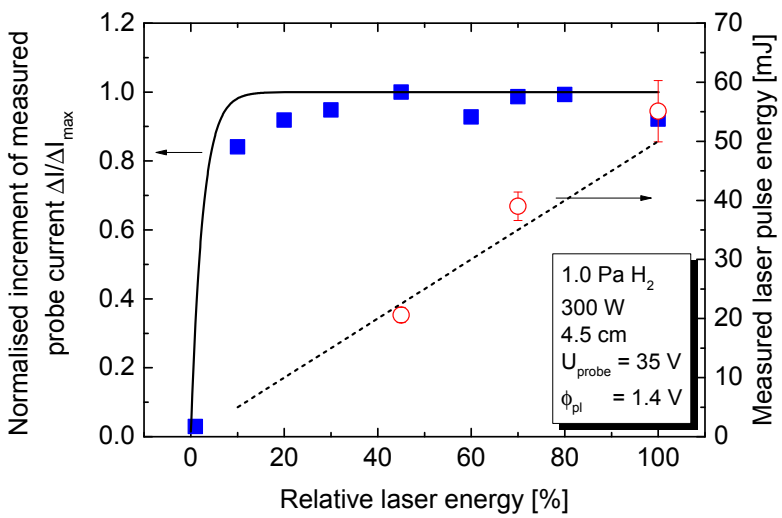

Figure 6.6: *Increment of measured probe current and via equation (5.24) calculated $\Delta n_{\mathrm{H}^-}/n_{\mathrm{H}^-}$ (left scale) as well as correlation of measured laser pulse energy (right scale) for relative laser pulse energy variations.*

pulse energies even exceed the manufacturer's data but with increasing pulse energy, an increasing standard deviation is given. Furthermore, it can be seen that the measured evolution of the normalised current increment well reproduces the detachment efficiency calculated via equation (5.24). For a relative laser pulse energy of $\gtrsim 20\,\%$, the measured and the calculated ratios saturate. Hence, the relative laser pulse energy is chosen to be 45 % (= 22.9 mJ), since the neutralisation efficiency exceeds 99.9 % and simultaneously a high reproducibility of the emitted laser pulse energy is given. Furthermore, a potential damage of components being within the laser line of sight, especially the quartz window and effects like secondary electron emission and probe material ablation induced by

interaction of the laser beam with the probe tip can be minimized [Mai11].

Error estimation

As described in chapter 5, the **Langmuir probe** is used to determine the EEDF, the plasma and floating potentials as well as the positive ion density. For the determination of these parameters uncertainties can arise resulting for example from a finite signal-to-noise ratio of the I-U characteristic.
For the determination of the EEDF the signal-to-noise ratio is typically in the order of two orders of magnitudes which corresponds for the conditions present within this work to an electron energy range of typically 14 eV. A systematic evaluation of the measurement error for the plasma and floating potential revealed an uncertainty of $\pm 7.8\,\%$ and $\pm 6.5\,\%$, respectively. The uncertainty for determining the positive ion density crucially depends on the effective positive ion mass. As this quantity is not accessible, the resulting error cannot be assessed. However, independent of this error, already the uncertainty of the effective probe area and of the procedure for fitting a theoretical positive ion current evolution to the measured current evolution is accompanied by an error of typically $\pm 11\,\%$.

The uncertainty for the absolute negative ion density is given by the accuracy of the positive ion density determination and by the error for determining ΔI and I_0. As indicated in figure 6.5 the error for determining the latter two parameters is also correlated with the signal-to-noise level. Taking this into account, the error has been assessed via the standard deviation, determined via several sets of ten measurements as described above at identical external parameters. An uncertainty for ΔI of maximally $\pm 7\,\%$ and for I_0 of less than $\pm 1\,\%$ was found leading to a Gaussian error for $\Delta I / I_0$ of $\pm 8\,\%$. Together with the typical error for the determination of the positive ion density of $11\,\%$, the Gaussian error for n_{H^-} is estimated to be in the order of $\pm 15\,\%$.

Benchmark

For the determined parameters the applied laser photodetachment diagnostic has been successfully benchmarked against cavity-ringdown spectroscopy (CRDS) by [Rau14]. The determination of the negative hydrogen ion density via this diagnostic is also based on the laser photodetachment process, but grants access without the necessity and uncertainty of additional parameter determination like the electron or positive ion density in case of laser photodetachment. Briefly, the

absolute negative ion density is measured via the decay time of a laser pulse that is introduced into a high-finesse cavity which consists of two highly reflective mirrors and the plasma volume. By comparing the decay times of a laser pulse traversing the cavity with and without the plasma and thus with and without H^-, the negative ion density can be determined[2]. Although being highly reliable, CRDS only provides access to the line of sight averaged negative ion density. However, the design of the experimental setup HOMER is focused on providing radially homogeneous plasma profiles (see investigations e.g. on density and potential profiles in [Die05]). Therefore, negative ions determined via CRDS and laser photodetachment are comparable.

[2]A more detailed description of this diagnostic can be found for example in [OD88].

7 Initial Basic Studies

In negative ion sources as well as in the present experimental setup HOMER, the negative ion density is a superposition of surface produced H^- and those produced in volume processes. Therefore, a surface induced enhancement of n_{H^-} is only observable when the amount of surface produced H^- formation is at least comparable to the one coming from negative ion related volume processes. Hence, a comprehensive understanding of the volume processes supports the investigations on caesium-free alternative materials. Insight into present volume processes is provided by measuring the absolute negative ion density together with plasma parameters related to the volume processes and applying the 0-dimensional model *Yacora* H^-, described in section 5.4.

Two reference cases are investigated in the context of this work: on the one hand measurements performed with a bare stainless steel reference sample, for which due to the high work function, H^- surface production is negligible and consequently give access to the pure volume processes. And on the other hand, measurements of the enhancing effect on the negative ion density induced by the evaporation of caesium into the experimental setup, since a suitable caesium-free alternative material should result in at least comparable or even exceeding negative ion densities.

Within this work, several caesium-free materials are investigated and thus, the reproducibility of the negative ion density measurement after exchanging the sample material has to be checked. Therefore, measurements with the stainless steel reference sample at constant external conditions are performed throughout different campaigns.

7.1 Investigations on Bare and Caesiated Stainless Steel

7.1.1 The H^- Volume Processes at HOMER

First basic investigations on the H^- volume processes are performed with the none actively heated stainless steel reference sample for a variation of pressure between 0.3 and 3 Pa at 300 W discharge power and a standard relative distance between the stationary Langmuir probe and the sample surface of 4.5 cm, i.e. its maximal distance (see sketch figure 7.1). These experimental conditions are used as they allow for investigating a large plasma parameter variation in a relevant range in combination with a minimized influence of the sample holder. It has to be noted that for later measurements using materials where a direct negative ion surface production is investigated, a smaller distance between the sample surfaces and the Langmuir probe will be used and the pressure will be set to the ion source relevant value of 0.3 Pa. Within these investigations, respective measurements with the stainless steel reference will be performed.
For the following investigations, the stainless steel sample has been mechanically polished and cleaned with purified water, acetone and isopropyl alcohol prior to installation into the vacuum vessel. To minimize conditioning effects, i.e. changing plasma parameters due to thermalization of the experimental setup and/or a saturation of particle ad- and desorption processes on the walls, measurements are started one hour after starting the plasma.

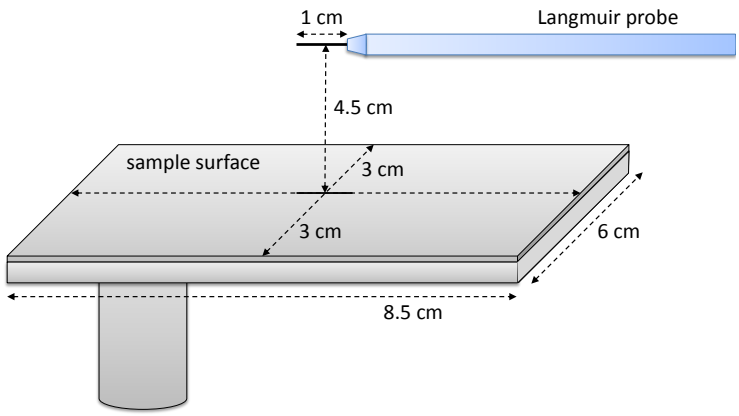

Figure 7.1: *Sketch to illustrate the relative position between the sample surface and the Langmuir probe tip.*

In figure 7.2 the measured negative ion density is depicted as a function of pressure. The negative ion density lies between 1.0 and $2.8\times10^{15}\,\mathrm{m}^{-3}$, peaked at 0.5 Pa. The corresponding negative ion to electron density is about 10 %, i.e. comparable to typical values in negative ion source based on the pure volume process [Bac00, SBB+06].

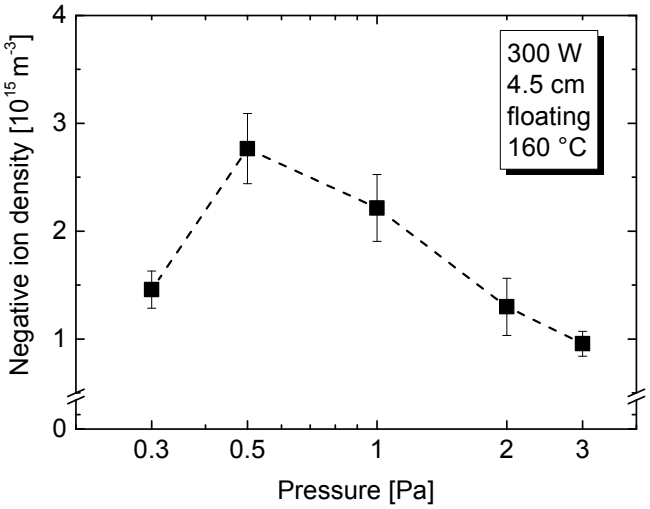

Figure 7.2: *Negative ion density as a function of pressure for the stainless steel reference sample.*

Plasma Parameters Correlated with H^- Volume Processes

The measured negative ion density is a consequence of negative ion volume formation via dissociative attachment which is balanced by mutual neutralisation, (non-)associative, collisional and electron detachment. Thus, the negative ion density is sensitive on the electron and positive ion density, the density and distribution of vibrationally excited molecules, the atomic hydrogen density and the EEDF.

In figure 7.3 the evolution of the positive ion density is depicted which is correlated with the electron density via the quasi-neutrality. Additionally the electron current measured at 35 V sample bias, i.e. at the default probe bias for laser photodetachment is shown. This depicted current data gives a measure of the relative evolution of the electron density for pressure variations.

As can be seen, both quantities show the same dependence on pressure variation. The positive ion density ranges between 1.6 and $3.4\times10^{16}\,\mathrm{m}^{-3}$ and is peaked at 1 Pa.

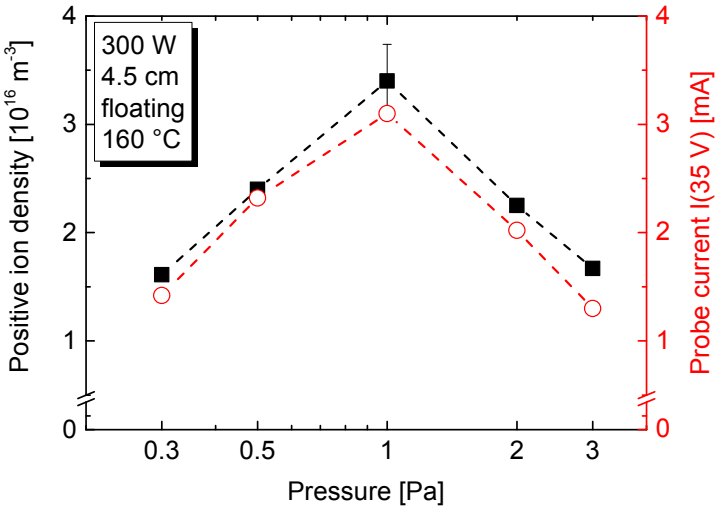

Figure 7.3: *Positive ion density determined via OML and measured probe current at a probe bias of 35 V as a function of pressure for the stainless steel reference sample.*

A direct access to the EEDF is given via the Langmuir probe. Over the whole investigated pressure range the measured EEDFs are Bi-Maxwellian. Exemplary for 1 Pa, the corresponding EEPF and a theoretical EEPF calculated after equation (3.8) (normalised to $n_e = 1$) with $T_{e,1} = 0.6\,\text{eV}$, $T_{e,2} = 3.6\,\text{eV}$ and $\beta = 0.11$ is depicted in figure 7.4 (a).
It has to be noted that the Bi-Maxwellian EEDF character is no consequence of the present meshed grid, as a Bi-Maxwellian EEDF also was measured in the absence of the meshed grid (not shown here). In fact, its presence in molecular plasmas is also reported throughout the literature (for example by [BF94]). It is dominantly induced in hydrogen discharges by electron impact excitation of ro-vibrational $H_2(X)$ states leading to a depletion of the amount of low energetic electrons and an according accumulation of lowest energetic electrons.

Data analyses via OES is based on a Maxwellian EEDF (see model description of *Yacora H* in [WDF09] and *Yacora* H_2 in [WF01]) and in figure 7.4 (a) a corresponding Maxwellian EEPF is additionally plotted, calculated for an electron temperature of 2.7 eV derived via OES by [Fri15]. The population of excited atomic levels (e.g. for the Balmer emission) via electron impact excitation requires electron energies which are above the excitation threshold energies ($\gtrsim 11\,\text{eV}$). Hence, electron temperatures deduced via OES T_e^{OES} are expected to be closer to

$T_{e,2}$ than $T_{e,1}$, i.e. the electron temperature deduced via Langmuir probe, which describes the higher energetic electron ensemble.

In figure 7.4 (b) the evolution of the 'electron temperatures' $T_{e,1}$, $T_{e,2}$ and T_e^{OES} is shown as a function of pressure. The characteristic 'electron temperature' $T_{e,1}$ decreases with increasing pressure from 0.6 to 0.4 eV and in case of $T_{e,2}$ from 5 to 3.6 eV. The corresponding weighting factor β shows a minor dependency on pressure variations: the low energetic ensemble represents the majority of electrons and β is about 10 %. A comparable trend is measured for the evolution of the electron temperature derived via OES, i.e. decreasing with increasing pressure from 3.1 down to 2.1 eV. Thus, via both diagnostics, an decreasing mean electron energy with increasing pressure is derived, which is in accordance to the ionisation balance described in section 3.3.
In the following, the Bi-Maxwellian EEDFs derived via the Langmuir probe are applied for modelling the negative ion density via *Yacora* H^- as the involved processes are highly sensitive to the electron energy distribution in the low energy range. For parameter evaluations via OES, i.e. T_{vib} and n_H/n_{H_2} electron temperatures deduced via OES are used for consistence.

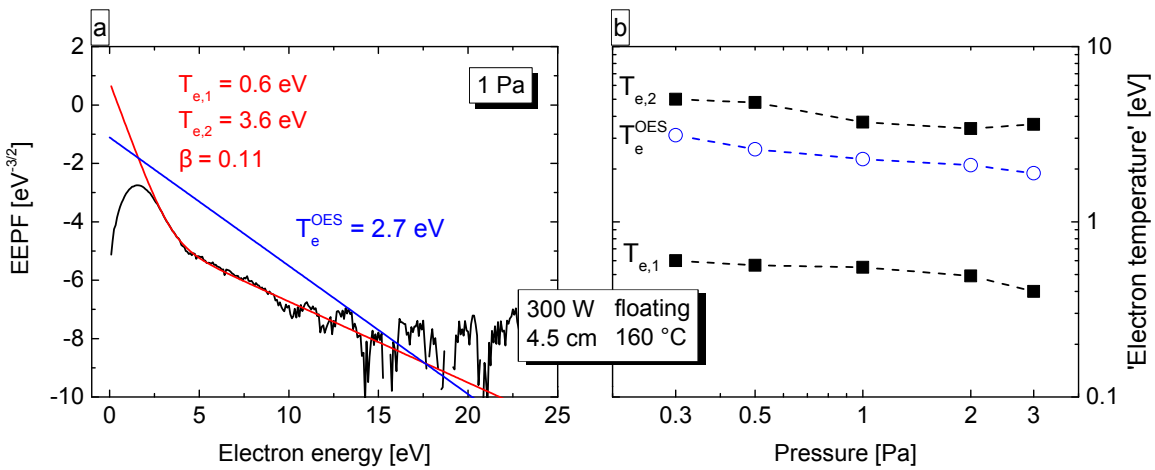

Figure 7.4: *(a) Measured and modelled EEPFs for stainless steel at 1 Pa. (b) Evolution of the 'electron temperatures' characterising the Bi-Maxwellian EEPF $T_{e,1}$, $T_{e,2}$ and the electron temperature determined via Yacora H [WF01, Fri15] for pressure variation.*

In figure 7.5 the evolution of the vibrational temperature and the gas temperature are shown. The determined vibrational temperature decreases from 3700 to 3100 K with increasing pressure. Within the error margins, a virtually constant

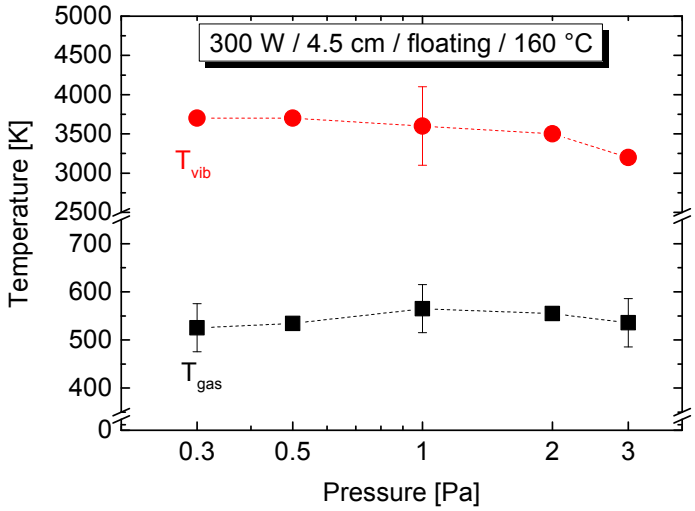

Figure 7.5: *Vibrational temperature T_{vib} and gas temperature as function of pressure variations for stainless steel sample.*

gas temperature of about 550 K is measured.

For determination of the atomic to molecular density ratio, the emission of H_γ and the Fulcher system have to be known. Independent of pressure, the measured line profile of the Balmer line is characterised by the superposition of two Gaussian profiles with different FWHM[1]. The spectral intensity measured at 1 Pa pressure and 300 W discharge power is exemplarily shown in figure 7.6 including the fitted Gaussian line profiles and the superposition of both calculated ones.

As described in section 5.1.2 the presence of a multi-Gaussian emission line profile implies the presence of different excited atomic hydrogen ensembles that are not thermalized among each other, i.e. are characterised by different temperatures. Evaluated via *Yacora H* and the corresponding collisional frequencies for thermalization with the background gas ($\sim 10^4\,\mathrm{s}^{-1}$) and de-excitation via spontaneous emission ($\sim 10^6\,\mathrm{s}^{-1}$), their population can be assigned to be coupled to different species which are the electronic ground state (via direct electron impact excitation) and the H_2^+ molecular ion (via dissociative recombination). For the shown example, the Doppler broadened line profiles yield temperatures of $T_{\mathrm{H}^*_{\mathrm{cold}}} = 500\,\mathrm{K}$ and $T_{\mathrm{H}^*_{\mathrm{hot}}} = 3\,\mathrm{eV}$ which can be attributed to come from an ensemble populated via direct excitation of with the background gas thermalized H(n=1) in case of the narrow peak and from a population via dissociative recombination i.e. cou-

[1]This characteristic is present for all measured Balmer lines.

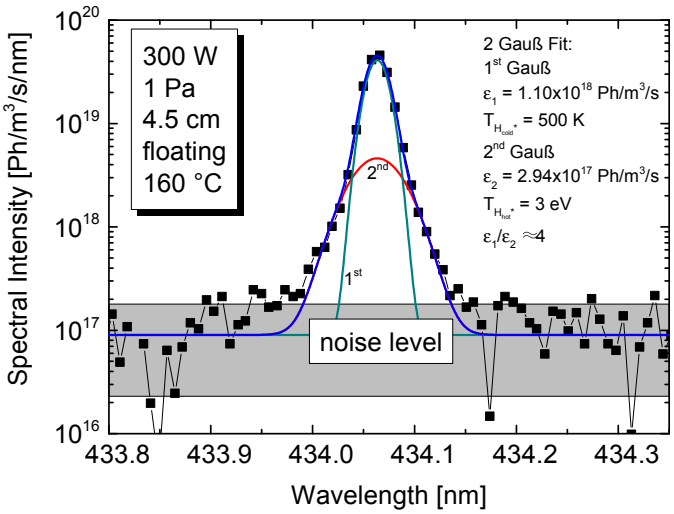

Figure 7.6: *Spectral intensity of the measured H_γ emission line including a two Gaussian fit.*

pled to H_2^+ in case of the broad peak. This is furthermore consistent with the given comparability of the determined gas temperature and $T_{H^*_{cold}}$ (see figure 7.5) which is measured over the whole investigated pressure range.

In the presence of a significant population of H(n=5) via processes coupled to further particle species besides H, the determination of n_H/n_{H_2} after equation (5.9) still holds, when the emitting particle ensembles are spectroscopically well distinguishable. Since this constraint is fulfilled, the atomic to molecular hydrogen density ratios can be evaluated via equation (5.9) taking only the narrow peak of the H_γ emission line into account.
The corresponding evolution of n_H/n_{H_2} for pressure variations is shown in figure 7.7: n_H/n_{H_2} ranges between 9.5 and 16.3 % and is peaked at 1 Pa.

Modelling negative ion densities

The negative ion density modelled via *Yacora* H^- on basis of the presented plasma parameters is plotted as a function of pressure together with the measured n_{H^-} in figure 7.8. For modelling, the vibrational population of $H_2(X, \nu)$ is calculated for a single Boltzmann distribution characterised by the diagnostically determined vibrational temperatures (shown in figure 7.5).
As can be seen, the modelled negative ion densities on basis of experimental determined parameters do not reproduce the measured data. Independent of pressure,

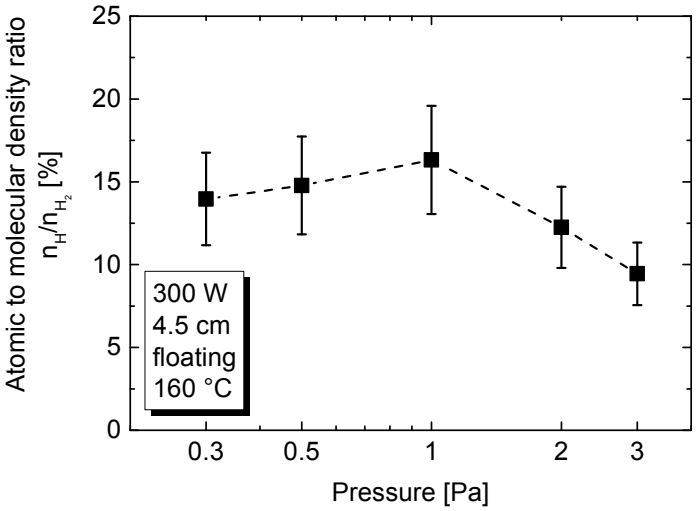

Figure 7.7: *Evolution of the atomic to molecular density ratio determined via the emissivities of the narrow peak of H_γ and the Fulcher system.*

modelled negative ion densities are more than one order of magnitude lower than the measured ones. It can be excluded that this deviation is a consequence of negative ion surface formation at the stainless steel sample as a comparable deviation has been reported in [Mai11] for measurements performed at HOMER without any sample holder installed. It can be furthermore excluded that this deviation results from negative ions produced in the driver region and diffuse into the downstream region as corresponding negative ions are not able to traverse the sheath of the meshed grid due to their low energy.

The formation of negative ions via dissociative attachment significantly depends on the population of vibrationally highly excited states with $\nu \geq 5$ (see section 4.1.1) which are diagnostically not accessible with the applied diagnostics (see section 5.1.1). An increased population of such vibrationally highly excited states can result by a redistribution via electron impact excitation of singlet $H_2(B)$ and $H_2(C)$ states. However, for such a redistribution typically higher mean electron energies are necessary than have been measured.
Sufficiently high mean electron temperatures are expected in the heated driver region, according to measurements performed by [Die10] and [Mai11] at HOMER

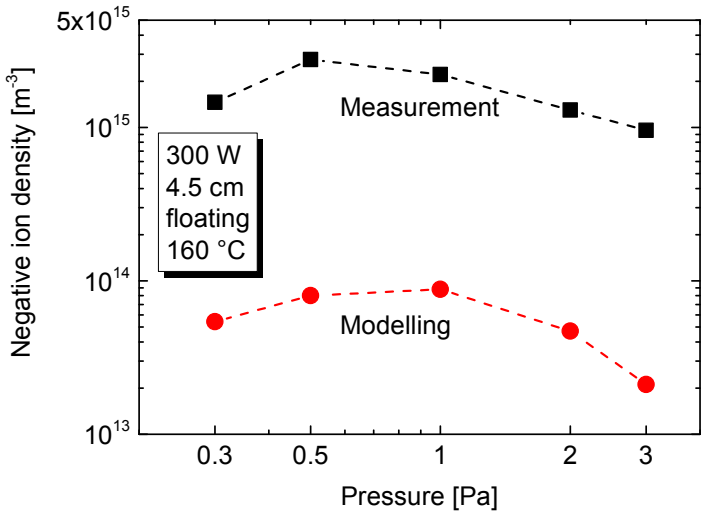

Figure 7.8: *Evolution of the measured and modelled negative ion density. Modelling is based on a vibrational population of $H_2(X, \nu)$ calculated with a single Boltzmann distribution corresponding to the measured T_{vib}.*

without the meshed grid installed[2]. Since vibrationally excited H_2 molecules are metastable, they can diffuse into the downstream region of the meshed grid after they have been formed in the driver region and allow for efficient negative ion formation, where the negative ion densities are measured.

An increased population of vibrationally highly excited H_2 can be addressed in *Yacora* H^- via a superposition of two Boltzmann distributions characterised by the vibrational temperatures of the low vibrational states $T_{\mathrm{vib},1}$ and highly excited states $T_{\mathrm{vib},2}$. This allows for fitting the modelled negative ion density to the measured n_{H^-}, by taking the diagnostically determined vibrational temperature $T_{\mathrm{vib}}^{\mathrm{OES}}$ for $T_{\mathrm{vib},1}$ and adapting $T_{\mathrm{vib},2}$ as free parameter. In figure 7.9 (a) the correspondingly modelled and measured negative ion densities (identical curve) are shown as a function of pressure together with the accuracy range of the measurement indicated by the dotted red lines. Modelled data well reproduce the measurement for $T_{\mathrm{vib},2}$ shown also as a function of pressure in figure 7.9 (b). The uncertainty of $T_{\mathrm{vib},2}$ deduced by fitting modelled data within the accuracy of measurement is maximally $\pm 330\,\mathrm{K}$ (dotted red lines). The vibrational temperature $T_{\mathrm{vib},2}$ lies between 7700 and 10300 K, peaked at 0.5 Pa. The corresponding relative vibrational coefficient P_ν (see equation (5.27)) is comparable to those calculated

[2]It is reported that at comparable parameters electron temperatures reached up to 3 eV.

by [Wün14] for an electron temperature of 4 eV (see figure 4.2), implying that vibrational temperatures deduced by fitting modelled negative ion densities to measured ones are reasonable.
For such high $T_{\mathrm{vib},2}$, the relative vibrational coefficient for $\nu \geq 4$, $P_{\nu \geq 4}$, is increased by up to three orders of magnitude compared to one described by a single Boltzmann distribution with $T_{\mathrm{vib}} = T_{\mathrm{vib}}^{\mathrm{OES}}$. Since the rate coefficient for dissociative attachment is highest for vibrationally highly excited states, this results in a significant increment of negative ion formation via the dissociative attachment process.

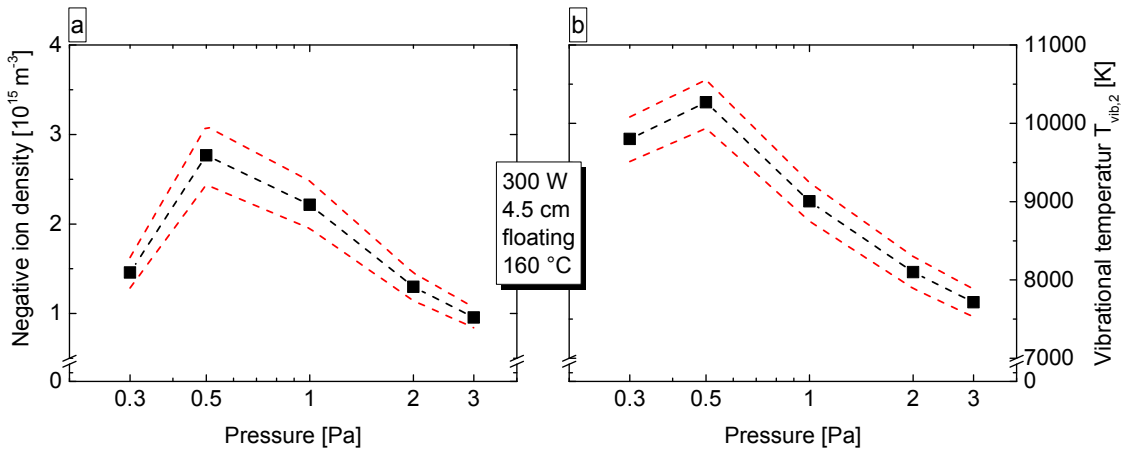

Figure 7.9: *Evolution of (a) the measured and modelled negative ion density and of (b) the free parameter $T_{\mathrm{vib},2}$ for adapting modelled to measured data together with the accuracy range indicated by the dotted red lines.*

The achieved agreement between measured and modelled H^- allows for an identification of the dominant destruction mechanisms via the 0-dimensional model *Yacora* H^-. The evolution of the different shares of destruction channels for H^- with pressure is shown in figure 7.10. Over the whole pressure range, negative ions are dominantly destroyed by collisions with neutral atoms. The associative and non-associative detachment rate contributes to more than 74 % of the total negative ion destruction, monotonously increasing with increasing pressure. Electron detachment and mutual neutralisation have a comparable share for the destruction, representing between 1.7 and 13 % of the total destruction channels. Despite n_{H_2} representing the dominant particle species within the plasma, the destruction of negative ions via collisions with hydrogen molecules, i.e. via collisional detachment has a minor share of less than 1 % independent of pressure.

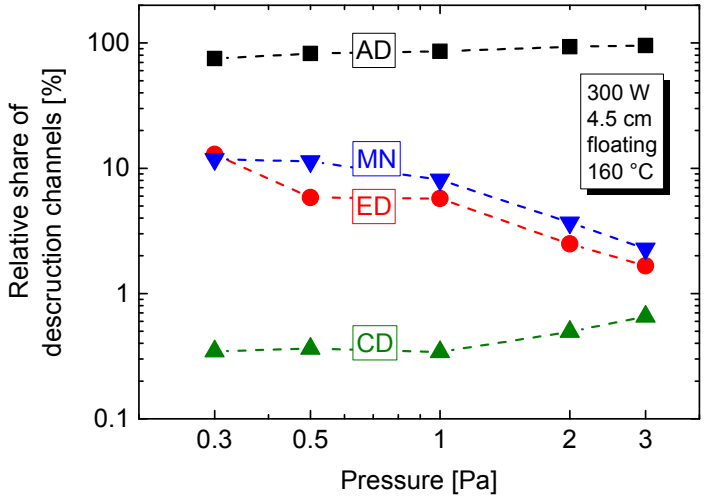

Figure 7.10: *Evolution of the relative shares of H^- destruction via associative and non-associative detachment (AD), electron detachment (ED), mutual neutralisation (MN) and collisional detachment (CD) as a function of pressure.*

Following this, a simplified equation for calculating the negative ion density by balancing the volume formation with the destruction channels is given and equation (5.26) transforms to:

$$n_{\mathrm{e}} n_{\mathrm{H_2}} \sum_{\nu} P_{\nu} X \nu_{\mathrm{DA}}(\mathrm{EEDF}) \approx n_{\mathrm{H}} n_{\mathrm{H^-}} X_{(\mathrm{non})\mathrm{AD}} \tag{7.1}$$

which yields:

$$n_{\mathrm{H^-}} \approx \left(\frac{n_{\mathrm{H}}}{n_{\mathrm{H_2}}}\right)^{-1} n_{\mathrm{e}} \frac{\sum_{\nu} P_{\nu} X \nu_{\mathrm{DA}}(\mathrm{EEDF})}{X_{(\mathrm{non})\mathrm{AD}}} \quad . \tag{7.2}$$

Thus, the evolution of the negative ion density for pressure variations is caused dominantly by the evolution of the atom to molecular density ratio, the electron density, the EEDF and the relative vibrational population:
An increment of $n_{\mathrm{H}}/n_{\mathrm{H_2}}$ is correlated due to the reverse correlation, with a correspondingly decreasing negative ion density. Since $n_{\mathrm{H}}/n_{\mathrm{H_2}}$ slightly increases in the pressure range between 0.3 and 1 Pa and decreases by about 42 % for higher pressure, the evolution of $n_{\mathrm{H}}/n_{\mathrm{H_2}}$ results in a slight decrease of $n_{\mathrm{H^-}}$ in the pressure range between 0.3 and 1 Pa and a significant increment for increasing pressure.
The evolution of the electron density is assessed via the positive ion density evolution shown in figure 7.3 which is peaked at 1 Pa. A pronounced dynamic of the

electron density is given which leads due to the linear dependence in a comparable evolution of n_{H^-}.
Regarding the evolution of X_{DA}^{ν} as a function of T_{e} shown in figure 4.1 the dissociative attachment rate coefficient for $\nu \leq 7$ significantly decreases for a decreasing electron temperature with $T_{\mathrm{e}} \leq 1$ and slightly increases for higher vibrational states. The measured mean electron energies are comparable and an according correlation of the corresponding X_{DA}^{ν} is given, for the evolution of the measured mean electron energies: With increasing pressure, the changing EEDF causes a reduction of dissociative attachment rate coefficients for $\nu \leq 7$ by up to 50 % while the rate coefficients are increasing by up to 24 % for higher vibrational states. However, the influence of the EEDF evolution is significantly depending on the evolution of the relative distribution of vibrationally excited states.
The described evolution of $n_{\mathrm{H}}/n_{\mathrm{H}_2}$ and n_{e} would lead to a negative ion density evolution peaked at 1 Pa and decreasing due to the contrary influences of $n_{\mathrm{H}}/n_{\mathrm{H}_2}$ and n_{e} by only 15 % for increasing pressure. The measured negative ion density decreases between 1 Pa and 3 Pa by 57 %. This is mainly caused by the decreasing population of vibrationally highly excited states, i.e. of $T_{\mathrm{vib},2}$ and shows the pronounced influence of this parameter.

7.1.2 Effect of Caesiation of a Stainless Steel Sample

After having evaluated the evolution of the n_{H^-} background coming from pure volume processes, the second reference case was investigated by in-situ application of caesium onto a stainless steel sample for investigating the negative ion density enhancement by H^- surface formation. For these investigations the sample holder is modified by a support structure allowing for the application of an alloy caesium dispenser [Alv15]. Via this support structure the caesium dispenser can be placed in a fixed distance of 2 cm relative to the sample while being electrically and thermally insulted from the sample holder. The evaporation rate of caesium is controlled by the electrical current running through the dispenser.
For ensuring that surface produced negative ions are measured by the diagnostic system, the mean free path of surface produced negative ions has to be higher than the distance between the sample surface and the stationary Langmuir probe used for laser photodetachment. The mean free path of surface produced negative ions can be estimated by taking the accelerating sheath potential and the dominant loss channel into account: The sheath potential can be assessed via the potential difference of the sample and the plasma potential. Measurements are

conducted at 0.3 Pa and 300 W discharge power where the dominant loss mechanism is given by collision of negative ions with atomic hydrogen (see section 7.1.1). As surface produced negative ions are accelerated within the sheath according to the measured potential difference to about 2 eV, the mean free path for surface produced negative ions can be estimated to be 2.8 m. The distance between the stainless steel sample and the stationary Langmuir probe is set to 2.5 cm and thus a high probability is given that all surface produced negative ions are detected with the applied diagnostic system.
For monitoring the caesium evaporation, the emission of caesium resonance line at 852 nm is measured. The impact of caesiation over time is directly accessible by monitoring the negative ion density evolution. Furthermore, plasma parameters like the EEDF and positive ion density as well as the plasma emission are monitored.

In figure 7.11 the time evolution of the positive and the negative ion density is shown together with the evolution of the caesium emission at 852 nm. Starting without any caesium, virtually constant positive and negative ion densities of $1.3\times10^{16}\,\mathrm{m}^{-3}$ and $1.0\times10^{15}\,\mathrm{m}^{-3}$, respectively, are measured. After 53 minutes, caesium evaporation[3] is started which is observable at the increase of the caesium emission. Simultaneously, an immediate increase of the negative ion density by a factor of up to 2.5 is measured. In contrast, the positive ion density is virtually not affected. According to the increasing caesium emission, an increment of the caesium flux onto the stainless steel sample is given resulting in a reduction of the stainless steel sample's work function[4] which allows for the formation of negative ions at the sample material's surface. With on-going caesium evaporation, after about 82 minutes, the caesium emission starts decreasing. Accordingly, the caesium flux onto the sample surface is reduced which leads to a degradation of the sample's work function and thus a reduction of the H^- surface formation. Thus, the negative ion density slightly decreases within one hour of operation down to a value of $2\times10^{15}\,\mathrm{m}^{-3}$ correlated to a decreasing caesium emission.

It is well known that the application of caesium also can affect the plasma potential (see for instance [FF13b]). As described in section 3.4, this is a consequence

[3] A maximal caesium density of $n_{\mathrm{Cs}} \approx 0.5 \times 10^{15}\,\mathrm{m}^{-3}$ is determined via OES.
[4] By [GWF11] a reduction of a molybdenum sample's work function down to 2.2 eV was measured when the caesium flux was increased by evaporation in an hydrogen discharge comprising comparable parameters. A comparable effect was measured by [Fri15].

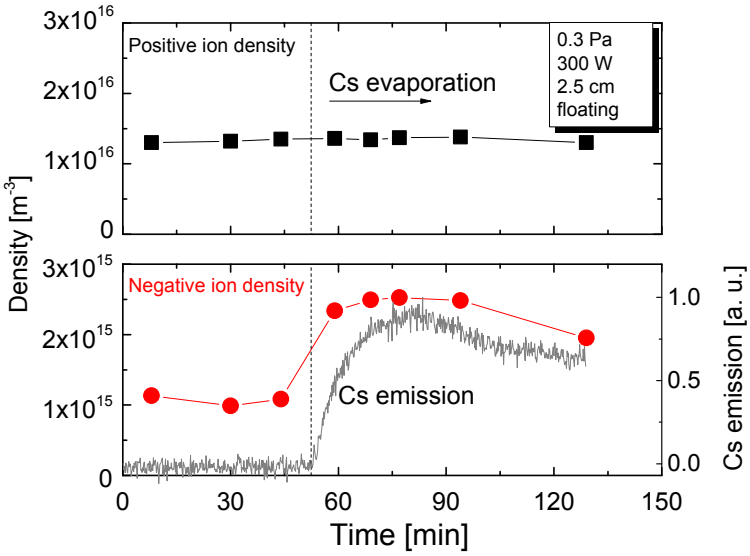

Figure 7.11: *Time evolution of positive and negative ion density as well as caesium emission before and while evaporation of caesium to a stainless steel sample.*

of an increasing density of negative particles in the vicinity of a caesium covered surface altering the charged particle flux balance. In the present case, this affects the complex interplay between the potentials of the sample, the plasma and the meshed grid. Together with changes in the potentials, the Balmer emission decreases by up to 15 % during caesium evaporation. This effect has also been observed by [Fri13] where it is explained as a consequence of caesium induced H gettering. Although the correlation between the atomic hydrogen density and the negative ion density is linear (destruction via (non)associative detachment), the measured reduction of 15 % in the atomic hydrogen density is negligible compared to the surface induced enhancement of the negative ion density.

It has to be mentioned that in negative ion sources the application of caesium is typically correlated with an enhancement of the negative ion density of up to a factor of 10 [WSF16]. The deviation to the present observations is explained by the different fluxes of atomic and ionic hydrogen particles bombarding the converter surface.

At HOMER the positive ion flux is in the order of $1\times10^{20}\,\mathrm{m^{-2}s^{-1}}$. This flux is calculated on basis of an effective electron temperature determined via equation (3.9) and an effective positive ion mass of 2 u. For the calculation of the neutral hydrogen atom flux both ensembles of hydrogen atoms, i.e. the hot and the cold

ensembles have to be taken into account. The combined neutral atom flux is thereby assessable via the ratios of the corresponding formation rates and the thermal velocities of the both ensembles. Thus, at HOMER a neutral hydrogen atom flux of about $5\times10^{21}\,\mathrm{m^{-2}s^{-1}}$ is given. The maximal conversion yield reported in [IKS92] and [LS92] is 20 % for positive ions and 25 % for neutral atoms depending on the actual surface work function and the energy of the impinging particles. According to this, the neutral atom flux at HOMER has a much higher relevance for producing a negative ion flux into the plasma than the positive ion flux. The estimated difference is up to a factor of 63. After [WGF09] and [WSM+12], the conversion of neutral atoms also is the dominant process for negative ion production in negative ion sources.

In the IPP prototype negative ion source the positive ion and neutral atom fluxes are about 0.7 to $7\times10^{20}\,\mathrm{m^{-2}s^{-1}}$ and 1 to $3\times10^{22}\,\mathrm{m^{-2}s^{-1}}$, respectively, [Wim14]. Thus, at HOMER the positive ion flux is up to a factor of seven and the neutral atom flux up to a factor of six lower than at BATMAN. Consequently a lower enhancement of the measured $n_{\mathrm{H^-}}$ is expected at HOMER when caesium is applied.

It has to be noted that at HOMER the lower enhancement of the measured $n_{\mathrm{H^-}}$ may also be correlated with a potentially present space charge limitation (see section 3.4) that masks the actual negative ion surface formation induced by the application of caesium. However, regarding the investigations on caesium-free alternatives this effect is of minor relevance as the effect of caesiation is measured for giving a benchmark value at present experimental conditions at HOMER and correspondingly apply for all other investigated materials.

7.2 Reproducibility Regarding Exchange of Sample

For monitoring the long term evolution and to check a possible material induced contamination of the setup during the performed investigations, measurements with the stainless steel reference sample were conducted at constant external conditions after distinct measurement campaigns. In figure 7.12 the corresponding positive and negative ion densities are plotted for 0.3 Pa H_2 and 300 W discharge power in a distance of 2.5 cm to the sample.
A mean positive ion density of $1.28\times10^{16}\,\mathrm{m^{-3}}$ with a standard deviation of less

than 4 % and a mean negative ion density of $9.43 \times 10^{14}\,\mathrm{m}^{-3}$ with about 12.2 % of standard deviation was determined. The measured deviation is smaller than the corresponding error margins for the positive ion density determination of about 11 % and for n_{H^-} of 21 %. Thus, this virtually constant long term evolution shows no indications for any possible contamination of the experimental setup and confirms the reproducibility of the negative ion density determination and furthermore, the applicability of the stainless steel sample for determining reference values.

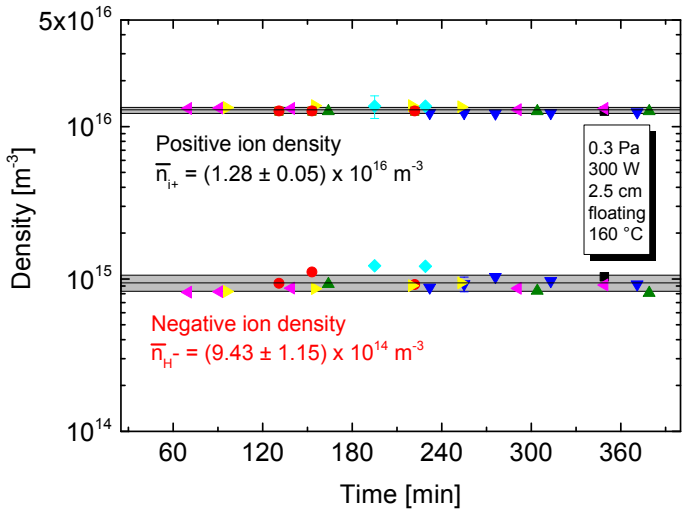

Figure 7.12: *Reproducibility of the positive and negative ion densities measured with the stainless steel reference installed. Measurements were performed over one year of measurement after distinct campaigns (indicated by the different symbols) on caesium-free materials.*

8 Negative Ion Formation at Caesium-Free Materials

Following the discussions in chapter 4.1.2 three types of materials are investigated for their effect on the negative ion formation, i.e. for being caesium-free alternatives:

- materials with inherent low work function (H^- surface formation),
- diamond materials (direct H^- surface formation), and
- refractory metals (indirectly enhancing the volume formation).

For the investigations, each campaign is compared to respective measurements performed with a stainless steel reference sample. Furthermore, the influence of the investigated surfaces is assessed using 0-dimensional modelling of the H^- volume processes.
In order to detect any plasma induced erosion or ablation of the investigated sample materials, the sample weight is measured before and after plasma exposure and the plasma emission is monitored with the survey spectrometer to see impurities.

8.1 Investigations on Low Work Function Materials

Materials with inherently low work function, namely lanthanum hexaboride (LaB_6) and a molybdenum sample doped with 0.7 % lanthanum (MoLa) are investigated for their effect on the negative ion density.
The LaB_6 sample has a polycrystalline structure and is manufactured by press sintering. It has a sample size of 3x3 cm^2 and is purchased from the commercial

distributor Sindlhauser [Sin14]. For this sample material a work function between 2.7 and 3 eV is expected according to [SKO+79, KS97] and [UWG06]. Also the MoLa sample has a polycrystalline structure and is produced via press sintering. A work function of about 2.6 eV is expected according to [YNX+04] for the MoLa sample which has a sample size of $8.5\times6\,\mathrm{cm}^2$ and is purchased from the commercial distributor Plansee [Pla01].

Both samples were cleaned with purified water, acetone and isopropyl alcohol. Additionally to that, the MoLa sample was mechanically polished prior to the described procedure.
For none of the performed investigations indications for plasma induced material erosion was measurable by emission nor by weight loss measurements, showing the resistibility of LaB_6 and MoLa in the investigated scenarios.

In order to reduce residual impurities on the investigated surfaces, i.e. to achieve a low work function, the samples are heated in vacuum up to a temperature[1] of 450° C for two hours. Measurements are conducted one hour after starting the discharge at 0.3 Pa hydrogen gas pressure and 300 W discharge power like in case of the stainless steel measurements.

8.1.1 Sample Bias Variations

The amount of negative ions at a surface depends on the flux of incoming particles. The low work function materials are consequently investigated for a sample bias variation, since thereby a direct influence on the positive ion flux, on the one hand and on the dwelling time of surface produced negative ions on the other hand is possible. Additionally, by increasing the positive ion flux a potentially present space charge limitation may be suppressed and so a further insight into the negative ion formation capability given.

In figure 8.1 the negative ion density measured as a function of sample bias between -30 to +20 V is shown for MoLa, LaB_6 and the stainless steel reference sample. The measurements are performed with a relative distance between the

[1] It has to be noted that typically low work function materials are heated to significantly higher temperatures ($\gtrsim$1000 K) for achieving lowest possible work functions. However, the applied temperatures within this work are expected to be of higher relevance from an engineering point of view in the context of future NNBI systems.

installed samples and the stationary Langmuir probe of 2.5 cm.
Compared to stainless steel an increased n_{H^-} is measured over the whole investigated range when MoLa or LaB_6 are installed. The increase is most pronounced in the range between -10 to +20 V being at least 15 % in case of MoLa and 25 % in case of LaB_6. For MoLa n_{H^-} is maximal at -5 V (=$1.4\times10^{15}\,m^{-3}$) and increased by 60 % compared to stainless steel. For LaB_6, n_{H^-} is maximal at +20 V and maximally increased by 42 %, at -5 V. For negative biases of -30 and -20 V, the difference between the measured H^- density for the low work function materials and stainless steel diminishes and is comparable within the error margins.
Independent of the material, the negative ion density is reduced when a negative bias below -5 V is applied. With increasing bias between -5 to +20 V, i.e. in the moderate negative and positive bias range, n_{H^-} increases monotonously in case of the stainless steel reference, is within the error margin virtually constant for LaB_6 and for MoLa.

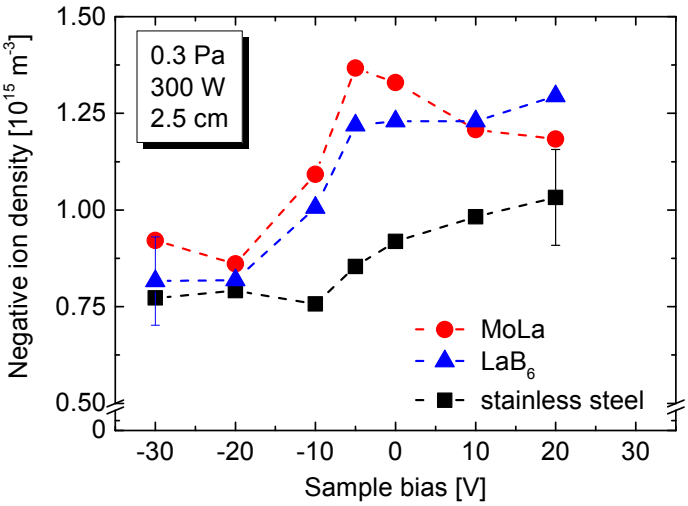

Figure 8.1: *Negative ion density as a function of applied sample bias for stainless steel (T_{smpl} = 160° C) and the low work function materials MoLa and LaB_6 (T_{smpl} = 450° C).*

It has to be noted that in the present setup a modification of the sample bias not only affects the fluxes of charged particles in front of the sample but also the potentials of the plasma and the meshed grid. Thus, the complex interplay of global particle fluxes is affected. The principle influence of a sample bias variation on the plasma itself is characterized by using the stainless steel reference sample.

The potential difference between the plasma and the sample allow for assessing the energy of impinging charged particles. The evolution of the plasma and floating potential which are determined via the Langmuir probe relative to the grounded vessel walls as well as of the meshed grid is shown as a function of sample bias variation in figure 8.2 (a) exemplarily for the stainless steel reference sample. For the low work function materials, an almost equal evolution is observed. As can be seen in figure 8.2 (a), the measured potentials shift accordingly with the sample potential, i.e. with increasing sample potential, the measured potentials increase but show a lower dynamic in the negative bias range.
In figure 8.2 (b), the potential difference ΔU between the plasma and the sample potential for stainless steel and the low work function materials is depicted. Assuming a collisionless sheath, a maximal positive ion energy of up to 10 eV is achievable for the dominant positive ion species H_2^+ in the investigated range when the sample is most negatively biased. In the moderate negative and positive bias range, the positive ion energy is nearly independent of sample bias variations: the positive ion energy in this range is constantly about 0.9 eV.

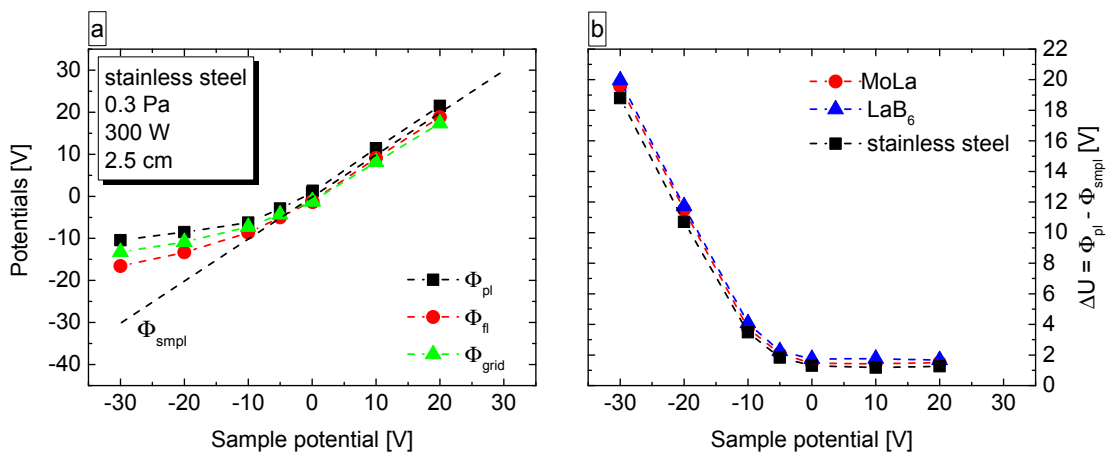

Figure 8.2: *Evolution of potentials and potential differences for sample bias variations: (a) plasma and floating potentials measured with the Langmuir probe and potential of the meshed grid for stainless steel. (b) Potential difference between plasma and sample potential for stainless steel and the low work function materials.*

Additionally to the shown effect of sample bias variations on the negative ion density and the potentials, a change of measured plasma parameters is observed mainly for $n_{\mathrm{H}}/n_{\mathrm{H}_2}$ and the mean electron energy, i.e. the EEDF. Other plasma parameters like the diagnostically determined $T_{\mathrm{vib}}^{\mathrm{OES}}$ as well as the positive ion density are only minor influenced by sample bias variations. For all materials, a $T_{\mathrm{vib}}^{\mathrm{OES}}$

of about (3500±250) K and a positive ion density of about $(1.3\pm0.1)\times10^{16}\,\mathrm{m}^{-3}$ are measured.
It has to be noted that in case of low work function materials, a changing $n_\mathrm{H}/n_{\mathrm{H}_2}$, i.e. a changing n_H, not only affects the H^- destruction via atom collisions but also negative ion surface formation. A changed mean electron energy influences the formation via the dissociative attachment process as well as the destruction via electron detachment.

In figure 8.3 the atomic to molecular density ratio is shown as a function of applied sample bias. Like in section 7.1.1, the Balmer emission lines were characterised by a double-Gaussian peak and depicted data are deduced according to the emissivity of the narrow H_γ peak.
For stainless steel and LaB_6 $n_\mathrm{H}/n_{\mathrm{H}_2}$ ranges between 7.3 and 9.5 %, whereas in case of MoLa the density ratio is slightly increased (range 8.7 to 9.7 %). As depicted in figure 8.3, these variations are almost within the error margins and independent of the sample, the atomic to molecular hydrogen density ratio is only minor effected by sample bias variations. Within the error margins, comparable atomic hydrogen and gas temperatures of 500 K are measured, virtually unaffected by sample bias variations. Hence, the atomic hydrogen fluxes vary correspondingly with $n_\mathrm{H}/n_{\mathrm{H}_2}$: Overall the atomic hydrogen flux varies between $1.6\times10^{21}\,\mathrm{m}^{-2}\mathrm{s}^{-1}$ and $2.2\times10^{21}\,\mathrm{m}^{-2}\mathrm{s}^{-1}$.
The effect of sample bias on the EEPF evolution is shown exemplarily for stainless steel in figure 8.4 (a) and the corresponding $T_{\mathrm{e},1}$ and $T_{\mathrm{e},2}$ for stainless steel, MoLa and LaB_6 are depicted in figure 8.4 (b).
As can be seen, the electron energy distribution has a Bi-Maxwellian character that is clearly influenced by sample bias variations. Comparable EEDFs are measured for stainless steel and the low work function materials. The corresponding electron temperatures behave equably, independent of the installed sample material. With increasing bias $T_{\mathrm{e},1}$ decreases from about 1.8 eV at -30 V down to 0.5 eV at 0 V and is virtually constant for positive biases. $T_{\mathrm{e},2}$ is decreasing over the whole investigated bias range from 7.0 eV at -30 V down to 4.5 eV at +20 V. Furthermore, the weighting factor β is nearly constant within the error margins at about 10 % in the positive bias range but increases with increasing negative bias up to 20 %. This evolution is consistent with an increment of electron repulsion from the surface which is correlated with the increasing negative sample bias.

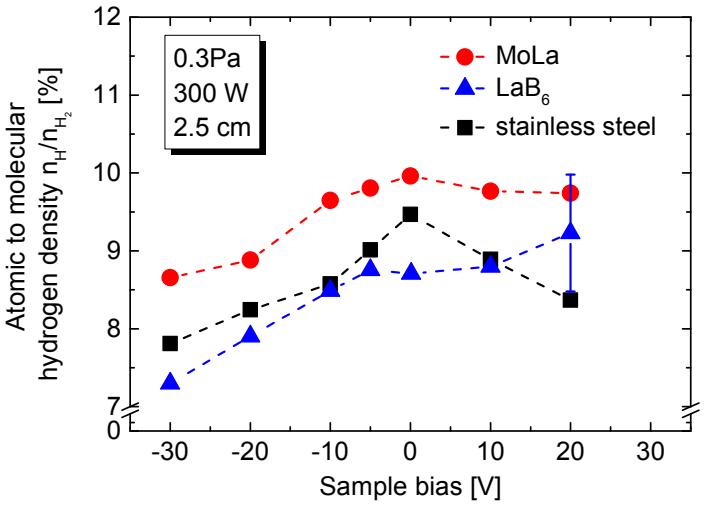

Figure 8.3: *Atomic to molecular density ratio as a function of applied sample bias for stainless steel ($T_{\mathrm{smpl}} = 160\,^{\circ}C$) and the low work function materials MoLa and LaB_6 ($T_{\mathrm{smpl}} = 450\,^{\circ}C$).*

In order to assess the present negative ion surface formation at the low work function materials, the volume processes are modelled based on the measured plasma parameters.

The significant influence of the diagnostically not accessible population of vibrationally highly excited H_2 molecules on the absolute density n_{H^-} is again taken into account in *Yacora* H^- like in section 7.1.1 via a variation of the temperature $T_{\mathrm{vib},2}$. It is assumed that all three investigated surfaces have a comparable effect on the distribution of highly excited $H_2(X, \nu \geq 3)$ states[2]. Regarding this, two approaches for implementing the vibrational temperature $T_{\mathrm{vib},2}$ are used for modelling:

- In a first approach $T_{\mathrm{vib},2}$ was deduced by fitting modelled data to stainless steel measurement at 0 V and keeping this free parameter fixed for other biases and materials.

- In the second approach, $T_{\mathrm{vib},2}$ was adapted to fit modelled n_{H^-} to measured stainless steel data for each sample bias and applying the deduced temperatures also for the low work function materials.

[2]The vibrational population can be modified by particle reformation at the surface and thus it might be sensitive on the surface material (see chapter 4.1.2). However, for both materials no dedicated data on this reformation process are available in literature.

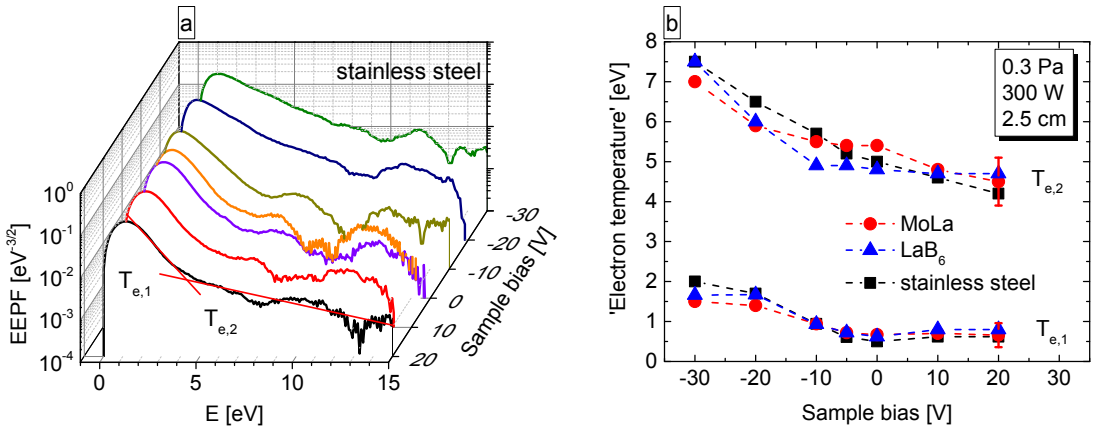

Figure 8.4: *Evolution of the mean electron energy as a function of sample bias variations: (a) Dependence of measured EEPF versus sample bias of the stainless steel sample. (b) 'Electron temperatures'* $T_{e,1}$ *and* $T_{e,2}$ *of the Bi-Maxwellian EEDF in dependence of applied sample bias for stainless steel* (T_{smpl} = *160°C) and the low work function materials MoLa and* LaB_6 (T_{smpl} = *450°C).*

The first approach follows the idea that the vibrational distribution is mainly resulting from present conditions within the driver region, i.e. in the plasma volume above the meshed grid where it is assumed that sample bias variations have a negligible influence (tandem principle). In the second approach it is assumed that any potential influence of sample bias variations on $H_2(X, \nu \geq 3)$ are at least transferable from stainless steel measurements to investigations with the low work function materials.

In figure 8.5 the measured n_{H^-} is compared to the modelled negative ion densities for all three materials. As can be seen, in case of stainless steel, modelled n_{H^-} well reproduce the measured densities in the moderate negative and positive bias range using a fixed $T_{vib,2}$ of (8300±210) K. In this bias range the evolution of the negative ion density is mainly given by changes in the dissociative attachment rate. However, in the negative bias range, a significant deviation between modelled and measured negative ion densities is present. The strong decrease of the modelled n_{H^-} is a consequence of the changing EEDF leading mainly to a lowered dissociative attachment rate. Furthermore, the H^- destruction via electron detachment increases according to the increasing mean electron energy in the negative bias range. While in the moderate negative and positive bias range, H^- are dominantly destroyed via atomic collisions with a relative share of all destruction channels of minimal 66 %, negative ions are predominantly destroyed by electron

detachment in the bias range between -30 and -20 V reaching a relative share of almost 50 %. The pronounced deviation between modelled and measured negative densities implies that in this bias range the population of vibrationally highly excited states is strongly affected. This can be taken into account in *Yacora* H^- via $T_{\mathrm{vib},2}$ and the model well reproduces the measured stainless steel data when vibrational temperatures are increased up to 10600 K at -30 V (see figure 8.6).

This analyses clearly shows that for the both low work function materials higher negative ion densities are given which are not resulting from increased volume formation. Independent of the approach and in contrast to stainless steel, modelling based on measured plasma parameters results for the both low work function materials in negative ion densities that are lower than measured ones over the whole investigated bias range.
This discrepancy implies that in case of the low work function materials an additional source for negative ions, i.e. H^- surface production is present. It has to be furthermore noted that in case of MoLa and LaB_6 the comparison of modelled and measured n_{H^-} indicates an even more pronounced surface induced n_{H^-} enhancement is given than the comparison of measurements with the stainless steel measurement would imply.

For the low work function materials, the deviation between measurement and modelling is most pronounced in the positive bias range and diminishes at least for the second modelling approach in the negative bias range. As shown in figure 8.3, $n_{\mathrm{H}}/n_{\mathrm{H}_2}$ is decreasing for decreasing bias and thus also the atomic hydrogen flux onto the sample surface. As a higher atomic hydrogen flux is expected to correlate with an increased negative ion surface formation rate, this may be interpreted as an indication for an increasing H^- surface formation at higher biases.
However, regarding the flux of positive ions to the surface, no enhancement is measured for increasing the positive ion flux by increasing the negative sample bias. Also no increment of the H^- yield by increasing the energy of the impinging positive ions is observed which was reported by [IKS92] for a caesiated molybdenum surface in a comparable energy range. This confirms a minor relevance of the positive ion flux and energy of impinging positive ions for the H^- surface production in case of MoLa and LaB_6 which would be in line with the expected higher relevance of negative ion surface formation from H seen in case of a caesiated surface (see discussion in section 7.1.2). It has to be furthermore noted that

no indications for a space charge limitation are observed as in the negative bias range no increment of the negative ion density is measured.

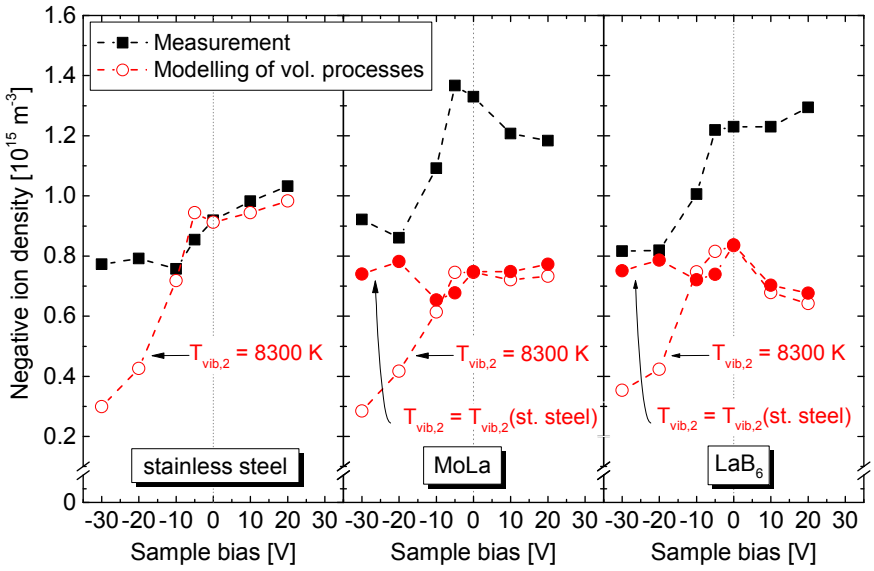

Figure 8.5: *Modelled n_{H^-} as a consequence of changed volume processes in comparison with measured n_{H^-} as a function of sample bias. Modelling is based on measured input parameters assuming $T_{\mathrm{vib},2}$ deduced from adapting modelled data to stainless steel measurements after two different approaches (see text for details).*

8.1.2 Distance Scans

According to the estimation of the mean free path of surface produced negative ions (see section 7.1.2), a high probability is given that the applied diagnostic system at HOMER is suited to detect all surface produced H^-. However, the negative ion transport may be influenced since surface produced negative ions can lead to a significant modification of the sheath topology. Thus, the evolution of n_{H^-} is investigated as a function of distance comparing low work function materials and the stainless steel reference sample. This is done by variation of the sample holder's relative position, i.e. the distance between the station-

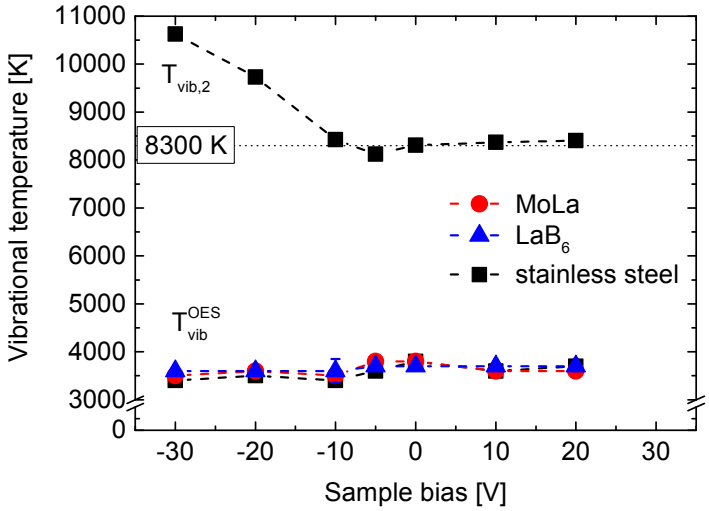

Figure 8.6: *Evolution of the vibrational temperature as determined via OES for stainless steel and the low work function materials and of $T_{\mathrm{vib},2}$, fixed at 8300 K (dotted line, first approach, see details in text) and for matching for stainless steel modelled n_{H^-} to measured data (second approach, , see details in text).*

ary Langmuir probe and the sample surface. For these investigations no sample bias is applied, i.e. the samples are on floating potential and measurements are performed at 0.3 Pa hydrogen pressure and 300 W discharge power. According to measurements regarding the effect of sample bias variations, the low work function materials are kept at a temperature of up to 450 °C during the present measurement campaigns.

In figure 8.7 the negative ion densities are shown, measured as a function of distance for the low work function materials as well as for the stainless steel reference sample. Increasing the relative distance between the sample surface and the Langmuir probe from 1.5 to 4.5 cm results in an increment of n_{H^-} for all materials. Thereby, higher negative ion densities are measured with the low work function materials than with the stainless steel reference sample installed. The negative ion density increases from $7.1\times10^{14}\,\mathrm{m}^{-3}$ up to $1.6\times10^{15}\,\mathrm{m}^{-3}$ and $1.5\times10^{15}\,\mathrm{m}^{-3}$ for MoLa and LaB_6 respectively, whereas for the stainless steel reference the negative ion density increases from $6.2\times10^{14}\,\mathrm{m}^{-3}$ to $1.4\times10^{15}\,\mathrm{m}^{-3}$. As expected, no indications for a higher concentration of surface produced H^- is observed which is in line with the mean free path of several meters. A variation of the relative distance rather affects the bulk plasma in front of the probe:

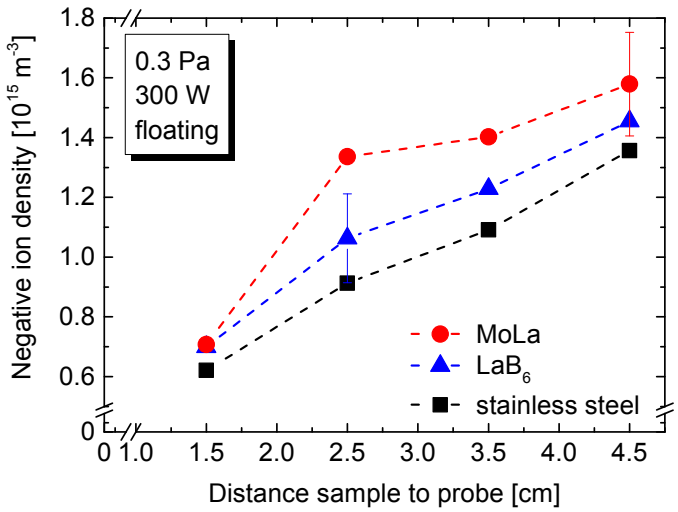

Figure 8.7: *Dependence of n_{H^-} for MoLa, LaB_6 (T_{smpl} = 450° C) and stainless steel (T_{smpl} = 160° C) on a distance variation of the sample surface relative to the stationary Langmuir probe.*

While variations of the relative distance between the sample surface and the Langmuir probe mainly affect the absolute negative and positive ion densities, virtually no changes beyond the error margins are measured in the corresponding EEDFs, $n_{\mathrm{H}}/n_{\mathrm{H}_2}$ ratios and temperatures. The Bi-Maxwellian EEDFs are characterised by $T_{\mathrm{e},1}$ of about 0.6 eV, $T_{\mathrm{e},2}$ of 5.1 eV and $\beta \approx 10\,\%$. An atomic to molecular density ratio of about 9.5 % is present and $T_{\mathrm{gas}} \approx T_{\mathrm{H}}$ is 500° C whereas $T_{\mathrm{vib},1}$ is about 3700 K. For all three materials the positive ion density is virtually identical and increases linearly with increasing sample distance from $1.2\times10^{16}\,\mathrm{m}^{-3}$ to $1.6\times10^{16}\,\mathrm{m}^{-3}$.

For modelling the H^- related volume processes the approaches for $T_{\mathrm{vib},2}$ described in section 8.1.1 are used, i.e. the second vibrational temperature is deduced by adapting modelled data to measurements performed with stainless steel. In figure 8.8, measured and modelled H^- densities are depicted as a function of relative sample distance for stainless steel, MoLa and LaB_6.

In the first approach, $T_{\mathrm{vib},2}$ is determined by adapting the modelled n_{H^-} to stainless steel data, measured at 2.5 cm distance and keeping the deduced value of (8600±220) K fixed for other distances and materials (open symbols). The differing evolution of measured and modelled negative ion densities for stainless steel indicates a pronounced dependence of the vibrational distribution from the rela-

tive position of the sample since all other, measured plasma parameters are taken into account. Thus, $T_{\mathrm{vib},2}$ is adapted in a second approach to stainless steel measurements for each distance separately. The measured negative ion densities for stainless steel are reproduced by the model using a monotonously increasing $T_{\mathrm{vib},2}$ of 7900 K at 1.5 cm to $\approx$ 9000 K at 4.5 cm which correlates with a decrement of the depopulating character of an interaction between vibrationally highly excited H_2 and the sample surface.

Modelled negative ion densities for the low work function materials based on correspondingly measured input data are shown in figure 8.8. For a fixed $T_{\mathrm{vib},2}$ of 8600 K lower n_{H^-} are resulting than have been measured for distances greater than 1.5 cm and generally the measured trend of $n_{\mathrm{H}^-}$is not reproduced. In contrast, within the accuracy of the model, a comparable relative evolution of measured and modelled negative ions is given for the second approach for $T_{\mathrm{vib},2}$. However, modelled volume processes again result in negative ion densities that are lower than the measured densities over the whole investigated range. This confirms again the presence of an additional source for negative ions which is constantly increasing the negative ion density independent of distance.

8.1.3 Isotopic Differences on H^-/D^- using MoLa

Future NNBI systems will operate in hydrogen as well as in deuterium. Among caesium-free low work function materials, the highest H^- densities have been measured with MoLa. Consequently, the effect of this material on the negative ion density is further investigated in deuterium.
In figure 8.9 the negative ion density is shown measured as a function of sample bias in H_2 and D_2 with the MoLa sample installed. In both campaigns the sample temperature is constantly at 450° C. For comparison also n_{H^-} measured in H_2 with the stainless steel reference sample is depicted, too.
Shown data are measured at identical external parameters, i.e. in a relative distance of 2.5 cm to the stationary Langmuir probe at 0.3 Pa gas pressure and 300 W discharge power.

In accordance with the previously described results on H_2, higher negative ion densities are measured in the moderate negative and positive bias range in the presence of a MoLa sample compared to the stainless steel sample. A comparable

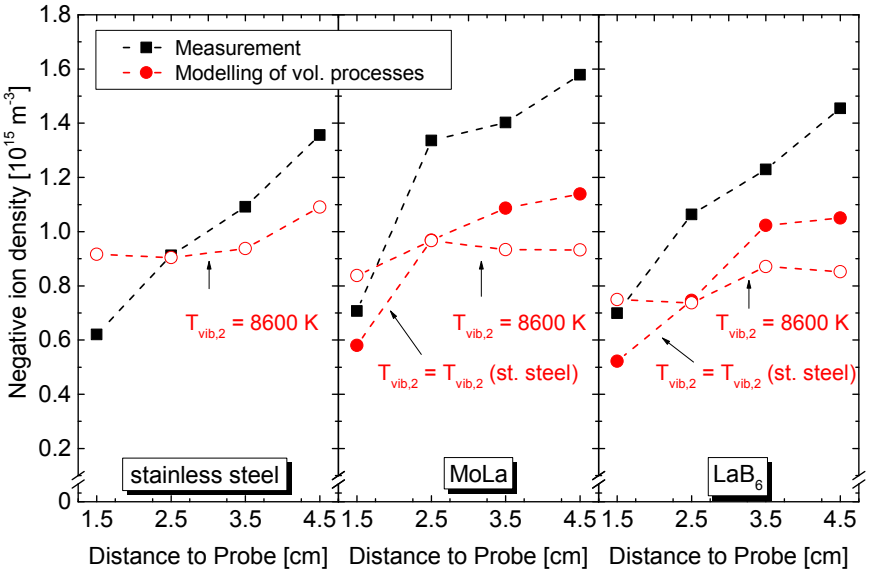

Figure 8.8: *Modelled n_{H^-} as a consequence of changed volume processes in comparison with measured n_{H^-} as a function of relative distance between sample surface and fixed Langmuir probe. Modelling is based on measured input parameters assuming $T_{\mathrm{vib},2}$ deduced from adapting modelled data to stainless steel measurements after two different approaches (see text for details).*

evolution of the negative ion density is given for H_2 and D_2, i.e. an increasing negative ion density with increasing bias, showing the highest dynamic in the bias range between -20 and -5 V. Applying a negative bias results in both cases within the error margins in virtually the same negative ion density of about $8.5\times10^{14}\,\mathrm{m}^{-3}$.

It has to be noted that the interpretation of the measured negative ion densities by deducing the volume processes via the 0-dimensional model *Yacora* H^- is not possible in case of deuterium due to the limited availability of corresponding cross section data. However, based on the assumption that changes in plasma parameters comparably affect negative ion related volume processes in D_2 as in H_2, a qualitative comparison of measured plasma parameters involved in these volume processes can be done.

In figure 8.10 the positive ion density as well as the 'electron temperatures' $T_{\mathrm{e},1}$ and $T_{\mathrm{e},2}$ describing the Bi-Maxwellian EEDF are plotted as a function of sample bias for MoLa in D_2 and H_2.

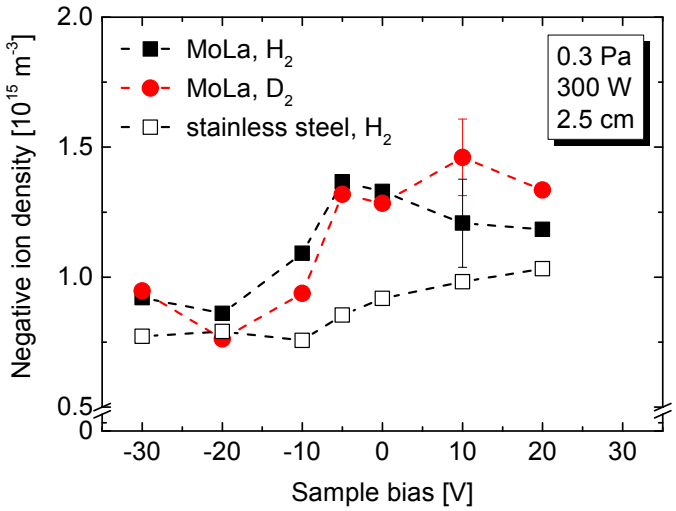

Figure 8.9: *Negative ion density as a function of applied sample bias for the low work function material MoLa measured in H_2 and D_2 (T_{smpl} = 450° C). For comparison data measured with the stainless steel reference in H_2 are depicted.*

For the positive ion density evaluation in D_2, the OML theory (applied for H_2) is inappropriate and the BRL theory applies (see chapter 5.2). As can be seen, a significant dependence on the isotope is present. Over the whole investigated range an increased positive ion density is measured in D_2 compared to H_2. In deuterium the positive ion density ranges between $1.8\times10^{16}\,\mathrm{m}^{-3}$ and $2.4\times10^{16}\,\mathrm{m}^{-3}$, thus it is up to 73 % increased compared to H_2. Furthermore, a more pronounced influence on sample bias variations is present in deuterium. Due to quasi-neutrality, the higher positive ion density together with the virtually equal negative ion density, correlates with a higher electron density in deuterium at comparable external parameters.

It has to be noted that on the one hand it is known that positive ion densities derived via BRL typically are higher than ones derived via OML (see section 5.2). However, on the other hand increased electron densities have also been measured in deuterium at a slightly modified version of HOMER, reported by [Die10] using among others microwave interferometry. It was discussed that this difference results at HOMER from a more efficient coupling of the injected microwave power into a deuterium plasma.

Independently of the gas type, a Bi-Maxwellian EEDF is present over the whole investigated bias range. Furthermore, the mean electron energy decreases with

increasing bias for both gases, i.e. a lower $T_{e,1}$ and $T_{e,2}$ is measured in the positive bias range than in the negative range. However, in case of deuterium, a higher mean electron energy is present independent of the applied sample bias: While virtually equal $T_{e,1}$ are measured for deuterium and hydrogen being up to 1.8 eV in the negative range and 0.7 eV in the positive bias range, $T_{e,2}$ is between 8 and 6 eV for deuterium, i.e. is increased between 0.5 and 2.3 eV compared to H_2 exceeding the error margins. This increase is most pronounced in the positive bias range. Also by [Die10] differences in the EEDF depending on the isotope have been observed.

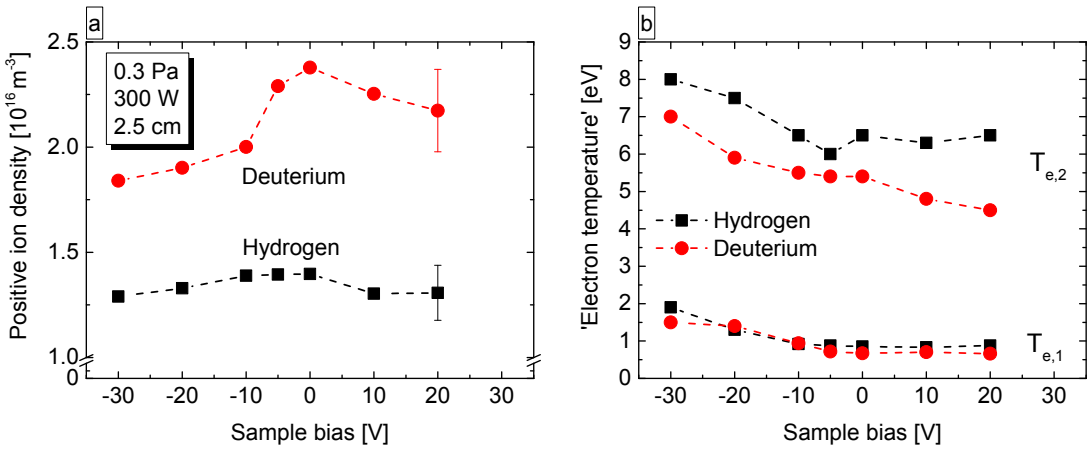

Figure 8.10: *(a) Positive ion density and (b) 'electron temperatures' for MoLa in H_2 and D_2 as a function of sample bias.*

In figure 8.11 the atomic to molecular density ratio as well as the gas temperature and the diagnostically accessible vibrational temperature $T_{vib,1} = T_{vib}^{OES}$ are plotted as a function of sample bias for MoLa in D_2 and H_2: a clear isotope effect is given for the density ratio and the gas temperature. Like in hydrogen, the emission line profile of the Balmer lines in D_2 are characterised by the superposition of two Gaussian profiles. The atomic to molecular density ratio is accordingly derived taking the narrow peak of the D_γ emission line into account. In hydrogen the atomic to molecular density ratio is between 8.7 and 10 % whereas it is between 17.9 and 25.8 % in deuterium. Furthermore, it shows a higher sensitivity on sample bias variations in deuterium than in hydrogen. The increased atomic to molecular density ratio in deuterium is in line with measurements performed by [Die10, Fri13] and [FFF+06]. It is a consequence of the higher cross sections for electron induced dissociative excitation [CJL+01] as well as of the higher n_e and

mean electron energy present in case of deuterium. The gas temperature measured in deuterium is lower by about 60 K compared to the hydrogen discharge in accordance with results reported by [Die10] and [Fri13]. Regarding the population of the diagnostically accessible vibrational states (i.e. $\nu \leq 3$), comparable vibrational temperatures $T_{\mathrm{vib},1}$ of (3500±250) K are measured for both isotopes within the error margins, not showing a pronounced dependence on sample bias variations.

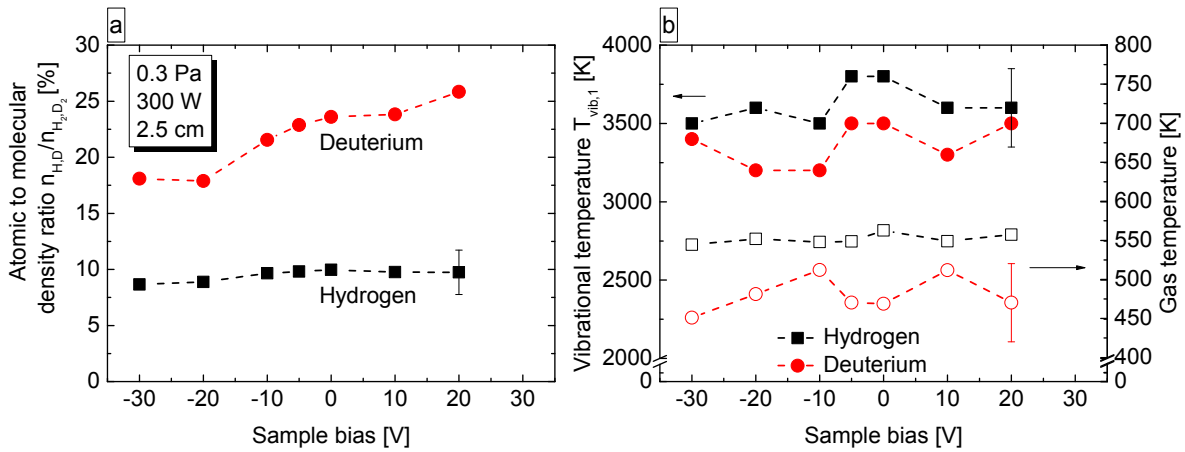

Figure 8.11: *(a) Atomic to molecular density ratio, (b) measured vibrational temperature $T_{\mathrm{vib},1}$ and gas temperature for MoLa in H_2 and D_2 as a function of sample bias.*

Assuming a comparable effect of these plasma parameters on the negative ion related volume processes in D_2 as in H_2, an overall increased dissociative attachment rate is given in deuterium, balanced by an overall increased volume destruction: The increased volume production is caused by the higher electron density present in deuterium. A discussion of the influence of a changed EEDF is however not possible due to the missing cross section data for D_2. As described, modelling of H^- related volume processes revealed that for hydrogen the evolution of the negative ion density, mainly given by changes in the dissociative attachment rate which is balanced in the positive bias range dominantly by destruction via atomic collisions and by electron detachment for the most negative biases. As the atomic particle density is even more increased in deuterium, a comparable relevancy of the present negative ion destruction mechanisms is expected for deuterium. Furthermore, regarding the absolute destruction rates, the increased atomic deuterium density and the higher electron density measured in deuterium results in an overall increased destruction of negative ions independent

of the applied sample bias. Electron detachment is even more enhanced due to the higher mean electron energy in deuterium.

The described differences in the positive ion and atomic neutral particle densities are in turn directly correlated with the negative ion surface production, which is depending on the impinging particle fluxes. These fluxes differ in hydrogen and deuterium not only due to the different particle densities but also the masses and temperatures. In contrast to the atomic temperature determination in hydrogen via the Doppler broadening of the Balmer emission line, the temperature evaluation in case of D_2 is not possible due to the spectral resolution of the diagnostic system. Therefore, the atomic deuterium flux is calculated on basis of the determined gas temperatures shown in figure 8.11, assuming a comparable equality of measured gas and atomic temperatures as in case of H_2.
Despite the higher mass of deuterium, the atomic particle flux is overall increased due to the measured increased n_{D}. In deuterium an atomic particle flux between $3.9\times10^{21}\,\mathrm{m^{-2}s^{-1}}$ in the negative bias range and $5.3\times10^{21}\,\mathrm{m^{-2}s^{-1}}$ for positive biases is determined. For comparison, a maximal atomic particle flux of $2.1\times10^{21}\,\mathrm{m^{-2}s^{-1}}$ is deduced in case of MoLa in H_2. Regarding the positive ion fluxes which are calculated on basis of an effective electron temperature determined via equation (3.9) and an effective positive ion mass of 2 u for H_2 and 4 u for D_2. For these corresponding Bohm fluxes no significant isotope effect is present within the error margins: Despite the differences in the positive ion densities, the Bohm flux is between 1.2 and $1.6\times10^{20}\,\mathrm{m^{-2}s^{-1}}$ in deuterium and between 0.9 and $1.6\times10^{20}\,\mathrm{m^{-2}s^{-1}}$ in hydrogen.

Regarding the negative ion related volume processes, indications for compensating tendencies for the volume production and destruction are found in deuterium. Thus, comparable negative ion densities like in case of hydrogen can be expected. According to the different atomic neutral fluxes, an increased negative ion surface formation is expected in case of deuterium. This difference is most pronounced in the positive bias range. Since within the error margins negative ion densities are only slightly rather than clearly increased in case of deuterium, this can be caused by a lower $T_{\mathrm{vib},2}$ being present in D_2 than in H_2 or generally that this effect is not exceeding the sensitivity of the diagnostic system for negative ions.

8.1.4 Conclusion

The effect of the low work function materials MoLa and LaB_6 on the negative ion density was studied as a function of sample bias and distance. Furthermore, for MoLa isotope differences were investigated.
Both materials have resulted in enhanced negative ion densities compared to stainless steel, without showing any signs of plasma induced erosion. Thus, they fulfil general requirements for being installed in negative ion sources for NNBI and are seen as potential suitable caesium-free alternative converter materials.
Compared to stainless steel, the presence of a MoLa sample in H_2 resulted in a maximal increment of the negative ion density by up to 60 % and in case of LaB_6 by up to 42 %. This enhancement is sensitive to the sample bias, i.e. it is most pronounced in the moderate negative and positive bias range, decreasing with decreasing bias. For a sample bias below -20 V virtually the same negative ion densities are measured as in case of the stainless steel reference sample. In contrast to a sensitivity on the sample bias, increased negative ion densities were measured when low work function materials have been installed independent of the relative distance.

It was discussed that this effect in not caused by changes of the H^- volume formation processes using *Yacora* H^-: The effects of changing plasma parameters on the volume processes were modelled, assuming a comparable distribution of the vibrationally highly excited H_2 states for the low work function materials as in case of stainless steel: For MoLa and LaB_6 lower negative ion densities are determined by the volume processes than have been measured. This is interpreted as the presence of an additional source for negative ions, i.e. H^- surface production. The observed correlation between the impinging atomic hydrogen flux and the measured n_{H^-} evolution in combination with the absence of a pronounced effect resulting from an increment of the positive ion flux implies that H^- surface formation at MoLa and LaB_6 is given mainly by atomic particle conversion.

Isotopic differences were studied for MoLa, also by variation of the applied sample bias. Over the whole investigated range virtually the same negative ion densities were observed within the error margins in H_2 and D_2.
A quantitative comparison via modelling of the volume processes is not possible for deuterium due to the limited availability of appropriate cross section data.

However, a comparison of measured plasma parameters under the assumption of a comparable dependence of negative ion related volume processes in deuterium like in case of hydrogen revealed that overall increased volume formation and destruction rates are present in deuterium. Hence, comparable negative ion densities coming from the correlated volume processes are expected in D_2 like in H_2. The observed increment of the atomic deuterium density, correlated with an increased atomic particle flux did not result in an expected enhancement of the amount of surface produced negative ions that exceeds the sensitivity of the diagnostic system. Only a slightly enhanced negative ion density is measured in case of deuterium which is however within the error margins.
For the application in negative ion sources for NNBI, the significantly higher positive ion densities, measured in D_2, at comparable negative ion densities have to be noted, which is linked to higher electron densities. This is generally related to a high amount of unwanted, co-extracted electrons, an effect that is typically also observed in negative ion sources comparing deuterium and hydrogen operation (see for instance [FSW14]).

It has to be furthermore mentioned that despite the observed enhancing effect of MoLa and LaB_6 at HOMER, the actual work function of these materials has not been accessible within the performed investigations. Since this crucial parameter for negative ion formation may be altered for higher particle fluxes present in negative ion sources, dedicated experiments regarding the impact of ion source plasma exposure and long-term stability are necessary in order to further examine their suitability for being converter surfaces.

8.2 Investigations with Diamond Materials

Within this work a variety of different none-doped and boron doped diamond samples have been investigated for their negative ion formation capability at ion source relevant parameters, since the underlying mechanism for negative ion formation at diamond is not known at present. Two non-doped diamond samples (in the following labelled diamond#1 and diamond#2) and three boron doped diamond (BDD) samples (in the following labelled BDD#1, BDD#2 and BDD#3) are investigated. Their characteristics are given in the following and additionally for a comprehensive view they are listed in table 8.1.

The first non-doped diamond sample (**diamond#1**) is a polycrystalline bulk diamond sample of 0.75 mm thickness and an average grain size of about 150 μm deposited at the University of Augsburg [Sch15] via MPACVD[3]. Investigations are performed using twelve diamond pieces sized between $0.5\times2\,\mathrm{cm}^2$ and $2\times2\,\mathrm{cm}^2$ and arranged in a mosaic pattern on the sample holder.

The second non-doped sample (**diamond#2**) has an epitaxial crystalline structure and a thickness of about 13 μm. The sample was deposited at the University of Augsburg [Sch15] also via MAPCVD on a $\langle 0\,0\,1\rangle$ oriented silicon substrate and comprised an average grain size of 2.5 μm. The sample size is $3\times2\,\mathrm{cm}^2$.

The first BDD sample (**BDD#1**) is a polycrystalline diamond layer deposited with a maximal thickness of 3 μm on a silicon waver at the LSPM laboratory [LF15] via PECVD[4] and was provided by [Gil15]. The sample has an estimated charge carrier density of $1.5\times10^{18}\,\mathrm{m}^{-3}$, an average grain size of 1.8 μm and a diameter of 5 cm.

The second BDD sample (**BDD#2**) is a polycrystalline diamond layer deposited via MPACVD on a molybdenum substrate at Heriott-Watt University [Her15] and was provided by [Cro13]. The boron doping level was measured by [Sar15] via RBS[5] to be $0.5\times10^{18}\,\mathrm{m}^{-3}$. The sample size was $8.5\times6\,\mathrm{cm}^2$.

The third BDD sample (**BDD#3**) is a polycrystalline diamond layer of 12 μm thickness deposited via HFCVD[6] on a niobium substrate and was purchased from the commercial supplier Diaccon [Dia13]. The boron doping level was measured by [Sar15] via RBS to be $0.1\times10^{18}\,\mathrm{m}^{-3}$. The average grain size was about 3 μm and the sample is $6.9\times2.9\,\mathrm{cm}^2$.

All samples have been cleaned with purified water and dried with nitrogen gas prior to installation in HOMER. Measurements are started one hour after starting the hydrogen discharge. It is therefore assumed that all samples are H covered

[3]Microwave plasma assisted chemical vapour deposition.
[4]Plasma enhanced chemical vapour deposition
[5]Rutherford backscattering spectrometry.
[6]Hot filament assisted chemical vapour deposition

Table 8.1: *Overview of investigated diamond materials.*

	diamond#1	**diamond#2**	**BDD#1**	**BDD#2**	**BDD#3**
Crystallinity	polycr.	epitaxial	polycr.	polycr.	polycr.
Sample Size [cm^2]	34	4	31.4	51	20
Thickness of diamond layer [μm]	7.5×10^2	13	3	not specified	12
Average grain size [μm]	150	2.5	1.8	not specified	3
Substrate material	-	Si $\langle 0\,0\,1 \rangle$	Si polycr.	Mo polycr.	Nb polycr.
Deposition method	MPACVD	MPACVD	PECVD	MPACVD	HFCVD
Boron Doping level [$10^{18}\,m^{-3}$]	0	0	1.5	0.5	0.1
Supplier	[Sch15]	[Sch15]	[Gil15, LF15]	[Cro13, Her15]	[Dia13]

due to the present hydrogen flux and consequently are expected to possess a negative electron affinity according to the results reported by [DKA+98, WZB+94], i.e. a beneficial constraint is fulfilled for negative ion surface formation.

For the investigations on the effect of diamond materials on the negative ion density, the focus is laid on variations of sample bias, temperature increment and in case of BDD additionally on sample bias variations at elevated temperature, i.e. with and without actively heating the BDD samples. Due to the low or absent electrical conductivity of the investigated diamond materials, the application of a sample bias is maintained by biasing the sample holder. Via this procedure, the electrical field induced over the diamond is modified. Even if the actual potential at the plasma facing surface is diagnostically not accessible, the sheath topology will be altered and thus, the labelling 'sample bias' is maintained, in order to illustrate the variation of the positive ion energy.

Presented measurements are performed at a relative distance of 2.5 cm to the stationary Langmuir probe at a hydrogen gas pressure of 0.3 Pa and 300 W discharge power. If not otherwise specified, the samples are not additionally heated and the sample temperature is below 160 °C.

Regarding the resistibility of the diamond materials against ion source relevant plasma conditions, the impact of plasma exposure is investigated by determining the sample weight before and after the different campaigns, monitoring the

plasma emission and analyses of the surface structure.

8.2.1 Sample Bias Variation for non-heated Diamond Materials

In figure 8.12 the negative ion density is depicted as a function of sample bias between -30 to +20 V for non-doped diamond (part (a)) and BDD samples (part (b)). Compared to stainless steel, none of the investigated diamond materials[7] results in a systematic enhancement of n_{H^-} beyond the error margins and virtually the same negative ion densities are measured. Furthermore, independent of the installed material sample, a comparable dependence on variation of sample bias is present, i.e. increasing n_{H^-} with increasing bias.

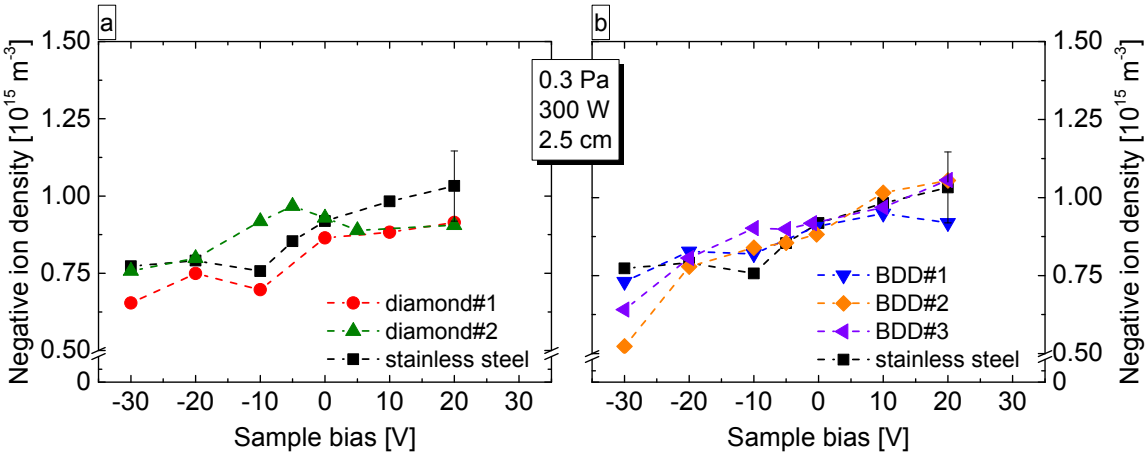

Figure 8.12: *Negative ion density as a function of sample bias for stainless steel, (a) non-doped diamond and (b) BDD. The sample temperatures are about* $T_{\mathrm{smpl}} \approx 160°\,C$.

The influence of sample bias variations on the charged particle flux can be assessed qualitatively via the evolution of the potentials and their differences. The sample bias variation from -30 to +20 V results in a comparable evolution of the plasma and floating potentials (meshed grid and Langmuir probe) for all diamond materials showing virtually the same dependency like in case of the stainless steel reference sample depicted in figure 8.2. Accordingly, a virtually constant potential difference between plasma and sample potential of 1.3 V is given for the bias range between -5 and +20 V. With increasing negative bias the potential difference significantly increases up to a maximal potential difference of 21 V at -30 V

[7] In section 8.2.3 it will be shown that despite a detected plasma induced surface erosion for all diamond samples a diamond layer is still present after plasma exposure.

sample bias.
Regarding the influence on the bulk plasma, virtually the same positive ion densities of about $1.3\times10^{16}\,\mathrm{m}^{-3}$ are given independent of the installed materials, showing a minor dependence of less than 14 % on sample bias variations. In contrast a pronounced influence of the presence of diamond and BDD samples on the mean electron temperature, the vibrational temperature and the atomic to molecular density ratio is observable. In figure 8.13, corresponding parameters are plotted as a function of sample bias for all diamond and BDD materials compared to stainless steel. Like for stainless steel, a Bi-Maxwellian EEDF is present for all materials independent of applied sample bias. A comparable evolution of both temperatures $T_{\mathrm{e},1}$ and $T_{\mathrm{e},2}$, characterising the EEDF, is given. As can be seen, $T_{\mathrm{e},1}$ decreases from about 1.5 to 0.8 eV with increasing bias. For $T_{\mathrm{e},2}$, stainless steel and the diamond materials differ slightly: While for stainless steel $T_{\mathrm{e},2}$ decreases monotonously with increasing bias over the whole investigated bias range, for diamond materials it decreases in the negative bias range, but slightly increases in the positive bias range. At most negative bias, $T_{\mathrm{e},2}$ is about 8 eV for all materials and at +20V it is about 4.2 eV for stainless steel and 5.8 eV in case of diamond materials.
The weighting factor β evolves similar to the case of bias variations with the stainless steel reference sample with absolute values of 10 to 20 %.
Regarding the vibrational distribution, compared to stainless steel, a systematic increment of the vibrational temperature $T_{\mathrm{vib}}^{\mathrm{OES}}$ is measured when diamond samples are installed. As can be seen in figure 8.13 (b), the diagnostically accessible vibrational temperature $T_{\mathrm{vib}}^{\mathrm{OES}}$ in the presence of diamond materials is between 4000 and 4500 K, i.e. increased by about 500 K compared to stainless steel.
The most pronounced impact of diamond materials is given on the atomic to molecular density ratio. Compared to stainless steel the atomic to molecular hydrogen density is in investigations performed with diamond materials significantly reduced by up to 70 % over the whole investigated bias range.
Like for stainless steel measurements, the determined atomic hydrogen temperatures are within the error margins comparable with the gas temperature ($T_{\mathrm{gas}} \approx$ 500 K) for all diamond materials. According to the lower atomic to molecular density ratios measured with diamond materials, compared to stainless steel a reduced atomic hydrogen flux of 0.9 to $1.4\times10^{21}\,\mathrm{m}^{-2}\mathrm{s}^{-1}$ is determined. For comparison, in case of stainless steel, the atomic hydrogen flux ranges between 2.4 and $2.8\times10^{21}\,\mathrm{m}^{-2}\mathrm{s}^{-1}$.

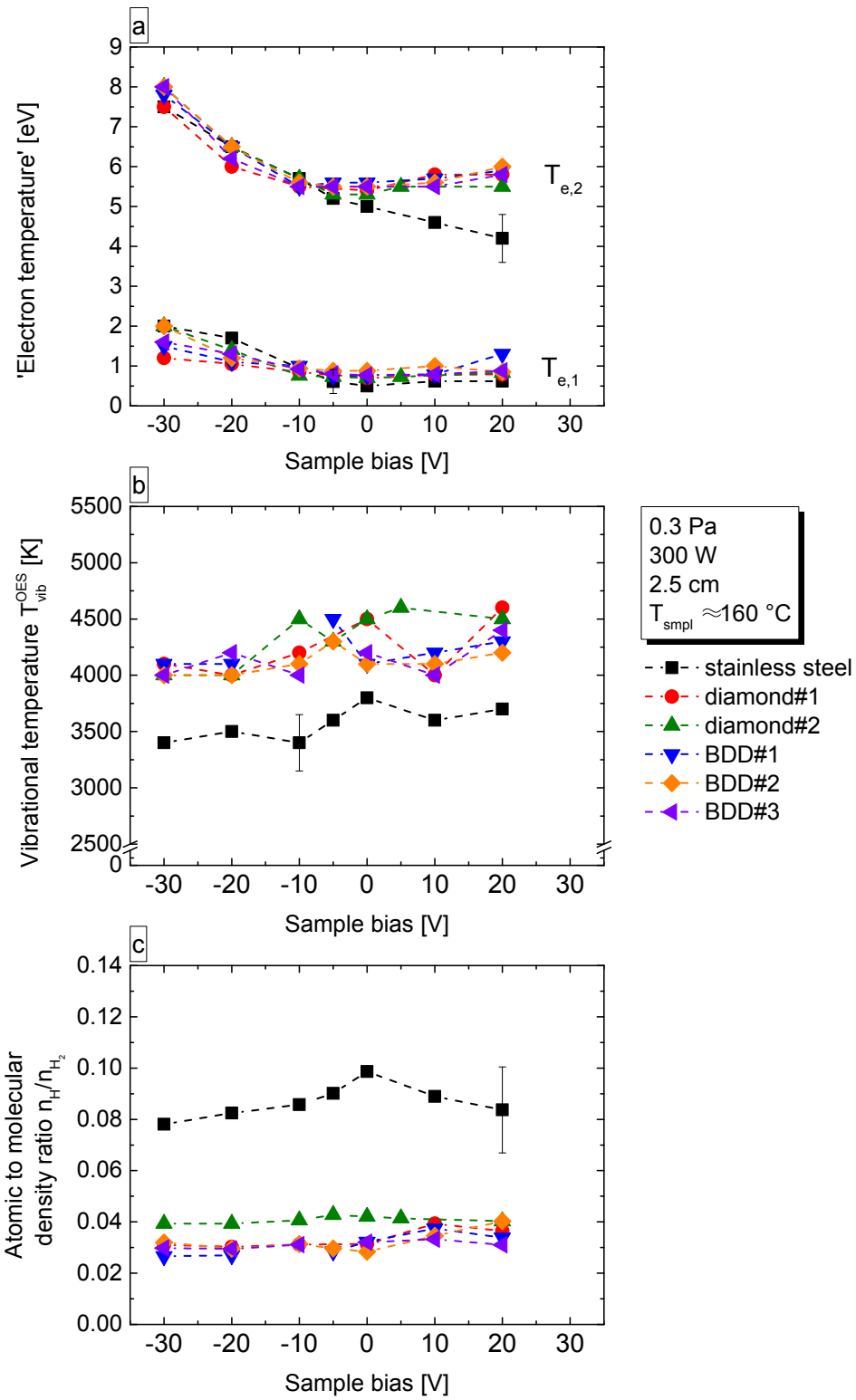

Figure 8.13: *(a) 'Electron temperatures', (b) atomic to molecular density ratio and (c) vibrational temperature* $T_{\mathrm{vib}}^{\mathrm{OES}}$ *for diamond, BDD and stainless steel as a function of sample bias.*

In another low pressure hydrogen discharge a similar effect for graphite, i.e. another carbon based material on the vibrational temperature has been reported by [HF01] and for the atomic hydrogen density by [Fan04]: The authors reported that compared to stainless steel the presence of graphite resulted in increased T_{vib} and decreased n_{H}.
The vibrational population and the atomic to molecular hydrogen density ratio is resulting from various processes in the plasma volume and plasma surface interaction. Compared to metals, a high Eley-Rideal reactivity, i.e. the catalytic reformation of atomic hydrogen at a surface resulting in a vibrationally excited H_2 molecule, has been found for graphite in calculations performed by [JL01]. This is in line with the reported results in [HF01] and [Fan04]. However, graphite and diamond differ e.g. in the crystallographic structure and the strength of bonds between H and the substrate. After [JL01] the strength of H substrate bonds affects the reactivity of the Eley-Rideal process, i.e. the cross section increases with decreasing bond strength. Thus, the effect should be weakened in case of diamond compared to graphite. However, also for diamond sp^2 hybridised phases are present at grain boundaries and defects and consequently a high Eley-Rideal reactivity can arise. Furthermore, for the investigated diamond materials, indications for plasma induced surface erosion and amorphization is found (see section 8.2.3). Thus, indications are given, that a high Eley-Rideal reactivity of the diamond surfaces might be present. Furthermore, the measured effects might also be a consequence of a modification of the vessel wall surfaces, resulting from the re-deposition of eroded sample material in an amorphous structure having a high Eley-Rideal reactivity.
Moreover, the detected erosion indicates the presence of hydrocarbons in the plasma volume for which an enhancing character on the vibrational population of hydrogen molecules has been reported by [FM01].

The shown plasma parameters affect the volume production of negative ions. For modelling H^- related volume processes, an analogue approach for deducing the diagnostically not accessible population of vibrationally highly excited states is applied as described in chapter 8.1 (see page 8.1.1, second approach). $T_{\mathrm{vib},2}$ is consequently taken for modelling n_{H^-} for diamond materials, from fitting modelled data to measured stainless steel data: $T_{\mathrm{vib},2}$ ranges from 8300 K in

the positive and moderate negative bias range, where it is virtually constant, to 10600 K in the negative bias range (see figure 8.6). Since already higher values for the diagnostically determined vibrational temperature $T_{\mathrm{vib}}^{\mathrm{OES}}$ in case of diamond materials are given than for stainless steel, it is expected that the deduced vibrational temperatures $T_{\mathrm{vib},2}$ represent a lower limit in case of diamond materials and may even be increased.

For all investigated diamond and BDD materials a comparable evolution of measured and modelled data is found. Figure 8.14 exemplarily shows the results for diamond#2 and BDD#3 compared to stainless steel.

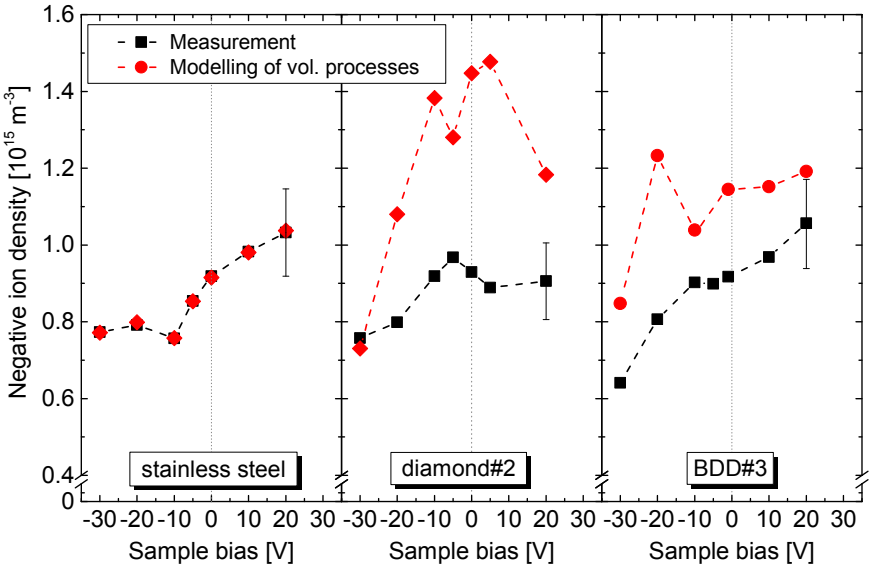

Figure 8.14: *Comparison of measured and modelled n_{H^-} for stainless steel, diamond#2 and BDD#3 as a function of sample bias. The modelled n_{H^-} is based on measured plasma parameters assuming a $T_{\mathrm{vib},2}$ deduced via fitting modelled to measured stainless steel data.*

Using measured input parameters modelling for diamond and BDD results over the complete bias range in higher negative ion densities than have been measured (up to 66 %). The high negative ion densities deduced via modelling are on the one hand a consequence of the high measured vibrational temperatures which result in a high volume production rate and of the comparably low destruction rates via collisions with low density H atoms on the other hand.

The results imply that no direct negative ion surface formation seem to be present but rather indications for a decreasing influence of the diamond materials on the

negative ion density are given. As described in section 4.1.3, H^- are confined within the bulk plasma due to the plasma surrounding sheath which repels negatively charges particles. Thus, no pronounced H^- destruction directly at the investigated diamond/BDD surfaces is expected and the negative ion density should mainly be influenced by changes in the volume processes.
This implies either the presence of mechanisms adversely affecting the population of vibrationally highly excited H_2 and thus $T_{\mathrm{vib},2}$ even if higher $T_{\mathrm{vib}}^{\mathrm{OES}}$ are measured, or the presence of further H^- destruction mechanisms e.g. by hydrocarbon collisions.
In combination, these effects could counteract the beneficial effects of the measured increased vibrational temperature $T_{\mathrm{vib}}^{\mathrm{OES}}$ and the reduced destruction rate via atomic collisions.

In [APC+14] the authors correlate the increased relative negative ion yield in the presence of diamond materials with a changing sp^3/sp^2 hybridisation ratio induced by hydrogen plasma exposure within their experimental setup. However, they applied comparably high biases (positive ion energies of $\sim$60 eV [APC+14]) and in combination with the expected low atomic hydrogen fluxes in their experimental setup, the plasma surface interaction clearly differs from HOMER and negative ion sources. Thus, the absence of a significant effect on the negative ion density at HOMER could be a consequence of a differently evolving sp^3/sp^2 hybridisation ratio caused by the lower energetic positive ion flux and the additionally given high flux of atomic radicals, i.e. H atoms. While the conditions at HOMER, i.e. at negative ion sources could be generally unfavourable for negative ion surface formation at diamond materials it also has to be noted that [KAP+11, APC+14] measured only a change of the *relative* negative ion yield. Thus, a comparable effect of negative ion formation at the investigated diamond surfaces might be also present at HOMER but not be sufficient to result in a comparable amount of negative ions like the volume processes. Hence, negative hydrogen ion formation at the investigated surfaces might be masked by changes of the volume processes.

8.2.2 Effect of Temperature Increment for Diamond Materials

In [KAP+11] and [APC+14] the most pronounced enhancement of the measured relative negative ion yield has been reported, when diamond and BDD samples were heated to 400 °C. Thus, investigations with diamond materials regarding the absolute negative ion density as a function of sample temperature are conducted at HOMER.
In figure 8.15 the negative ion density measured as a function of sample temperature is shown for all investigated diamond and BDD samples. For comparison, the mean negative ion density measured with the non-heated stainless steel reference sample is plotted including the margin of error indicated by the highlighted area. The average sample temperature for stainless steel caused by inherent plasma heating was below 160 °C. Measurements are performed in hydrogen at 0.3 Pa and 300 W discharge power in a relative distance of the sample of 2.5 cm without the application of any bias (i.e. samples are on floating potential).

As can be seen, no systematic trend of the measured negative ion density is visible. Furthermore, absolute densities comparable to those with stainless steel are determined independent of material or temperature. Moreover, no effect of elevated temperatures on the positive ion density, the electron and vibrational temperatures or the atomic to molecular density ratio is observable within the error margins. For the determined gas temperature a slight increment of about 20 K is given with increasing surface temperature.

In a further campaign, a possible interplay of effects coming from temperature increment and increased positive ion energy is investigated by varying the sample bias between -30 and 0 V for BDD samples heated to 430 °C. In figure 8.16 the negative ion density as a function of sample bias is shown for the different BDD samples at elevated sample temperature.

Independent of heating the BDD samples or not, virtually the identical negative ion densities within the error margins are given and heating the BDD samples does not result in an enhancement of n_{H^-} compared to stainless steel.

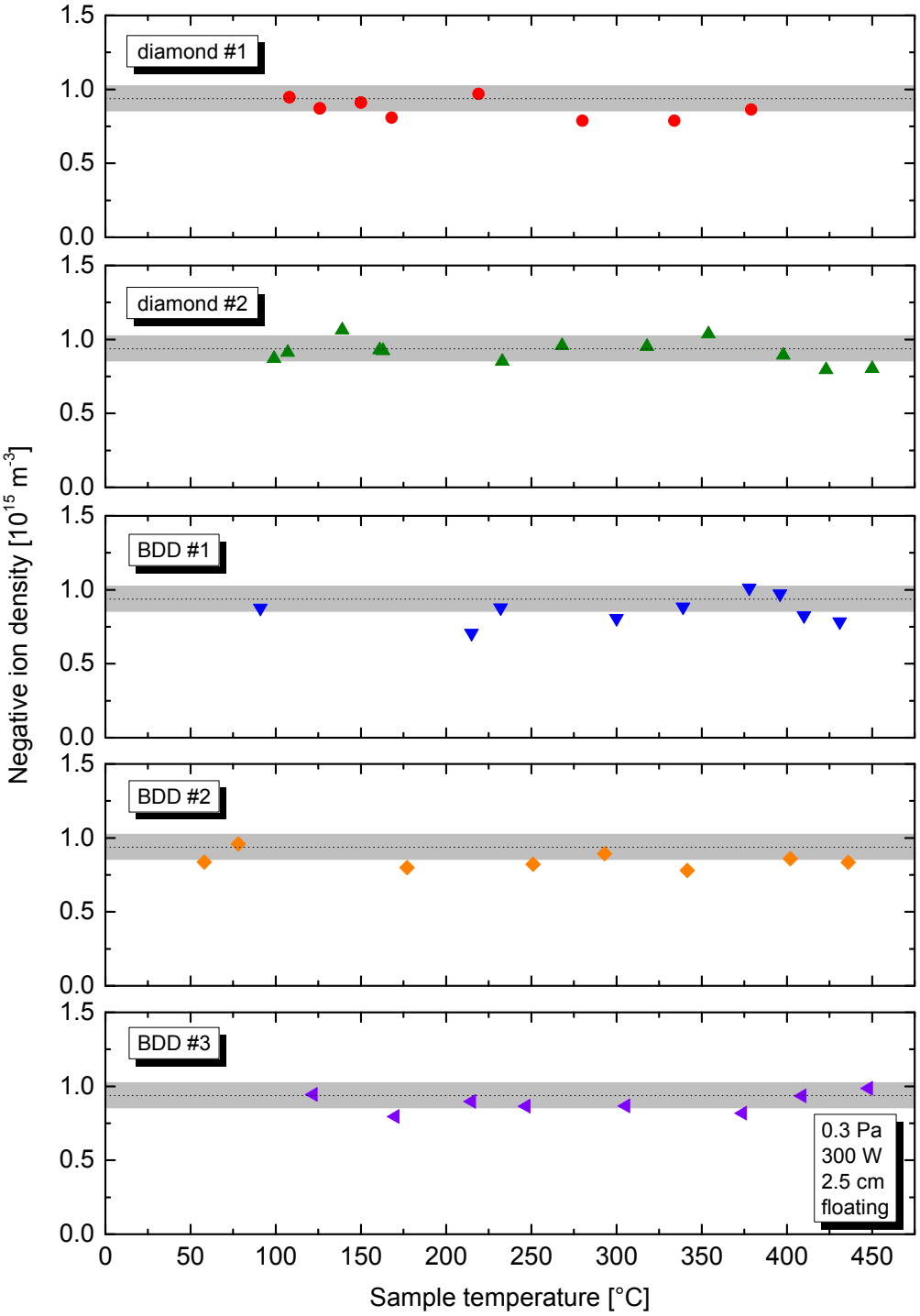

Figure 8.15: *Negative ion density as a function of temperature for diamond and BDD samples compared to a not additionally heated stainless steel sample ($T_{\mathrm{smpl}} \approx 160\,°C$).*

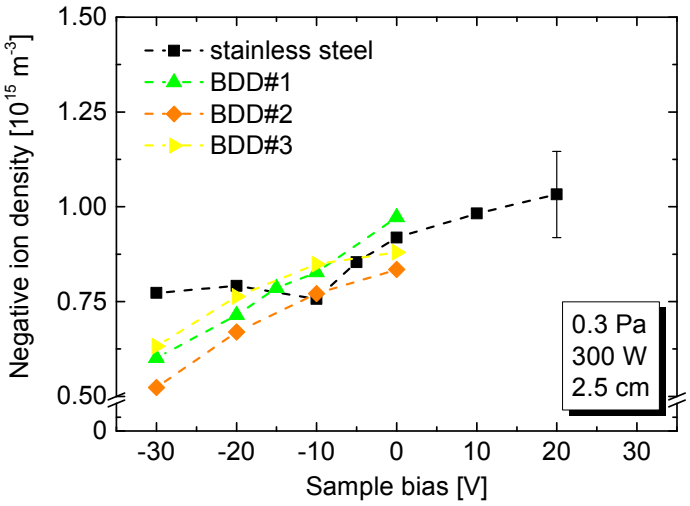

Figure 8.16: *Negative ion density as a function of sample bias for heated BDD samples ($T_{\mathrm{smpl}} \approx 430°C$) compared to stainless steel sample (not additionally heated, $T_{\mathrm{smpl}} \approx 160°C$).*

8.2.3 Plasma Induced Surface Modification

The monitoring of a potentially present plasma induced erosion of the investigated surfaces by sample weight measurements were performed before and after the respective investigations on the influence of diamond materials on the negative ion density. For minimizing a contamination of the discharge chamber by venting the system, the weight is measured at the very end of the complete set of investigations for each sample. As has been described, for the diamond materials different measurement campaigns (bias scan with or without additional heating) are performed and consequently, the plasma exposure time and experimental conditions vary. In table 8.2 the relative weight loss as well as the relative weight loss per plasma-on-time is listed. The average plasma-on-time is between 10 and 15 hours. For all diamond samples ($m \gtrsim 2\,\mathrm{g}$) a reduced weight is given after plasma exposure. The average erosion rate is about $1\times10^{-3}\,\mathrm{g/h}$ and the observed mass loss is lower than the mass of the respective diamond layers, but clearly shows a plasma induced erosion.

This observation is generally in line with the well-known effect of material erosion of carbon based materials including diamond due to hydrogen plasma exposure which is intensively investigated e.g. in the context of suitable materials for the walls in future fusion machines (see for instance [Bro93, Sta05, TDJ+09]).

Table 8.2: *Weight loss and weight loss per plasma-on-time of investigated diamond materials due to plasma exposure. Performed investigations: (a) bias scan without additional heating, (b) bias scan with additional heating, (c) temperature scan.*

Material	Relative weight loss [‰]	Relative weight loss per plasma-on-time [‰/ h]	Treatment
diamond#1	1.4	0.2	a, c
diamond#2	6.4	0.6	a, c
BDD#1	0.7	0.05	a, b, c
BDD#2	0.8	0.07	a, b, c
BDD#3	0.3	0.02	a, b, c

The plasma induced surface modification is further investigated for the different BDD samples: BDD#1 is analysed at the PIIM laboratory using Raman and optical spectroscopy [Gil15]. For BDD#2 and BDD#3 the plasma induced surface modification was investigated via SEM[8] at the University of Augsburg [Gut15].

The BDD#1 diamond layer, deposited on a silicon substrate waver showed a non-uniform layer thickness before plasma exposure, i.e. a lower thickness of the diamond layer at the sample edges than at the centre of the sample. According to density and potential profile measurements at HOMER performed by [Die05], the plasma at the location of the sample holder is homogeneous and plasma induced erosion is consequently expected to be uniform over the whole sample area. The surface structure is investigated by means of optical microscopy and Raman spectroscopy at different positions from the centre towards the edge. Corresponding pictures and data are shown in figures 8.17 and 8.18 where for comparison also a untreated, i.e. non-eroded BDD sample is included, labelled with (a). Measurements performed at the centre position are labelled with (b) and on-going enumeration corresponds to positions recorded moving towards the thinner edge[9].
The surface structure of the untreated diamond surface, looked at with an optical microscope shows typical sharp crystalline edges and structures of the diamond sample (see inset in figure 8.17 (a)). Furthermore, the untreated BDD diamond

[8]Scanning electron microscopy.
[9]It has to be noted that in figure 8.18 no Raman spectrum corresponding to position (f) is depicted as nearly no more diamond layer is present.

layer is recognizable by homogeneously distributed dark structures. In contrast to the untreated sample, the surface structure of the plasma exposed BDD sample, depicted in figure 8.17 (b), partially loses the typical sharp crystalline edges, indicating plasma induced erosion. Furthermore, going from figure 8.17 (b) to (f) more and more parts of the silicon substrate become visible as can be seen by the bright parts, furthermore showing the erosion. In figure 8.18 corresponding mea-

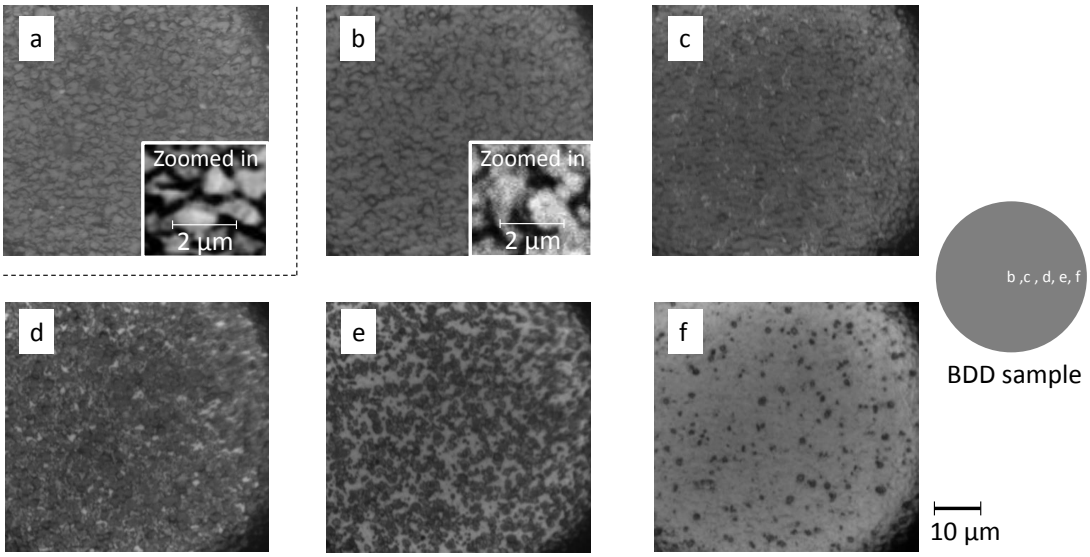

Figure 8.17: *Surface of (a) untreated BDD sample and (b) to (f) of the after plasma exposure at HOMER eroded BDD#1 surface at different positions on the sample from the centre to the edge as indicated in the schematic on the right, recorded by optical microscopy [Gil15].*

surements by means of Raman spectroscopy (performed at PIIM laboratory) are shown. Additionally, to the measurements at the positions (b) to (f), a spectrum of the untreated (non-exposed) BDD sample is depicted (black curve in figure 8.18).

The Raman spectra of the untreated BDD sample and at position (b) of exposed BDD sample are characterized by the diamond peak at around 1300 cm^{-1} and the boron peak at ∼1200 cm^{-1}. Moving towards the eroded zone (towards (e) in figure 8.17), the silicon peak at ∼950 cm^{-1} appears and grows. Since the intensity is correlated with the layer thickness, the spectra of the exposed sample clearly show the decrease of the BDD film thickness and the increase of the silicon substrate contribution. Furthermore, slight indications for the appearance of the G band at ∼1600 cm^{-1} and the D band at ∼1520 cm^{-1} are present which may imply the

establishment of sp^2 bonds and non-diamond sp^3 bonds. These bond structures can be a consequence of surface amorphization induced by plasma bombardment [Gil15].

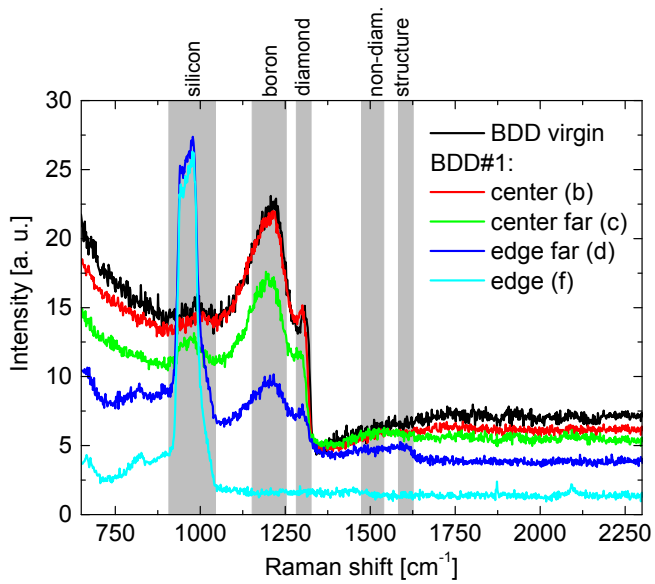

Figure 8.18: *Raman spectra of a untreated BDD and the BDD#1 sample after plasma exposure at HOMER. For the latter, the spectra are recorded at different positions on the sample corresponding to positions labelled with (b) to (e) in figure 8.17 [Gil15].*

For the investigations on BDD#2 and BDD#3 at HOMER, a stainless steel mask is used for covering a defined area of the samples from plasma exposure. Exemplarily SEM pictures of the BDD#3 sample are shown in figure 8.19. In figure 8.19 (a) a section is depicted, where a dark and a lighter area is visible. The darker area was covered by the stainless steel mask and represents the pristine surface structure. The lighter part was exposed to the hydrogen plasma at HOMER. In figures 8.19 (b) and (c) zoomed-in pictures of both areas are shown.
As can be seen, the pristine, i.e. polycrystalline surface structure (b) is clearly modified due to plasma exposure (c). The plane textures present in the pristine area (b) are transformed into structures of a higher surface roughness (c).
Despite the weight loss and the shown surface modifications, no emission coming from carbon atoms or molecules and/or from C_xH_y $(x, y = 1, 2, 3, \dots)$ was observed throughout the campaigns. This implies that only low particle densities of corresponding species are present in the bulk plasma. It is estimated by taking the diamond sample's weight loss and the particle diffusion into account, that the

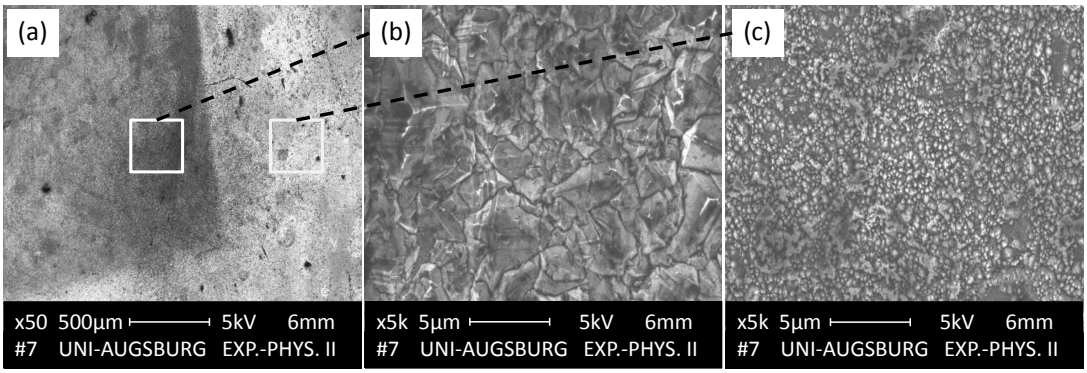

Figure 8.19: *SEM pictures of BDD#3. (a) Section showing pristine (dark) and plasma exposed areas (lighter). (b) Zoomed-in in pristine area. (c) Zoomed-in in plasma exposed area [Gut15].*

carbon particle density is comparably low, i.e. at least three orders of magnitude smaller than the atomic hydrogen density.

8.2.4 Conclusion

The effect of different diamond and BDD materials on the negative ion density was investigated as a function of sample bias and surface temperature. Compared to stainless steel, none of the samples resulted in a systematic increase of the negative ion density independent of bias and temperature. Furthermore, clear signs for plasma induced erosion were observed.

The diamond materials influenced the overall plasma conditions, which was discussed to be possibly correlated with the clearly observable surface erosion: The vibrational temperature $T_{\mathrm{vib}}^{\mathrm{OES}}$ was systematically increased by about 500 K and the atomic to molecular density ratio reduced by up to 70 % compared to stainless steel. Based on these measured input data, modelled H^- related volume processes would result in higher n_{H^-} than were measured. This implies the presence of additional processes that may result in a decreased population of vibrationally highly excited H_2 states or the presence of an additional H^- destruction channel.

The absence of a measurable effect on n_{H^-} by the increment of sample temperature indicates that the sp^3/sp^2 hybridisation ratio cannot be beneficially influenced by the present ion source relevant plasma conditions for yielding efficient H^- surface formation. Indeed, Raman spectra of BDD#1 do not show a pronounced signal coming from sp^2 phases, which is discussed as important perquisite for H^-

formation on diamond in the literature [APC+14].
Since for the application in negative ion sources for future NNBI systems, a potential caesium-free alternative converter material has to provide a constantly high negative ion formation efficiency and simultaneously has to withstand the plasma exposure over long term, the gained results show that the investigated diamond samples are not suitable.

8.3 Investigations with Tantalum and Tungsten

Motivated by the discrepancies reported in literature in combination with tantalum and tungsten (see section 4.1.1), the effect of tantalum and tungsten is systematically investigated at ion source relevant conditions at HOMER. Consistent with the performed investigations described on low work function and diamond materials, solid bulk samples are used.
Investigations are performed as function of pressure between 0.3 and 3 Pa. The distance between the floating sample and the Langmuir probe is set to 4.5 cm and the discharge power is 300 W.

The bulk tantalum and tungsten samples have a size of $8.5\times6\,\mathrm{cm}^2$ and were mechanically polished and cleaned with purified water, acetone and isopropyl alcohol. Residual humidity was reduced by drying with nitrogen gas. The discharge is started one hour before starting the experiments. Thereby, the samples were inherently heated by the plasma up to 160 °C. None of the investigated samples showed any signs of plasma induced erosion determined by monitoring the plasma emission and the equality of sample weight before and after the campaigns.

8.3.1 Pressure Variation

In figure 8.20 the negative ion density is shown, measured for tantalum, tungsten and the stainless steel reference sample.

Compared to the stainless steel reference sample, no systematic enhancement of the negative ion density is visible. For all materials, n_{H^-} is increasing from $1.5\times10^{15}\,\mathrm{m}^{-3}$ at 0.3 Pa to $2.7\times10^{15}\,\mathrm{m}^{-3}$ at 0.5 Pa and decreases with further

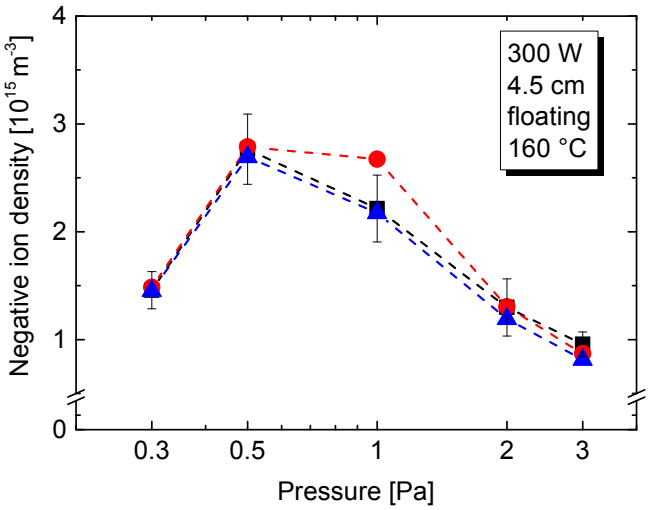

Figure 8.20: *Negative ion density as a function of gas pressure for tantalum, tungsten and stainless steel.*

increasing pressure down to about $9 \times 10^{14}\,\mathrm{m}^{-3}$.
Except for the atomic to molecular density ratio comparable plasma parameters are present independent of the installed material sample (see figures 7.3 to 7.5). In contrast to the measurements performed with the stainless steel reference sample where an atomic to molecular hydrogen density ratio between 9.5 % and 16.3 % is determined, $n_{\mathrm{H}}/n_{\mathrm{H}_2}$ lies between 7.7 % and 13.2 % for tantalum and tungsten, i.e. is slightly decreased.

Comparable vibrational temperatures $T_{\mathrm{vib}}^{\mathrm{OES}}$ of constantly about 3600 K between 0.3 Pa and 1 Pa decrease for all materials down to 3200 K at 3 Pa.
Although not significantly pronounced, the lower atomic to molecular hydrogen density ratio given in case of tantalum and tungsten results in a reduced negative ion destruction rate via atomic collisions. As has been described in section 7.1.1, (non-)associative attachment represents the dominant destruction channel. Since virtually the same n_{H^-} are measured for all three metals independent of pressure, this implies a reduced negative ion formation via dissociative attachment to balance the lower destruction rate. It has to be noted that these variations are almost within the accuracy of the $n_{\mathrm{H}}/n_{\mathrm{H}_2}$ and n_{H^-} determination.
For matching on bases of measured input parameter, modelled n_{H^-} to measured data, slightly lower vibrational temperature $T_{\mathrm{vib},2}$ describing the vibrationally highly excited states are given. For tantalum and tungsten modelled negative ion

densities reproduce the measurement for vibrational temperatures $T_{\mathrm{vib},2}$ between 7650 and 10130 K which is up to 560 K lower than in case of stainless steel.
Hence, no indication for an enhancing effect on the vibrational population is visible, neither for tantalum nor for tungsten. Comparing tungsten and stainless steel, this is in line with results reported by [HF01], where within the error bars also virtually the same vibrational temperatures $T_{\mathrm{vib}}^{\mathrm{OES}}$ have been determined for these two metals in a low pressure low temperature hydrogen discharge.

It has to be noted that presented investigations are performed using bulk material samples. In contrast, [IMO+92] and [BGI+02, BIG+04], reported about increased negative ion densities, when they modified the wall material by evaporation of tantalum or tungsten from corresponding filaments which covered the walls. And also investigations reported by [LEP85] where different rods of bulk material have been used, were performed in a tungsten filament driven arc discharge. Consequently it can be assumed that also within these investigations, material evaporation is present which results in a comparable coverage like discussed in [IMO+92] and [BGI+02, BIG+04]. Thus, a significant difference between those investigations and the ones performed at HOMER is present regarding the effective surface area and the surface structure. According to [BIG+04], both parameters are affecting the H trapping, i.e. the atomic hydrogen density within the discharge on the one hand and the hot-atom formation process, i.e. the catalytic formation of vibrationally excited hydrogen molecules on the surface which can subsequently desorb into the bulk plasma (see section 4.1.2).

8.3.2 Conclusion

Bulk samples of tantalum and tungsten were investigated as a function of pressure between 0.3 and 3 Pa. Within the performed investigations neither the application of tantalum nor of tungsten bulk samples resulted in a measurable enhancement of the negative ion density compared to stainless steel. Except for the atomic to molecular hydrogen density ratio, none of the plasma parameters correlated with the H^- volume processes showed a material dependence. Especially regarding the population of vibrationally excited molecules no indications for any surface induced enhancement could be observed.
Investigations were performed using bulk material samples but could be extended by evaporating filaments for modifying the wall surface like in case of investigations performed by [IMO+92] and [BGI+02, BIG+04]. However, the backgrounds for finding caesium-free alternative materials for the application in future negative

ion sources include problems correlated with the presently required evaporation of caesium, like an unwanted migration into the extraction and acceleration multi-grid system. Thus, it is questionable whether evaporation of tantalum or tungsten is suitable for future NNBI systems that need to fulfil the RAMI requirements. Taking this into account together with the absence of a measurable enhancement of the negative ion density for bulk samples, tantalum and tungsten can generally not be seen as alternative converter materials for efficient negative ion formation applied in future negative ion sources for NNBI.

8.4 Overview of the Maximal Negative Ion Densities for the Investigated Materials

A caesium-free alternative material should result in a comparable enhancement of the negative ion density like the application of caesium or at least eliminated linked drawbacks when a slightly lower enhancement is given. To give an overview of the measured negative ion densities in combination with the different investigated caesium-free alternatives the maximally achieved negative ion densities are presented in figure 8.21 compared to the case for the in-situ caesiated stainless steel sample labelled as 'stainless steel + Cs' (see chapter 7.1.2). All of the shown measurements were performed at equal external parameters.

At ion source relevant plasma conditions present at HOMER, neither bulk samples of the refractory metals tantalum and tungsten nor any of the investigated diamond materials have resulted in a measurable increase of the negative ion density but virtually the same negative ion densities like in case of stainless steel were measured. The absence of an enhancing effect and in case of diamond the observed erosion, which contradicts the required stability of a converter material for long-term application in negative ion sources, show that these materials cannot be seen as suitable caesium-free alternatives.

An enhancement of the negative ion density was measured only with the low work function materials MoLa and LaB_6. Both materials furthermore did not show any signs of plasma induced erosion, i.e. proved to be stable for long time spans of plasma exposure. Thus, basically both materials are suitable for being applied in negative ion sources for future NNBI systems. However, within the performed investigations none of these materials resulted in a comparably high negative ion density as in case of application of caesium.

On the other hand, it has to be noted that when MoLa or LaB_6 would be applied, difficulties related to the complex evaporation, adsorption and/or redistribution dynamics of caesium including a possible migration into the multi grid system would be cancelled out, since bulk samples could be used that did not show any signs of erosion.
Furthermore, dedicated investigations regarding the maximally extractable negative ion currents at simultaneously given co-extracted electron currents are required in order to evaluate the full potential of MoLa and LaB_6 for being caesium-free alternative converter materials in negative ion sources. Although it is well-known that negative ion surface formation reduces the amount of electrons in the vicinity of the converter surface (see for instance [FF13b]), the actual influence of these materials on the extracted currents have to be investigated directly at a negative ion source providing an extraction system.
Another issue that should be addressed in further investigations is the evolution of the respective work functions during plasma exposure, regarding their stability as well as possibilities for maintaining lowest possible values and counteracting any unwanted deterioration.

Generally, the results show that materials with inherent low work function can be seen as the most promising types of materials for being caesium-free alternatives in future NNBI ion sources like for DEMO and it is recommended that further investigations should be focused on this type of materials.

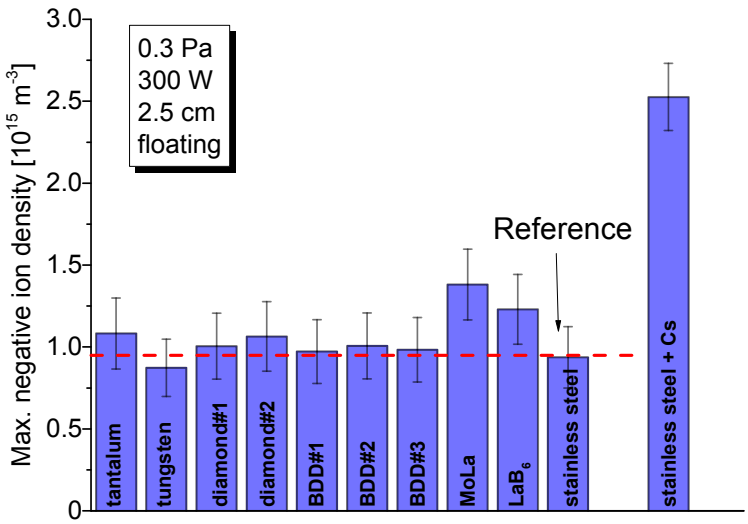

Figure 8.21: *Maximally measured negative ion density for different materials at equal external experimental conditions.*

9 Summary

A main auxiliary system for heating and current drive at the fusion experiment ITER will be neutral beam injection based on negative ions (NNBI). Depending on the scenario, it will be also of major importance for DEMO, the next step fusion device and the first machine to produce net electricity based on thermonuclear fusion. Respective future NNBI systems will have to provide for long pulses of up to one hour, high energetic energy beams in the MeV range. Furthermore, a high negative ion current density (ITER NNBI: $200\,\mathrm{Am}^{-2}$) has to be extracted and accelerated from the corresponding negative ion sources with the constraint of a current ratio of inevitably co-extracted electrons to negative ions of below unity.

Currently, no systems exist that fulfil such challenging requirements and the test stand MITICA[1] will be the first device allowing to access the full performance. Research and development for future NNBI systems is performed, focused for example on efficient negative hydrogen ion formation. Up to date, high performance negative ion sources are based on negative ion formation by atom and positive ion conversion at a caesiated plasma grid. Therefore, caesium is evaporated into the ion source volume to cover the grid surface, lower it's work function and thus significantly enhance the H^- surface formation probability. However, although various requirements have already been shown to be compliable with this procedure (e.g. the demanded negative current density at an electron to negative ion current ratio below unity), there are several drawbacks inherently linked to the application of caesium: caesium is chemically very reactive and susceptible to form compounds with residual impurities, which leads to an unwanted spatially and temporally inhomogeneous degradation of the plasma grid's work function. In order to counteract this, continuous evaporation of fresh caesium is necessary and together with an inherent plasma induced caesium redistribution, a complex caesium dynamic is given. This affects the stability and reliability of the source performance and results in an unwanted caesium consumption. Therefore,

[1] MITICA (**M**egavolt **I**TER injector **C**oncept **A**dvancement).

caesium-free alternative materials are highly desired for the application in future ion sources, granting a comparably high efficiency for negative ion formation like caesium.
In this context, caesium-free materials were investigated within this work at ion source relevant plasma conditions and their effect on the negative ion density was directly compared with the effect of caesium application at one distinct experimental setup. Investigations were performed at the flexible ECR discharge HOMER, a laboratory experiment which is equipped with various diagnostics including laser photodetachment allowing for a locally resolved determination of the negative ion density. HOMER provides ion source relevant plasma conditions and a meshed grid is used for applying the tandem principle, i.e. for separating the plasma volume into a heated driver and a diffusive downstream region. The setup allows for investigating the effect of different caesium-free materials on the negative ion density in the diffusive downstream region as a function of sample temperature, sample bias, relative distance to the sample surface and of gas pressure. For comparability reasons, all these investigations were performed at the same discharge power of 300 W.
Since the determined negative ion density is a consequence of H^- related volume processes and of a possibly present H^- surface formation, a material induced enhancement of the negative ion density is only detectable when it is at least comparable to the amount of negative ions coming from volume processes. As the materials themselves can influence the bulk plasma, the H^- related volume processes can also be influenced by the investigated materials. Therefore, volume processes were modelled by balancing volume formation against the different destruction mechanisms via the 0-dimensional model *Yacora* H^- on basis of measured plasma parameters which were determined via Langmuir probe and OES measurements. A detailed knowledge of the negative ion related volume processes allows to assess the amount of surface produced negative ions.
For comparison of the gained results, measurements with a stainless steel reference sample were performed, which represent the negative ion density due to pure volume processes. Together with the investigations on the effect of in-situ application of caesium, these measurements allow to set performed investigations on caesium-free alternative materials into perspective.

A first characterisation of the volume processes, using the stainless steel reference sample was performed in a pressure range between 0.3 and 3 Pa. In a relative

distance to the sample surface of 4.5 cm the measured negative ion density is peaked at 0.5 Pa and ranges between 1.0 and $2.8\times10^{15}\,\mathrm{m}^{-3}$, i.e. within typical values known from other discharges where H^- volume formation is investigated. Modelling the volume processes based on a simple Boltzmann distribution for describing the vibrational population of H_2 states, results in lower negative ion densities than have been measured. For an experimentally via OES determined vibrational temperatures of 3700 to 3100 K modelled n_{H^-} are at least one order of magnitude lower compared to measurement. However, H^- volume formation is rather sensitive on the diagnostically not accessible population of vibrationally highly excited states with $\nu \geq 5$. Thus, modelling was performed by describing the vibrational population with a two-temperature-Boltzmann distribution, using $T_{\mathrm{vib},1}$ as determined via OES for the low lying vibrational states and $T_{\mathrm{vib},2}$ for the vibrationally highly excited states as a free adjustable parameter. The description of the vibrational population via a two-temperature-Boltzmann distribution is a well known procedure which is often applied in literature and the applicability has been confirmed by various groups in distinct investigations. Within the present work, the enhanced population of vibrationally highly excited states is in line with the tandem principle design of HOMER and the correspondingly modelled negative ion density matches the measured n_{H^-} over the whole investigated pressure range for $T_{\mathrm{vib},2}$ being between 7700 and 10300 K, i.e. being increased by about 5000 K compared to $T_{\mathrm{vib},1}$.
Moreover, modelling revealed that (non-)associative detachment, i.e. H^- destruction via collisions with atomic hydrogen, is the most relevant destruction channel. It contributes by more than 74 % to the total share of negative ion destruction. According to this result, the negative ion density resulting from volume processes at HOMER is dominantly determined by the evolution of the H^- volume formation process, i.e. determined by the electron density, the population of vibrationally highly excited H_2 states and the EEDF on the one hand and by the atomic hydrogen density on the other hand which determines the H^- destruction.

The atomic hydrogen density was evaluated within this work via the ratio of the H_γ emission line and the Fulcher emission. It was found that the emission line profile of the Balmer lines are characterised by the superposition of two different Gaussian line profiles with strongly differing FWHM which result from two ensembles of excited atomic hydrogen with different temperatures. The narrow part of the peak is coupled to the hydrogen atomic ground state ensemble. This

ensemble is thermalized prior to excitation with the H_2 background gas resulting in a temperature deduced from the Doppler profile close to the gas temperature. On the other hand, high energetic excited H atoms are formed via dissociative recombination of H_2^+ which results in a Balmer emission with a much broader Doppler profile.
The atomic hydrogen density was determined via the emissivity of the narrow peak, since well-established evaluation procedure is based on Balmer emission coupled to H only. A typical atomic hydrogen density of $3.5\times10^{18}\,\mathrm{m}^{-3}$ was present at an atomic to molecular hydrogen density ratio in the order of 10 %, i.e. typical for low pressure low temperature hydrogen discharges. On the other hand, for the determination of the flux of hydrogen atoms onto the investigated sample materials, the combined peak of 'hot' and 'cold' atoms was evaluated, taking the determined temperatures of the two ensembles into account. Typical fluxes were in the order of $2.5\times10^{21}\,\mathrm{m}^{-2}\mathrm{s}^{-1}$, i.e. in the same order like in negative ion sources and test stands.
A benchmark of the maximally achievable enhancement of n_{H^-} at HOMER was deduced by the in-situ application of caesium via evaporation onto a stainless steel sample surface. Measurements were focused on the ion source relevant pressure of 0.3 Pa and were performed at a relative distance of the sample surface to the applied laser photodetachment diagnostic of 2.5 cm. Corresponding to measurements reported in literature, a reduction of the surface work function down to 2.2 eV was expected by the caesium application. At HOMER the evaporation of caesium results in an immediate increment of the measured negative ion density by up to a factor of 2.5. For the given fluxes of atomic ($\sim 5.0\times10^{21}\,\mathrm{m}^{-2}\mathrm{s}^{-1}$) and positive ionic hydrogen ($\sim 1.0\times10^{20}\,\mathrm{m}^{-2}\mathrm{s}^{-1}$) this enhancement is in line with the increasing effect of caesium application in negative ion sources where atomic and positive ion fluxes are about a factor of seven and six, respectively, higher than at HOMER and caesium evaporation leads to an enhancement of the negative ion density of up to an factor ten. It was found that at HOMER a higher relevancy of the atomic hydrogen flux for H^- formation at a caesiated surface is given than of the positive ion flux, caused by the higher atomic hydrogen flux and the increased respective conversion probability. This is also the case in negative ion sources.

Direct negative ion surface formation is correlated with the reduction of the surface work function as utilized by the application of caesium. Following this, materials with inherent low work function were investigated within this work: A

molybdenum sample doped with 0.7 % of lanthanum (MoLa) comprising an expected work function of 2.6 eV and a LaB_6 sample with an expected work function between 2.7 and 3.0 eV. The values of the work function are taken from literature and are typically determined at very high temperatures $\gtrsim$1000 K. For these low work function materials measurements at 0.3 Pa were focused on sample bias variations between -30 and +20 V in a relative distance to the respective surface of 2.5 cm. The sample were heated for reducing the work function to temperatures which are expected to be relevant from an engineering point of view for negative ions sources, i.e. to 450 °C. Compared to the bare stainless steel reference, the measured negative ion density is increased for both low work function materials over the whole investigated bias range. This increase is most pronounced in the moderate negative and positive bias range with up to 60 % in case of MoLa and 42 % for LaB_6. In the negative bias range it nearly diminishes. Regarding the bulk plasma, it was found that a sample bias variation results for the low work function materials as well as for the stainless steel reference sample mainly in changes of $n_{\mathrm{H}}/n_{\mathrm{H_2}}$ and the mean electron energy. Taking the measured plasma parameters into account for modelling and using different approaches for an enhanced population of highly vibrationally excited H_2 states, volume processes result in case of the low work function materials in lower negative ion densities than have been measured which implies the presence of actual H^- surface formation.
The effect of the low work function materials was furthermore investigated at 0.3 Pa as a function of distance between 1.5 and 4.5 cm without the application of any bias. Again, compared to the stainless steel reference sample increased negative ion densities were measured for the low work function materials in the whole investigated range. Within the distance variations, a clear sensitivity of the relative position of the surfaces on the bulk plasma was identified for all materials. Modelling on bases of measured input parameters revealed a comparable relative evolution of modelled and measured $n_{\mathrm{H^-}}$. However, for the low work function materials, modelling of volume processes results in lower negative ion densities with a nearly constant offset. For an estimated mean free path for surface produced negative ions of about 3 m, this offset would be expected for a present additional negative ion source by H^- surface formation.

Since the highest negative ion densities were measured with MoLa, investigations for this material were extended regarding isotopic differences. Plasma parameters

clearly differ for hydrogen and deuterium, but still virtually the same negative ion densities are measured in a distance of 2.5 cm in D_2 as in H_2, independent of a variation of the applied sample bias between -30 and +20 V. Modelling of the volume processes is not possible in case of deuterium due to the unavailability of required of cross section data. Thus, the evolution of negative ion related volume processes was evaluated qualitatively by discussing the evolution of respectively determining plasma parameters. The most pronounced isotopic differences are the significant increment of the positive ion density (up to 73 %) and the atomic to molecular density ratio (up to a factor of 2.7) in case of deuterium. The comparison of the bulk plasma parameters revealed in deuterium the equally increasing effects on the volume formation and destruction mechanisms. The higher atomic to molecular density ratio in case of deuterium is correlated with an increased atomic particle flux onto the MoLa surface which is about a factor of two higher than in case of hydrogen. In contrast, due to the isotopic mass difference, virtually the same positive ion fluxes are present at given parameters.

As second material group, two non-doped and three boron doped diamond (BDD) samples with different doping levels and substrate materials were exposed to the hydrogen plasma at HOMER. This material group has attracted much interest since negative ion formation was reported in scattering and beam experiments as well as in low density hydrogen discharges by different authors in literature. The effect on the negative ion density was measured in a distance of 2.5 cm at 0.3 Pa as a function of sample bias. Furthermore, the effect of temperature increment was investigated and in case of the BDD samples measurements for bias variations of samples heated to 430 °C were performed. In contrast to the low work function materials, none of the investigated diamond materials resulted in a systematic increment of the measured negative ion density compared to stainless steel, independent of bias and temperature. However, in the presence of diamond materials the vibrational temperature determined via OES ($T_{\mathrm{vib},1}$) is clearly increased by at least 500 K compared to stainless steel. Moreover, the atomic hydrogen density ratio is significantly reduced by up to 70 %. Both effects would result in an increment of the negative ion density coming from the H^- volume processes. As no enhancement of n_{H^-} compared to stainless steel was measured, this implies either the presence of mechanisms which adversely affect the population of highly vibrationally excited H_2 states or of an additional H^- destruction process caused for example by collisions with hydrocarbons coming from the diamond surface.

Furthermore, clear signs of plasma induced erosion were detected for all diamond materials: A reduced sample weight after plasma exposure was measured and by means of optical microscopy, SEM and Raman spectroscopy a modification of the surface structure was detected. This is clearly in contradiction to a demanded resistibility of a converter material in negative ion sources for long-term application.

Refractory metals were the third group of materials which were investigated for their effect on the negative ion density. For bulk tantalum and tungsten samples, the negative ion density was measured in a distance of 4.5 cm within a pressure range between 0.3 and 3 Pa. For both samples no indications for an enhancing effect on the negative ion density was observed and no indications could be identified for an assumed enhancing effect of these materials on the population of vibrationally excited H_2 states. Compared to stainless steel virtually the same negative ion densities and vibrational temperatures were measured within the error margins. Since in case of tantalum and tungsten slightly reduced atomic densities were determined, compared to stainless steel a correspondingly lower H^- destruction by H collisions is present for these metals. Thus, for resulting in virtually identical negative ion densities, even slightly lower vibrationally temperatures $T_{\mathrm{vib},2}$ seem to be given for tantalum and tungsten which leads to a reduced H^- volume formation.

Concluding, within this work various materials known from literature were investigated at ion source relevant plasma conditions, regarding their suitability as a caesium-free alternative converter material needed for the next generation NNBI systems, like DEMO NNBI. As a main result, neither bulk samples of tantalum or tungsten nor any of the investigated diamond materials have resulted in a measurable enhancement of the negative ion density, but rather the same negative ion densities like in the presence of a stainless steel sample were measured. Moreover, all diamond materials showed signs of a plasma induced erosion. This is in clear contradiction of a demanded high negative ion formation efficiency and long-term stability of a suitable converter material applied in future negative ion sources.
Only the investigated low work function materials MoLa and LaB_6 showed a systematic increment of the negative ion density and furthermore, no indications of erosion were found. However, compared to

the enhancement resulting from a direct application of caesium, MoLa as well as LaB_6 resulted in significantly lower negative ion densities. Thus, when these materials are applied in negative ion sources, it consequently has to be tested whether the lower impact on the negative ion density overcompensates the advantage of cancelling out the problems related to the required frequent evaporation of fresh caesium and its complex redistribution dynamics. Furthermore, the maximally extractable amount of negative ions has to be investigated and especially which amount of co-extracted electron currents are thereby given.
Within this work, also isotopic differences on the negative hydrogen ion density were addressed using the MoLa sample since future NNBI systems will mainly be based on deuterium. Virtually the same negative ion densities at simultaneously higher positive ion densities and therefore higher electron densities were measured in D_2.

The performed investigations within this work on caesium-free alternatives at one distinct experimental setup and the direct comparison of gained results showed that the particle conversion at low work function materials are the most promising concepts for finding suitable alternative materials for the application in negative ion sources for future NNBI systems. In this context, investigations should be intensified, also regarding the evolution of the respective work functions during ion source plasma exposure, focused on their stability and on procedures for maintaining lowest values as well as on counteracting an unwanted deterioration.

Bibliography

[ABR57] J. E. Allen, R. L. F. Boyd, and P. Reynolds, *The collection of Positive Ions by a Probe Immersed in a Plama*, Proc. Phys. Soc. B **70** (1957), 297.

[AJS+15] A. D. Ash, T. T. C. Jones, E. Surrey, et al., *JET neutral beam duct Optical Interlock*, Fusion Eng. Des. **96** (2015), 396.

[Alv15] Alvatec GmbH, Austria, *http://www.alvatec.com*, 2015.

[APC+14] A. Ahmad, C. Pardanaud, M. Carrère, et al., *Negative ion production on carbon materials in hydrogen plasma: Influence of the carbon hybridization state and the hydrogen content on H^- yield*, J. Phys. D: Appl. Phys. **47** (2014), 085201.

[Bac93] M. Bacal, *Plasma diagnostics in negative ion sources*, Plasma Sources Sci. Technol. **2** (1993), 190.

[Bac00] ———, *Photodetachment diagnostic technique for measuring negative ion densities and temperatures in plasmas*, Rev. Sci. Instr. **71** (2000), 3981.

[Bac06] ———, *Physics aspects of negative ion sources*, Nucl. Fusion **46** (2006), S250.

[BBB+91] M. Bacal, P. Berlemont, A. M. Bruneteau, et al., *Measurement of the H^- thermal energy in a volume ion source plasma*, J. Appl. Phys. **70** (1991), 1212.

[BBB96] F. El BalghitiSube, F. G. Baksht, and M. Bacal, *Photodetachment diagnostics of plasma with a high $n_{\mathrm{H}^-}/n_{\mathrm{e}}$ ratio*, Rev. Sci. Instrum. **67** (1996), 2221.

[BBN81] M. Bacal, A. M. Bruneteau, and M. Nachman, *Electron collection radius of an electrostatic probe immersed in a low-pressure plasma*, J. Physique - Lettres **42** (1981), 5.

[BDD74] Y. I. Belchenko, G. I. Dimov, and V. G. Dudnikov, *A powerful injector of neutrals with a surface-plasma source of negative ions*, Nucl. Fusion **14** (1974), 113.

[BE00] A. G. Borisov and V. A. Esaulov, *Negative ion formation in the scattering of atoms and ions from dielectric surfaces*, J. Phys.: Condens. Matter **12** (2000), R177.

[Beh91] K. Behringer, *Diagnostics and modelling of ECRH microwave discharges*, Plasma Phys. Control. Fusion **33** (1991), 997.

[BF94] K. Behringer and U. Fantz, *Spectroscopic diagnostics of glow discharge plasmas with non-Maxwellian electron energy distribution functions*, J. Phys. D: Appl. Phys. **27** (1994), 2128.

[BGI+02] M. Bacal, M. Glass-Maujean, A. A. Ivanov Jr., et al., *Influence of Wall Material on VUV Emission from Hydrogen Plasma in H^- Source*, AIP Conf. Proc **639** (2002), 13.

[BHB+79] M. Bacal, G. W. Hamilton, A. M. Bruneteau, et al., *Measurement of H^- density in plasma by photodetachment*, Rev. Sci. Instr. **50** (1979), 719.

[BIG+04] M. Bacal, A. A. Ivanon Jr., M. Glass-Maujean, et al., *Contribution of wall material to the vibrational excitation and negative ion formation in hydrogen negative ion sources (invited)*, Rev. Sci. Instr. **75** (2004), 1699.

[BMT90] V. Bortolani, N. H. March, and M. P. Tosi (eds.), *Interaction of atoms and molecules with solid surfaces*, Plenum Press, New York, 1990.

[BN75] A. Blandin and A. Nourtier, *Localized time-dependent perturbations in metals: formalism and simple examples*, J. Physique **37** (1975), 369.

[BN81] R. Brako and D. M. Newns, *Charge exchange in atom-surface scattering: thermal versus quantum mechanical non-adiabaticity*, Surf. Sci. **108** (1981), 253.

[BPS75] K. H. Berkner, R. V. Pyle, and J. W. Stearns, *Intense, mixed-energy hydrogen beams for CTR injection*, Nucl. Fusion **15** (1975), 249.

[BR59] I. B. Bernstein and I. N. Rabinowitz, *Theory of Electrostatic Probe in a Low-Density Plasma*, Phys. Fluids **2** (1959), 1958.

[Bro93] J. N. Brooks, *Atomi and plasma-material interaction processes in controlled thermonuclear fusion*, Elsevier, Amsterdam (NL), 1993.

[BW79] J. N. Bardsley and J. M. Wadehra, *Dissociative attachment and vibrational excitation in low-energy collisions of electron with H_2 and D_2*, Phys. Rev. A **20** (1979), 1398.

[BW15] M. Bacal and M. Wada, *Negative hydrogen ion production mechanisms*, Appl. Phys. Rev. **2** (2015), 021305.

[CB11] P. Chabert and N. St. J. Braithwaite, *Physics of radio-frequency plasmas*, Cambridge University Press, Cambridge (UK), 2011.

[CBB95] C. Courteille, A. M. Bruneteau, and M. Bacal, *Investigation of a large volume negative hydrogen ion source*, Rev. Sci. Instr. **66** (1995), 2533.

[CEZ12] F. F. Chen, J. D. Evans, and W. Zawalski, *Calibration of Langmuir probes against microwaves and plasma oscillation probes*, Plasma Sources Sci. Technol. **21** (2012), 10.

[Cha87] P. J. Chantry, *A simple formula for diffusion calculations involving wall reflection and low density*, J. Appl. Phys. **62** (1987), 1141.

[Che65] F. F. Chen, *Electric probes*, Plasma Diagnostic Techniques (R. H. Hudelstone and S. L. Leonard, eds.), Academic Press, Los Angeles, California, 1965.

[Che01] ———, *Langmuir probe analysis for high density plasmas*, Phys. Plasmas **8** (2001), 3029.

[Che03] ———, *Langmuir probe diagnostics*, IEEE-ICOPS meeting, (Jeju, Korea), 2003.

[Che09] ———, *Langmuir probes in RF plasma: surprising validity of OML theory*, Plasma Sources Sci. Technol. **18** (2009), 035012.

[Chr88] Christmann, K., *Interaction of hydrogen with solid surfaces*, Surf. Sci. Rep. **9** (1988), 1.

[CJL+01] R. Celiberto, R. K. Janev, A. Laricchiuta, et al., *Cross section data for electron-impact inelastic processes of vibrationally excited molecules of hydrogen and its isotopes*, Atomic Data and Nuclear Data Tables **77** (2001), 161.

[Cro13] B. Crowley, *Private communication*, Culham Centre for Fusion Energy - CCFE, (UK), 2013.

[DAB+89] P. Devynck, J. Auvray, M. Bacal, et al., *Photodetachment technique for measuring H^- velocities in a hydrogen plasma*, Rev. Sci. Instr. **60** (1989), 2873.

[Dia13] DiaCCon GmbH, Germany, *http://www.diaccon.de/de/*, 2013.

[Die05] S. Dietrich, *Aufbau und charakterisierung eines homogenen ecr plasmas*, University of Augsburg - EPP, (Germany), 2005, Diplomarbeit.

[Die10] ———, *Verifikation von optischen Diagnostikmethoden an H_2/D_2 - Plasmen*, Ph.D. thesis, University of Augsburg - EPP, (Germany), 2010.

[DKA+98] L. Diederich, O. M. Küttel, P. Aebi, et al., *Electron affinity and work function of differently oriented and doped diamond surfaces determined by photoelectron spectroscopy*, Surf. Sci. **418** (1998), 219.

[DP40] M. J. Druyvesteyn and F. M. Penning, *The Mechanism of Electrical Discharges in Gases of Low Pressure*, Rev. Mod. Phys. **12** (1940), 87.

[Dru30] M. J. Druyvesteyn, *Der Niedervoltbogen*, Z. Phys. **64** (1930), 781.

[EBL+88] P. J. Eenshuistra, J. H. M. Bonnie, H. Los, et al., *Observation of Exceptionally High Vibrational Excitation of Hydrogen Molecules Formed by Wall Recombination*, Phys. Rev. Lett. **60** (1988), 341.

[Ert10] D. Ertle, *Teilchendichten in HF-angeregten Wasserstoff- und Deuteriumplasmen*, University of Ulm (Germany), 2010, Diplomarbeit.

[Fan04] U. Fantz, *Emission spectroscopy of molecular low pressure plamas*, Contrib. Plasma Phys. **44** (2004), 508.

[Fan06] _____, *Basics of plasma spectroscopy*, Plasma Sources Sci. and Technol. **15** (2006), S137.

[FBB+15a] G. Federici, C. Bachmann, W. Biel, et al., *Overview of the design approach and prioritization of R&D activities towards an EU DEMO*, Fusion Eng. Des. (2015), –, In Press.

[FBB+15b] T. Franke, E. Barbato, G. Bosia, et al., *Technological and physics assessments on heating and current drive systems for DEMO*, Fusion Eng. Des. **96** (2015), 468.

[FF13a] U. Fantz and P. Franzen, *Feasibility and R&D Needs of a Negative Ion Based Neutral Beam System for DEMO*, 24th IAEA Fusion Energy Conference (USA), International Atomic Energy Agency, 2013.

[FF13b] R. Friedl and U. Fantz, *Influence of cesium on the plasma parameters in front of the plasma grid in sources for negative hydrogen ions*, AIP Conf. Proc. **1515** (2013), 255, (to be published).

[FFF+06] U. Fantz, H. Falter, P. Franzen, et al., *Spectroscopy - a powerful diagnostic tool in source development*, Nucl. Fusion **46** (2006), S297.

[FFKN09] U. Fantz, P. Franzen, W. Kraus, and the NNBI Team, *Plasma and beam homogeneity of the RF-driven negative hydrogen ion source for ITER NBI*, AIP Conf. Proc. **1097** (2009), 265.

[FFW12] U. Fantz, P. Franzen, and D. Wünderlich, *Development of negative hydrogen ion sources for fusion: Experiments and modelling*, Chem. Phys. **398** (2012), 7.

[FH98] U. Fantz and B. Heger, *Spectroscopic diagnostics of the vibrational population in the ground state of H_2 and D_2 molecules*, Plasma Phys. Control. Fusion **40** (1998), 2023.

[FHF+13] P. Franzen, B. Heinemann, U. Fantz, et al., *Commissioning and first results of the iter-relevant negative ion beam test facility {ELISE}*, Fusion Eng. Des. **88** (2013), 3132.

[FI92] O. Fukumasa and T. Iwasaki, *Development of a double plasma type negative ion source*, AIP Conf. Proc **287** (1992), 411.

[FM01] U. Fantz and S. Meir, *Diagnostics of hydrocarbons and their influence on hydrogen plasmas*, ECA **25A** (2001), 273.

[Fri13] R. Friedl, *Experimental investigation on the caesium dynamics in H_2/D_2 low temperature plasmas*, Ph.D. thesis, University of Augsburg - EPP, (Germany), 2013.

[Fri15] ———, *Private communication*, University of Augsburg - EPP, (Germany), 2015.

[FSW14] U. Fantz, L. Schiesko, and D. Wünderlich, *Plasma expansion across a transverse magnetic field in a negative hydrogen ion source for fusion*, Plasma Sources Sci. Technol. **23** (2014), 044002.

[GAB+15] G. Giruzzi, J. F. Artaud, M. Baruzzo, et al., *Modelling of pulsed and steady-state DEMO scenarios*, Nucl. Fus. **55** (2015), 073002.

[GBD+05] R. Gobin, K Benmeziane, O. Delferriere, et al., *Status of the Negative Hydrogen Ion Test Stand at CEA Saclay*, AIP Conf. Proc **763** (2005), 289.

[GD99] C. Goeden and G. Dollinger, *Electron stimulated desorption on diamond (100) as negative hydrogen source*, Appl. Surf. Sci. **147** (1999), 107.

[GDF00] C. Goeden, G. Dollinger, and P. Feulner, *Electron stimulated desorption of negative hydrogen ions from diamond (100)*, Diam. Rel. Mat. **9** (2000), 1164.

[Gel96] R. Geller, *Electron Zyklotron Resonance Ion sources and ECR Plasmas*, Institute of Physics Publishing, Bristol and Philadelphia, 1996.

[Gil15] C. Gilles, *Private communication*, Aix-Marseille Université - PIIM, (France), 2015.

[GMS95] V. A. Godyak, V. P. Meytlis, and H. R. Strauss, *Tonks-Langmuir problem for a bi-Maxwellian plasma*, IEEE Trans. Plasma Sci. **23** (1995), 728.

[GPA92] V. A. Godyak, R. B. Pieak, and B. M. Alexandrovich, *Measurement of electron energy distribution in low-pressure RF discharges*, Plasma Sources Sci. Technol. **1** (1992), 36.

[Gra84] W. G. Graham, *Vacuum ultraviolet emission and H^- production in a low pressure hydrogen plasma*, J. Phys. D: Appl. Phys. **17** (1984), 2225.

[Gri74] H. R. Griem, *Spectral line broadening by plasmas*, Academic Press, New York and London, 1974.

[Gut15] P. Gutmann, *Private communication*, University of Augsburg, Experimental Physics II, (Germany), 2015.

[GWF+09] R. Gutser, D. Wünderlich, U. Fantz, et al., *Negative hydrogen ion transport in RF-driven ion sources for ITER NBI*, Plasma Phys. Control. Fusion **51** (2009), 045005.

[GWF11] R. Gutser, C. Wimmer, and U. Fantz, *Work function measurements during plasma exposition at conditions relevant in negative ion sources for the ITER neutral beam injection*, Rev. Sci. Instrum. **82** (2011), 023506.

[HA98] D. Hong and D. M. Aslam, *Technology and characterization of diamond field emitter structures*, IEEE Trans. on Electron. Dev. **45** (1998), 977.

[HCB64] J. O. Hirschfelder, C. F. Curtiss, and R. B. Bird, *The molecular theory of gases and liquids*, rev. edition ed., Wiley-Interscience, New York, 1964.

[HCL+88] R. I. Hall, I. Cadez, M. Landau, et al., *Vibrational Excitation of Hydrogen via Recombinative Desorption of Atomic Hydrogen Gas on a Metal Surface*, Phys. Rev. Lett. **60** (1988), 337.

[Heg02] B. Heger, *Spektroskopische Diagnostik zur Untersuchung der Besetzungsmechanismen von molekularem Wasserstoff und Deuterium in Niederdruckplasmen*, Ph.D. thesis, University of Augsburg - EPP, (Germany), 2002.

[Her50] G. Herzberg, *Molecular spectra and molecular structure, I. Spectra of diatomic molecules*, 2nd ed. ed., D. van Nostrand Company, New York, NY, 1950.

[Her15] Heriot-Watt University: School of Engineering & Physical Sciences; Photonics & Quantum Sciences, *http://www.hw.ac.uk/schools/engineering-physical-sciences/*, 2015.

[HF01] B. Heger and U. Fantz, *Modification of the ground state vibrational population of molecular hydrogen and deuterium by different wall materials in low temperature plasmas*, 28th EPS Conference on Controlled Fusion and Plasma Physics (Funchal) (C. Varandas C. Silva and D. Campbell, eds.), vol. 25A, 2001, p. 261.

[HFF+09] B. Heinemann, H. Falter, U. Fantz, et al., *Design of the 'half-size' ITER neutral beam source for the test facility ELISE*, Fusion Eng. Des. **84** (2009), 915.

[His80] J. R. Hiskes, *Cross sections for the vibrational excitation of the $H_2(X)$ state via electron collision excitation of the high singlet states*, J. Appl. Phys. **51** (1980), 4592.

[HK81] J. Harris and B. Kasemo, *On precursor mechanisms for surface reactions*, Surf. Sci. Lett. **105** (1981), L281.

[HKV+79] F. J. Himpsel, J. A. Knapp, J. A. van Vechten, et al., *Quantum photoyield of diamond (111) - a stable negative-affinity emitter*, Phys. Rev. B. **20** (1979), 624.

[HLU+01] A. Hoffman, A. Laikhtman, S. Ustaze, et al., *Dissociative electron attachment and dipolar dissociation of H^- electron stimulated desorption from hydrogen diamond films*, Phys. Rev. B. **63** (2001), 045401.

[IAE02] IAEA, *ITER technical basis*, ITER EDA documentation series 24, International Atomic Energy Agency, Vienna, 2002.

[IKS92] J. D. Isenberg, H. J. Kwon, and M. Seidl, *Surface production of H^- ions by backscattering of H^+ and H_2^+ ions in the 3 - 50 eV ion energy range*, AIP Conf. Proc. **287** (1992), 38.

[IMO+92] T. Inoue, Y. Matsuda, Y. Ohara, et al., *Effect of filament material and area on the extracted current from a volume H^- ion source*, Plasma Sources Sci. Technol. **1** (1992), 75.

[ITE16] ITER Organization, *website*, Available online at https://www.iter.org/, 2016, visited August 24 2016.

[JEN+02] N. Jiang, K. Eguchi, S. Noguchi, et al., *Structural characteristics and field electron emission properties of nano-diamond/carbon films*, J. Cryst. Growth **236** (2002), no. 4, 577.

[JL01] B. Jackson and D. Lemoine, *Eley-Rideal reactions between H atoms on metal and graphite surfaces: The variation of reactivity with substrate*, J. Chem. Phys. **114** (2001), 474.

[JRS03] R. K. Janev, D. Reiter, and U. Samm, *Collision processes in low-temperature hydrogen plasmas*, Tech. Report 4105, Forschungszentrum Jülich GmbH, (Jülich), 2003, [up-to-date data available online: www.hydkin.de].

[KAP+11] P. Kumar, A. Ahmad, C. Pardanaud, et al., *Enhanced negative ion yields on diamond surfaces at elevated temperatures*, J. Phys. D: Appl. Phys. **44** (2011), 372002.

[KFK01] A. V. Karabutov, V. D. Frolov, and V. I. Konov, *Diamond/sp^2-bonded carbon structures: quantum well field electron emission?*, Diamond Relat. Mater. **10** (2001), 840.

[Kie68] R. E. Kiel, *Electrostatic probe theory for free molecular cylinders*, Am. Ins. Aeron. and Astron. (AIAA) Journal **6** (1968), 708.

[Kov69] I. Kovács, *Rotational structure in the spectra of diatomic molecules*, Adam Hilger, London (UK), 1969.

[KRR+15] A. Kramida, Yu. Ralchenko, J. Reader, et al., *NIST Atomic Spectra Database (version 5.3)*, National Institute of Standards and Technology, Gaithersburg, MD, [Online] Available: http://physics.nist.gov/asd, (2015).

[KS97] G. I. Kuznetsov and E. A. Sokolovsky, *Dependence of effective work function for LaB_6 on surface conditions*, Phys. Scri. **T71** (1997), 130.

[Lab77] Oak Ridge National Laboratory, *Atomic data for controlled fusion research*, Report **1** (1977), 5206.

[Laf66] J. G. Laframboise, *Theory of spherical and cylindrical langmuir probes in a collisionless, maxwellian plasma at rest*, Tech. report, UTIAS - University of Toronto Institute for Aerospace Studies, 1966.

[Lan71] N. D. Lang, *Theory of work-function changes induced by alkali adsorption*, Phys. Rev. B. **4** (1971), 4234.

[LEB83] K. N. Leung, K. W. Ehlers, and M. Bacal, *Extraction of volume-produced h^- ions from a multicusp source*, Rev. Sci. Instrum. **54** (1983), 56.

[LEP85] K. N. Leung, K. W. Ehlers, and R. V. Pyle, *Effect of wall material on H^- production in a multicusp source*, Appl. Phys. Letters **47** (1985), 227.

[LF15] LSPM Laboratoire des Sciences des Procédés et des Matériaux (France), *http://www-lpmtm.univ-paris13.fr/?lang=fr*, 2015.

[LG90] J. Los and J. J. C. Geerlings, *Charge exchange in atom-surface collisions*, Phys. Rep. **190** (1990), 133.

[LL05] M. A. Lieberman and A. J. Lichtenberg, *Principles of Plasma Discharges and Material Processing*, 2nd ed., John Wiley & Sons, Inc., Hoboken, N.J., 2005.

[LS92] B. S. Lee and M. Seidl, *Surface production of H^- ions by hyperthermal hydrogen atoms*, Appl. Phys. Letters **61** (1992), 2857.

[LVL+94] A. J. Lichtenberg, V. Vahedi, M. A. Lieberman, et al., *Modeling electronegative plasma discharges*, J. Appl. Phys. **75** (1994), 2339.

[Mai11] T. Maier, *Laser-Photodetachment zur Quantifizierung der Volumenproduktion negativer Wasserstoffionen im ECR-Plasma*, University of Augsburg - EPP, (Germany), 2011, Diplomarbeit.

[McA14] R. McAdams, *Beyond ITER: Neutral beams for a demonstration fusion reactor (DEMO)*, Rev. Sci. Instrum. **85** (2014), 02B128.

[MFS+08] A. Manhard, U. Fantz, A. Stäbler, et al., *Spectroscopic studies on positive ion based neutral beam injection systems*, Tech. Report 4/289, Max-Planck-Institut für Plasmaphysik (IPP), Garching, 2008.

[MGH+06] I. Méndez, F. J. Gordillo-Vázquez, V. J. Herrero, et al., *Atom and ion chemistry in low pressure hydrogen dc plasmas*, J. Phys. Chem. A **110** (2006), 6060.

[Mic77] H. B. Michaelson, *The work function of the elements and its periodicity*, J. Appl. Phys. **48** (1977), 4729.

[Möl93] W. Möller, *Plasma and surface modeling of the deposition of hydrogen carbon films from low-pressure methane plasmas*, Appl. Phys. A **56** (1993), 527.

[MSL26] H. M. Mott-Smith and I. Langmuir, *The theory of collectors in gaseous discharges*, Phys. Rev. **28** (1926), 727.

[MTG72] W. T. Miles, R. Thompson, and A. E. S. Green, *Electron-Impact Cross Sections and Energy Deposition in Molecular Hydrogen*, J. Appl. Phys. **43** (1972), 678.

[NK07] S. Nunomura and M. Kondo, *Characterization of high-pressure capacitively coupled hydrogen plasmas*, J. Appl. Phys. **102** (2007), 093306.

[NL79] J. K. Norskov and B. I. Lundqvist, *Secondary-ion emission probability in sputtering*, Phys. Rev. B. **19** (1979), 5661.

[NSB98] M. Nishiura, M. Sasao, and M. Bacal, *H^- laser photodetachment at 1064, 532 and 355 nm in plasma*, J. Appl. Phys. **83** (1998), 2944.

[OD88] A. O'Keefe and D. A. G. Deacon, *Cavity ring-down optical spectrometer for absorption measurements using pulsed laser sources*, Rev. Sci. Intstr. **59** (1988), 25.

[OOR+89] D. K. Otorbaev, V. N. Ochkin, P. L. Rubin, et al., *Electron-impact excitation of rotational levels of molecules in gas discharge*, Electronically Excited Molecules in Nonequilibrium Plasma (N. N. Sobolev, ed.), Nova Science Publishers, Commack, NY, 1989.

[Pla01] Plansee Composite Materials GmbH, Germany, *http://www.plansee.com/de/*, 2001.

[PNM+83] M. J. Puska, R. M. Nieminen, M. Manninen, et al., *Quantum motion of chemisorbed hydrogen on ni surfaces*, Phys. Rev. Letters **51** (1983), 1081.

[PT01] S. Pfau and M. Tichy, *Langmuir probe diagnostics of low-temperature plasmas*, Low Temperature Plasma Physics (K. H. Schoenbach, ed.), Wiley-VCH, Berlin, 1st ed., 2001.

[PTB+85] M. Péalat, J.-P. Taran, M. Bacal, et al., *Rovibraiotnal molecular populations, atoms, and negative ions in H_2 and D_2 magnetic multicusp discharges*, J. Chem. Phys. **82** (1985), 4943.

[Qua16] Quantel GmbH, Germany, *http://www.quantel-laser.com*, 2016.

[Rau14] D. Rauner, *Cavity-Ring-Down-Spektroskopie zur Quantifizierung negativer Wasserstoffionen in einem ECR-Plasma*, Master's thesis, University of Augsburg - EPP, (Germany), 2014.

[RBB+12] F. Romanelli, P. Barabaschi, D. Borba, et al., *Fusion electricity - a roadmap to the realisation of fusion energy*, Tech. report, European Fusion Development Agreement (EFDA), 2012, online available at: https://www.euro-fusion.org/wpcms/wp-content/uploads/2013/01/JG12.356-web.pdf.

[Rot95] J. R. Roth, *Industrial plasma engineering vol.1: Principles*, Institute of physics, London, Bristol, UK, 1995.

[RWL82] B. Rasser, J. N. M. van Wunnik, and J. Los, *Theoretical model of the negative ionization of hydrogen on clean tungsten, cesiated tungsten and cesium surfaces at low energies*, Surf. Sci. **118** (1982), 697.

[Sar15] A. F. Sartori, *Private communication*, University of Augsburg, Experimental Physics IV, (Germany), 2015.

[SBB+06] P. Savarnas, J. Breton, M. Bacal, et al., *Pressure optimization for H^- ion production in an electron cyclotron resonance-driven and a filamented source*, Rev. Sci. Instrum. **77** (2006), 03A532.

[SBJ+12] E. Surrey, A. Benn, I. Jenkins, et al., *The influence of neutral beam optimization for DEMO on injector design*, Fusion Engineering and Design **87** (2012), 373.

[SCB99] T. E. Sheridan, P. Chabert, and R. W. Boswell, *Positive ion flux from a low-pressure electronegative discharge*, Plasma Sources Sci. and Technol. **8** (1999), 457.

[SCC+08] L. Schiesko, M. Carrère, M. Carty, et al., *H^- production on a graphite surface in a hydrogen plasma*, Plasma Sources Sci. Technol. **17** (2008), 035023.

[Sch93] U. Schumacher, *Fusionsforschung: eine Einführung*, Wiss. Buchges., Darmstadt, 1993.

[Sch15] M. Schreck, *https://www.physik.uni-augsburg.de/lehrstuehle/exp4/*, University of Augsburg, Experimental Physics IV, (Germany), 2015.

[SCM+07] M. Shimada, D. J. Champbell, V. Mukhovatov, et al., *Chapter 1: Overview and summary*, Nucl. Fusion **47** (2007), S1.

[SDB+90] R. A. Stern, P. Devynck, M. Bacal, et al., *Nonresonant optical tagging and 'monopolar' transport in negative-ion plasmas*, Phys. Rev. A **41** (1990), 3307.

[SFF+06] E. Speth, H. D. Falter, P. Franzen, et al., *Overview of the RF source development programme at IPP Garching*, Nucl. Fusion **46** (2006), S220.

[Sin14] Sindlhauser Materials GmbH, Germany, *http://www.sindlhauser.de/*, 2014.

[SKO+79] G. V. Samsonov, A. I. Kondrashow, L. N. Okhrenchuk, et al., *Work function of lab_6-based alloys*, J. Less-Common. Met. **67** (1979), 415.

[SPL+94] C. Schermann, F. Pichou, M. Landau, et al., *Highly excited hydrogen molecules desorbed from a surface: Experimental results*, J. Chem. Phys. **101** (1994), 8152.

[SS74] W. Stiller and R. Schmidt, *Two-temperature model for ion-molecule reactions*, Int. J. Mass Spectrom. Ion. Phys. **14** (1974), 237.

[Sta05] P. Starke, *Chemische Erosion verschiedener Kohlenstoff-Materialien durch Wasserstoff-Isotope in Niederdruckplasmen*, Ph.D. thesis, University of Augsburg - EPP, (Germany), 2005.

[SWW+05] J. A. Scheer, M. Wieser, P. Wurz, et al., *High negative ion yield from light molecule scattering*, Nucl. Instr. Phys. Res. Sec. B: Beam Interactions with Materials and Atoms **230** (2005), 330.

[TDJ+09] G. De Temmerman, R. P. Doerner, P. John, et al., *Interactions of diamond surfaces with fusion relevant plasmas*, Phys. Scr. **T138** (2009), 014013.

[TKH+97] K. Tsumori, W. R. Koppers, R. M. A. Heeren, et al., *Large ion yields in hydrogen scattering from a graphite surface*, J. Appl. Phys. **81** (1997), 6390.

[TL29] L. Tonks and I. Langmuir, *A general theory of the plasma of an arc*, Phys. Rev. **34** (1929), 876.

[UWG06] M. A. Uijttewaal, G. A. de Wijs, and R. A.de Groot, *Ab Initio Work Function and Surface Energy Anisotropy of LaB_6*, J. Phys. Chem. B **110** (2006), 18459.

[WDF09] D. Wünderlich, S. Dietrich, and U. Fantz, *Application of a collisional radiative model to atomic hydrogen for diagnostic purposes*, Journal of Quantitative Spectroscopy and Radiative Transfer **110** (2009), 62.

[WF01] D. Wünderlich and U. Fantz, *A Collisional-Radiative Model for H_2 and H: Extensions and Applications*, Tech. Report 10/18, Max-Planck-Institut für Plasmaphysik (IPP), Garching, 2001.

[WFF13] D. Wünderlich, U. Fantz, and P. Franzen, *Optical emission spectroscopy at the large RF driven negative ion test facility ELISE: Instrumental setup and first results*, Rev. Sci. Instr. **84** (2013), 093102.

[WGF09] D. Wünderlich, R. Gutser, and U. Fantz, *PIC code for the plasma sheath in large caesiated RF sources for negative hydrogen ions*, Plasma Sources Sci. Technol. **18** (2009), 045031.

[Wil66a] R. G. Wilson, *Electron and Ion Emission from Polycrystalline surfaces of Be, Te, Cr, Ni, Cu, Pt and Type-304 Stainless steel in Cesium Vapor*, J. Appl. Phys. **37** (1966), 3161.

[Wil66b] ———, *Electron and Ion Emission from Polycrystalline surfaces of Nb, Mo, Ta, W, Re, Os and Ir in Cesium Vapor*, J. Appl. Phys. **37** (1966), 4125.

[Wim14] C. Wimmer, *Characteristics and Dynamics of the Boundary Layer in RF-driven Sources for Negative Hydrogen Ions*, Ph.D. thesis, University of Augsburg - EPP, (Germany), 2014.

[Win02] H. Winter, *Collisions of atoms and ions with surfaces under gracing incidence*, Phys. Rep. **367** (2002), 387.

[Wün04] D. Wünderlich, *Berechnung von Teilchendichten für die Diagnostik an Niedertemperaturplasmen*, Ph. D. thesis, University of Augsburg - EPP, (Germany), 2004.

[Wün14] ———, *Private communication*, Max-Planck-Institut für Plasmaphysik (IPP), Garching, 2014.

[WPL73] G. A. Woolsey, I. C. Plumb, and D. B. Lewis, *Langmuir probe charachteristics in a positive-ion/negative-ion plasma*, J. Phys. D: Appl. Phys. **6** (1973), 1883.

[WSA97] P. Wurz, R. Schletti, and M. R. Aellig, *Hydrogen and oxygen negative ion production by surface ionization using diamond surfaces*, Surf. Sci. **373** (1997), 56.

[WSF16] C. Wimmer, L. Schiesko, and U. Fantz, *Investigation of the boundary layer during the transition from volume to surface dominated H^- production at the BATMAN test facility*, Rev. Sci. Instr. **87** (2016), 02B310.

[WSH85] B. Willerding, K. Snowdon, and W. Heiland, *The interaction of fast H_3^+ ions with a clean Ni-surface*, Zeitschrift für Physik B: Condensed Matter **59** (1985), 435.

[WSM+12] D. Wünderlich, L. Schiesko, P. McNeely, et al., *On the proton flux toward the plasma grid in a RF-driven negative hydrogen ion source for ITER NBI*, Plasma Phys. Control. Fusion **54** (2012), 125002.

[WZB+94] J. van der Weide, Z. Zhand, P. K. Baumann, et al., *Negative-electron-affinity effects on the diamond (100) surface*, Phys. Rev. B. **50** (1994), 5803.

[YNX+04] J. Yang, Z. Nie, X. Xi, et al., *Emission ability of La-Sc-Mo cathode*, Appl. Surf. Sci. **229** (2004), 51.

Acknowledgements

An dieser Stelle möchte ich mich bei allen bedanken, die zur Entstehung dieser Arbeit beigetragen haben. Insbesondere gilt mein Dank:

- Frau **Prof. Dr.-Ing. Ursel Fantz** für die Möglichkeit, diese Doktorarbeit in der AG Experimentelle Plasmaphysik bzw. am Max-Planck-Institut für Plasmaphysik durchzuführen, sowie für das hohe Niveau der wissenschaftlichen Ausbildung und die gute Betreuung während der gesamten Arbeit.
- Herrn **Prof. Dr. Achim Wixforth** für die Übernahme des Zweitgutachtens.
- Herrn **Dr. Roland Friedl** für die unglaubliche Unterstützung während der gesamten Arbeit, das Korrekturlesen, die zahllosen Diskussionen und vorallem für die wahnsinns Freundschaft!
- Den Herren **Dr. Stefan Briefi**, **David Ertle**, **Patrick Gutmann**, **Sinan Kalafat**, **David Rauner** und Frau **Sofia Cristofaro** für all die Unterstützung und eure Freundschaft.
- Den Kollegen der **AG Experimentelle Plasmaphysik** die ich über die gesamte Zeit in der Arbeitsgruppe kennen und schätzen lernen durfte, für eure Unterstützung und die gute Zusammenarbeit.
- Dem gesamten **NNBI-Team** für die Unterstützung und die Hilfestellungen. Insbesonders möchte ich an dieser Stellen den Herrn **Dr. Christian Hopf**, **Dr. Loïc Schiesko**, **Dr. Christian Wimmer**, **Dr. Dirk Wünderlich** sowie den Herren **Martin Kammerloher** und **Johannes Kolbinger** für die stetige Hilfsbereitschaft und Unterstützung danken.
- Der feinmechanischen Werkstatt und der Elektronikwerkstatt des Physik Instituts für die Unterstützung und die Herstellung zahlreicher notwendiger Komponenten.
- Den Herrn **Dr. Matthias Schreck**, **Dr. André Sartori** und **Björn-Christoph Gallheber** für die wissenschaftlichen Diskussionen, Bereitstellung von Proben und Durchführung von Messungen.

Zu guter letzt möchte ich mich ganz besonders bei meiner gesamten Familie bedanken. Eurer Rückhalt und euer Verständnis hat maßgeblich dazu beigetragen, dass ich diese Arbeit verfassen konnte!